Electrochemical Metabolic Profiling of Live cells and Pancreatic Islets

By

Jeremy P. Wilburn

Dissertation

Submitted to the Faculty of the

Graduate School of Vanderbilt University

in partial fulfillment of the requirements

for the degree of

Doctor of Philosophy

in

Chemistry

May, 2009

Nashville, Tennessee

Approved:

Dr. David E. Cliffel

Dr. Sandra Rosenthal

Dr. David Wright

Dr. John P. Wikswo

Dr. David Weaver

For Leslie, whose music lifts my soul, and for Maria,

who will be always and forever my princess.

ACKNOWLEDGEMENTS

This work would not have been possible without the financial support in the form of research grants from the Defense Advanced Research Projects Agency, the Department of Energy, the Department of Defense, and the National Institute of Allergy and Infectious Disease, and from Vanderbilt University, through my advisor's startup funds and my research and teaching stipends. I would also like to especially thank my advisor and mentor, Dr. David Cliffel, for his patience, advice, and support throughout my stay at Vanderbilt, and for the active participation of my graduate committee; Dr. Sandra Rosenthal, Dr. David Weaver, Dr. John Wikswo, and Dr. David Wright.

I would also like to thank all those I have had the pleasure of working with at Vanderbilt, in particular all members of the Cliffel research group. Several ideas from our weekly group and subgroup meetings made their way into my research in one form or another, and the group's input on my various presentations and publications have been an invaluable assistance to me as well. In particular I would like to thank Dr. Madalina Ciobanu, Dr. Rachel Snider and Jennifer Merritt for all of their assistance with the Multianalyte Microphysiometry research presented in this work.

Finally, no thanks would be complete without including the members of my family, my father, who stretched a 9th grade education as far as anyone, my brother Jason and my mother. Of course, none of this has meaning without my children, one of whom was born during my stay here at Vanderbilt, and both of whose smiles and love made this long journey possible.

Thank you all.

TABLE OF CONTENTS

LIST OF TABLES

Table Page

LIST OF FIGURES

LIST OF ABBREVIATIONS

5-HT	5-hydroxytryptamine
AA	ascorbic acid
AC	approach curve
AcCOA	acetyl coenzyme-A
ACh	acetylcholine
AChE	acetylcholinesterase
ADP	adenosine diphosphate
ATCC	American type culture collection
ATP	adenosine triphosphate
BChE	butyrylcholinesterase
BioSECM	biological scanning electrochemical microscope/microscopy
BLM	bilayer lipid membrane
BSA	bovine serum albumin
CaM	calmodulin
cAMP	cyclic adenosine monophosphate
C_d	capacitance
C_d^0	bulk capacitance
CE	counter electrode
Cf-UME	carbon fiber ultramicroelectrode
chemFET	chemically sensitive field effect transistor
CV	cyclic voltammogram/voltammetry
D	diffusion coefficient
DAG	diacylglycerol
DHP	2-dihydropyran

Δi_p	peak current change
$\Delta\mu_H$	proton motive force
$\Delta\Psi_m$	membrane potential
ΔpH	proton gradient
DMF	dimethylformamide
DMSO	dimethylsulfoxide
DOPA	3,4-dihydroxy-phenylalanine
DPBS	Delbucco's phosphate buffered saline
ELISA	enzyme linked immunosorbent assay
EtOH	ethanol
FBS	fetal bovine serum
FcTMA	Ferrocenylmethyltrimethylammonium
FVB	Friend leukemia virus B
GAPDH	glyceraldehyde 3-phosphate dehydrogenase
GCE	glassy carbon electrode
GDA	glucose-6-phosphate dehydrogenase
GFP	green fluorescent protein
GOx	glucose oxidase
HA	hemagglutinin
HBSS	Hank's buffered salt solution
HEPES	N-2-Hydroxyethylpiperazine-N'-2-Ethanesulfonic Acid
IDH	isocitrate dehydrogenase
IP	inositol phosphate
IP_3	inositol triphosphate
i_{photo}	photocurrent

i_{ss}	steady-state current
$i_{ss,\infty}$	steady-state current at infinite distance from substrate
i_{tip}	tip current
LAPS	light-addressable potentiometric sensor
LDH	lactate dehydrogenase
LOx	lactate oxidase
mAChR	muscarinic acetylcholine receptor
MAMP	multianalyte microphysiometry
MAP	mitogen activated protein
MAPK	mitogen activated protein kinases
MWCNT	multiwall carbon nanotubes
MWCNT/DMF	multiwall carbon nanotube/dimethylformamide
nAChR	nicotinic acetylcholine receptor
NAD	nicotinamide adenine dinucleotide
NADH	nicotinamide adenine dinucleotide (reduced form)
NTE	neuropathy target esterase
O	oxidized form of redox couple
OAP	orthoaminophenol
PC12	pheochromacytoma cell line
PIP_2	phosphatidylinositol biphosphate
PFK	phosphofructokinase
PKC	protein kinase C
PLC	phospholipase C
PSC	probe scan curve
Ψ	electric field potential
r	radius

R	reduced form of redox couple
RE	reference electrode
ROS	reactive oxygen species
RPMI	Royal Park Memorial Institute (originator of cell culture media)
Ru-hex	ruthenium hexamine
SE	substrate electrode
SECM	scanning electrochemical microscope/microscopy
SNARE	soluble NSF associated protein receptors
SWV	square-wave voltammetry
TCA	tricarboxylic acid
t_{flow}	time of flow period
t_{stop}	time of stop period
UME	ultramicroelectrode
V_{max}	rate maximum
V_{O2}	respiration rate

CHAPTER I

INTRODUCTION

> "Progress in science depends on new techniques, new discoveries, and new ideas, probably in that order of decreasing importance."[1]
>
> -Sydney Brenner (2002 Nobel co-laureate in Physiology or Medicine)

The development of new techniques that increase our knowledge of both normative biological metabolism at the cellular level, and metabolic deviation in the event of disease, is crucial to the advancement of biology. New techniques, in turn, often rely upon innovations in instrumentation to facilitate their development,[1] especially when existing instrumentation for whatever reason is inadequate to perform the measurements demanded by the technique. Of all the current fields of novel biological research, the emerging field of metabolomics, defined as the "systematic study of the unique chemical fingerprints that specific cellular processes leave behind,"[2] is expected to be the most predictive of the overall phenotype of an organism,[3,4] and thus the best suited for use in the diagnosis of disease and detection of metabolic dysfunction.[5] Therefore the development of instruments, and new instrumental techniques, that are capable of probing metabolic activities on the cellular level is critical to the advancement of metabolomics and with it our understanding of cellular biology.[3]

In the past hundred years, thanks to a myriad of research efforts, cellular biochemical pathways have been painstakingly mapped out. The individual components of these pathways, including enzymes, substrates, intermediates and products, are now more completely understood than nearly any other aspect of biology.[6] The available studies, however, present a fragmented view of the totality of cellular metabolism. Since each study focused on an individual enzyme or pathway, we are left with a patchwork of individual snapshots that have been aggregated to form

a collage of the entire cellular biochemical pathway. What is missing in this aggregate are the quantitative relationships between the individual metabolites of different pathways that, if known, could lead to a better understanding about the balance of differing, and sometimes competing, processes present in a healthy metabolism. This, in turn, would allow the better determination of the extent and type of metabolic dysfunction in diseased organisms. In short, the dynamic aspects of metabolism, and therefore of cellular biology, simply cannot be understood without an in-depth knowledge of not only the type, but also the relative quantities of metabolites and metabolic precursors that exist, and the conditions under which they are present, in both healthy and diseased states of living cells and organisms.[7,8]

By studying individual metabolites and their relationships with respect to a particular disease we can find specific compounds, known as biomarkers, that could be used to detect the presence of, or estimate the extent of, a specific disease. One such example is the discovery of the linkage between the presence of the protein troponin-I (tn-I) in the bloodstream and cardiac muscle damage. While tn-I is present in healthy cardiac muscle, in the event of muscle damage, as in a myocardial infarction (heart attack), tn-I is released into the blood stream by cardiac necrosis.[9] Since tn-I is specific to cardiac tissue the detection of tn-I in the blood stream, done via immunoassay[10,11] or fluorometric analysis,[12,13] is then specifically indicative of cardiac damage, and therefore now used as the definitive diagnosis of myocardial infarction. Additionally, other research is currently underway to determine new cardiovascular-specific biomarkers and pathways in order to detect the presence of myocardial damage, such as cardiac myopathy, before the damage becomes irreversible.[14]

Although the core cause of most diseases are tied to faulty enzyme activity, improper substrate balance, or faulty metabolic regulation, the net result of all these things is a perturbation of cellular metabolism.[6] Additionally, the fact that metabolic disorders such as atherosclerosis, obesity, hypertension, and diabetes are increasingly seen as being epidemic in the population,[15]

has recently led to an increasing emphasis on the adaptation of technology toward the investigation of the intricacies of metabolism. Just as a project was undertaken to sequence the entirety of genes in human DNA, known now as the 'genome', the desire for a similar inventory of metabolites present within and surrounding cells, called the 'metabolome', is being focused under the newly founded field of metabolomics/metabonomics.[5,16,17] Metabolomics, even though a new field, could enable the discovery of new signaling pathways and new areas of research building upon what is already known about cellular biochemical pathways.[18]

While the first objective of the genome project was a mapping of all of the genes within human DNA, the initial goal of metabolomics is to obtain an inventory of all or a substantial fraction of metabolites present in a biological sample, and to quantify each individual metabolite with respect to an absolute index of the sample (per gram, milliliter, or cell).[6,7] Since an immediate consequence of a diseased state in an organism is a perturbation of metabolic activity, it follows that changes in the relative quantities of both metabolic precursors and metabolites would occur as well. If an accounting were made of all such compounds present in the healthy state of an organism, the detection of that perturbation would be a valuable tool in and of itself in the diagnosis of disease.

The completion of a metabolic inventory may prove to be far more difficult than the genome project, however, because unlike DNA, metabolites have a wide distribution of molecular compositions and physical properties.[6] Analysis of metabolites *en masse* is typically performed by NMR spectroscopy or capillary electrophoresis-mass spectrometry of body fluids (*e.g.*, blood or urine),[5,19-21] allowing the deconvolution of metabolic events which occur on a different temporal scale. [22,23] The primary advantage of these techniques is the measurement of multiple analytes simultaneously. The drawback, however, is that the convolution of the signals generated requires intricate computer analyses,[19] and individual analyte targeting is extremely difficult if not impossible without the addition of extraneous tags to individual metabolic

markers.[24,25] Another problem is that these instruments are only capable of offering *ex-situ* analyses of the metabolites, and thus while enabling temporal resolution of the metabolic activities, they are unable to offer results in real-time.[24] In any event, bulk analysis of all components of the metabolome, either qualitatively or quantitatively, is beyond the scope of the work presented here.

In the study of cellular metabolism, another key aspect is the utilization of non-invasive means of measurement. Since the aim of the experiment is to detect and observe minute changes in physiological metabolic activity, it is an absolute imperative that the act of performing the measurement itself does not make unrecognized changes of its own in the metabolic activity under study. Therefore, in order to draw meaningful conclusions from any data gathered, one must be able to say with a high degree of certainty that any changes observed are due to metabolic agent activity, or the presence of disease, rather than the presence of, or in response to, the analytical equipment, or chemical substances added while performing the measurement.

The 2008 Nobel prize for chemistry was awarded for the discovery and development of green fluorescent protein (GFP), due to the contributions of its wide spread use as a fluorescent tag in cell experiments. It has been found, however, that the addition of GFP as a chimeric tag to a protein will actually alter the normative cellular response to that protein.[26] Another frequently used method is the addition of epitope tags, which are utilized in conjugation with enzyme linked immunosorbent assays (ELISA). One of the most frequently utilized epitope tags is hemagglutinin (HA), which is a naturally occurring surface protein from the influenza virus. Like GFP, however, HA tagging has been shown to alter cellular metabolism.[27-29] Even the addition of a simple six amino acid residue tag has been shown to affect cellular enzyme processing.[30] While the added effect of these extraneous tags can sometimes be compensated for by comparison to the activity of their wild-type cousins, this adds yet another experimental step to an already complex

analysis. Clearly what is needed is an instrumental technique that is neither physically invasive nor requisite on the addition of deleterious compounds to perform analyses.

Since living organisms are not static systems, the ability of a measurement technique to render measurement of dynamic cellular processes in real-time is also highly desirable.[31,32] Cellular biology provides multiple control points, signal cascades and feedback mechanisms with which to respond to changes in both internal and external stimuli. The biological response to any specific metabolic agent is often not as simple as a switch to a "high" or "low" level of a specific metabolite or metabolic rate. One example is the biphasic release of insulin from β-cells in response to a spike in blood glucose levels, in which an initial short burst of insulin is followed by a sustained slow release. This subtle, temporally dynamic response would not be possible to observe if it were not for real-time methods of analysis. While it would be possible to quantitatively determine the amount of insulin released with *ex-situ* measurements it would not be possible to ascertain the manner in which it was released, and thus the mechanism governing the response would remain elusive. Additionally, since metabolomics focuses on the balance of various metabolites in relationship to changes in metabolic activity, the instrument should allow multi-analyte detection capabilities.

While live cell studies of metabolic activity currently focus on large numbers of cultured cells, those studies are irreconcilably limited to data that is also averaged over a large number of cells. It is rapidly becoming clear that even within a given phenotype there is considerable variability of metabolic activity from cell to cell. It may be adequate to utilize an averaged cellular response to detect, or diagnose, a particular disease or metabolic dysfunction, however in order to understand the actual mechanism behind the disease itself we must understand such activities on a single cell level. For this reason, investigations of large numbers of cells must be coupled with single-cell analyses, in order to better determine the statistical variability normally present in a population of healthy cells. This requires instrumental methods that both have

sufficient sensitivity to detect the shifts in metabolic activity of a single live cell, and that will allow miniaturization to the scale where those measurements may be performed.

In summation, the field of metabolomics requires methods of investigation that allow multiple analytes to monitored *in-situ*, non-invasively in real-time and by a platform that can be scaled toward single cell analyses when required. One method that is capable of meeting all these requirements is electrochemistry. Electrochemical measurements can be performed non-invasively, and for metabolites that are electrochemically active, or those that can be detected with chemically-modified electrodes, electrochemical measurements provide a relatively simplistic and rapid means with which to perform metabolic analyses. For example, the most frequent analytical chemical measurement today, the testing of blood glucose, is neither performed in a lab nor by trained technicians. Rather the testing of blood glucose levels, which is required daily to monitor the glucose homeostasis of Diabetes patients, is almost exclusively performed electrochemically by the patients themselves, using a glucose sensitive sensor in conjunction with a mass produced, hand-held instrument. Furthermore, when coupling electrochemical sensors with a microfluidic design, the resulting instrumentation has the demonstrated capability of *in situ* analyses for tissues and live cultured cells.[32] Additionally, electrochemistry is able to provide real-time measurement of dynamic processes, including simultaneous detection of multiple analytes. In some cases electrochemical instrumentation can be designed on such a scale as to allow for portability of the entire instrument, which presents the possibility of bringing the means of analysis to the subject rather than the other way around. Furthermore electrochemistry is capable of utilizing extremely small sensor designs that have extremely high sensitivity, and in specific cases have been shown to be able to perform single-molecule detection.[33]

References

(1) Brenner, S. *The Scientist* **2002**, *16*, 15.
(2) Daviss, B. *The Scientist* **2005**, *19*, 25-28.
(3) Blow, N. *Nature* **2008**, *455*, 697-700.
(4) Giovane, A.; Balestrieri, A.; Napoli, C. *J. Cell. Biochem.* **2008**, *105*, 648-654.
(5) Lindon, J. C.; Holmes, E.; Nicholson, J. K. *Anal. Chem.* **2003**, *75*, 384A - 391A.
(6) German, J. B.; Hammock, B. D.; Watkins, S. M. *Metabolomics* **2004**, *1*, 3-9.
(7) Fiehn, O. *Comp. Funct. Genom.* **2001**, *2*, 155-168.
(8) Tomita, M.; Nishioka, T., Eds. *Metabolomics: The Frontier of Systems Biology*; Springer-Verlag: Tokyo, 2003.
(9) Cummins, B.; Cummins, P. *J. Mol. Cell. Cardiol.* **1987**, *19*, 999-1010.
(10) Kuhr, L. P.; Baum, H.; Schweigert, R.; Hafner, G.; Prellwitz, W.; Neumeier, D. *Eur J Clin Chem Clin Biochem* **1997**, *35*, 399-404.
(11) Panteghini, M.; Bonora, R.; Pagani, F. *Int J Clin Lab Res* **1997**, *27*, 60-64.
(12) Gerhardt, W.; Nordin, G.; Herbert, A. K.; Burzell, B. L.; Isaksson, A.; Gustavsson, E.; Haglund, S.; Muller-Bardorff, M.; Katus, H. A. *Clin Chem* **2000**, *46*, 817-821.
(13) Pettersson, K.; Katajamaki, T.; Irjala, K.; Leppanen, V.; Majamaa-Voltti, K.; Laitinen, P. *Luminescence* **2000**, *15*, 399-407.
(14) Lewis, G. D.; Gerszten, R. E. *Clin. Prot.* **2008**, 279-293.
(15) Alberti, G. *B. World Health Organ.* **2001**, *79*, 907.
(16) Clarke, C. J.; Haselden, J. N. *Toxicol. Pathol.* **2008**, *36*, 140-147.
(17) Wikswo, J. P.; Prokop, A.; Baudenbacher, F.; Cliffel, D. E.; Csukas, B.; Velkovsky, M. *IEEE Proc. Nanobiotechnol.* **2006**, *153*, 81-101.
(18) Samuel, J.-L.; Schaub, M. C.; Zaugg, M.; Mamas, M.; Dunn, W. B.; Swynghedauw, B. *Cardiovasc. Res.* **2008**, *79*, 218-227.
(19) Lindon, J. C.; Nicholson, J. K. *Trends Anal. Chem.* **2008**, *27*, 194-204.
(20) Robertson, D. G. *Toxicol. Sci.* **2005**, *85*, 809-822.
(21) Verpoorte, R.; Choi, Y. H.; Mustafa, N. R.; Kim, H. K. *Phytochem. Rev.* **2008**, *7*, 525-537.
(22) Griffin, J. *Drug Discov. Today* **2004**, *1*, 285-293.
(23) Nicholson, J. K.; Lindon, J. C.; Holmes, E. *Xenobiotica* **1999**, *29*, 1181-1189.
(24) Goudar, C.; Biener, R.; Zhang, C.; Michaels, J.; Piret, J.; Konstantinov, K. *Adv. Biochem. Eng. Biotechnol.* **2006**, *10199-118*.
(25) Wittman, C.; Heinzle, E. *Biotechnol. Bioeng.* **1999**, *62*, 739-750.
(26) Brothers, S. P.; Janovick, J. A.; Conn, M. *J. Clin. Endocr. Metab.* **2003**, *88*, 6107-6112.
(27) Koller, K. J.; Whitehorn, E. A.; Tate, E.; Ries, T.; Aguilar, B.; Chernov-Rogan, T.; Davis, A. M.; Dobbs, A.; Yen, M.; Barrett, R. W. *Anal. Biochem.* **1997**, *250*, 51-60.
(28) Romano, J. D.; Schmidt, W. K.; Michaelis, S. *Mol. Biol. Cell* **1998**, *9*, 2231-2247.
(29) Tolbert, L. M.; Lameh, J. *J. Neurochem.* **1998**, *70*, 113-119.
(30) Ledent, P.; Duez, C.; VAnhove, M.; Lejune, A.; Fonze, E.; Charlier, P.; Rhazi-Filali, F.; Thamm, I.; Guillaume, G.; Samyn, B.; Devreese, B.; Van Beeumen, J.; Lamotte-Brasseur, J.; Frere, J. M. *FEBS Lett.* **1997**, *413*, 194-196.
(31) Eklund, S. E.; Kozlov, E.; Taylor, D. E.; Baudenbacher, F.; Cliffel, D. E. *Methods Mol. Biol.* **2005**, *303*, 209-223.
(32) Eklund, S. E.; Taylor, D.; Kozlov, E.; Prokop, A.; Cliffel, D. E. *Anal. Chem.* **2004**, *76*, 519-527.
(33) Fan, F. R.; Bard, A. J. *Science* **1995**, *267*, 871-874.

CHAPTER II

BACKGROUND

Sensors

Electrochemical sensors have a long history in the measurement of key metabolic biomarkers. The current *state of the art* in electrochemical metabolic investigation includes many macro scale sensors. The desire to extend metabolomic studies to the single cell level, however, demands that these sensors be adapted to the ultramicro scale, or new sensors be designed and implemented to allow single cell metabolic studies to be performed. In the work presented here, several electrochemical sensors were utilized to follow changes in metabolic activity, including chemically modified sensors and enzyme modified electrodes on both the macro and ultramicro scale.

Oxygen sensors

One of the most elementary electrochemical assays is the reduction of dissolved oxygen, first observed by Ludwig Danneel in 1897[1] and later encountered by Heyrovsky in his development of polarography.[2] Initial biological studies were underway as early as 1933 and reported by Baumberger in his "Apparatus for the study of reduction-oxidation potential in biological systems."[3] The studies utilized the dropping mercury electrode, and in the following years he established the ability to measure dissolved oxygen[4,5] and applied it to the study of the respiratory activity of live yeast cells.[6] Baumberger also coupled his electrochemical analysis with a study of heat production to generate one of the first metabolic studies of respiration and glucose metabolism of live cells.[7] There were problems with the use of mercury electrodes and biological systems however, including toxicity, the variation in the size of mercury droplets (in

the case of early dropping mercury electrodes) and protein contamination of the mercury itself (in the case of a static mercury electrode).[8] In 1948, Davies and Brenk were the first to utilize a Pt cathode,[9] which was mounted in a saline-filled glass capillary with an agar plug to minimize contamination (Fig. 2.1a). While this was more successful than Baumberger's previous attempts, there were still problems with long-term stability due to fouling of the electrode surface.

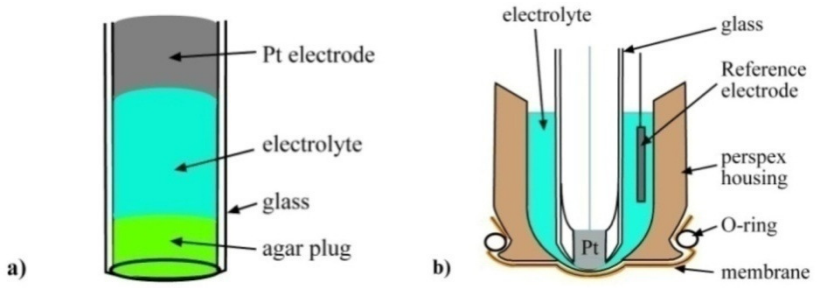

Figure 2.1; (a) shows the oxygen sensor of Davies and Brenk, which used an agar plug to prevent fouling, (b) shows the Clark oxygen electrode, which first utilized a cellophane membrane, and later a hydrophobic membrane to prevent biofouling of the Pt sensing electrode. [adapted from Silver][8]

To eliminate fouling in 1953 Leland Clark proposed isolation of the Pt electrode behind a gas permeable cellophane membrane[10,11] in order to measure oxygen saturation in human blood during early human total heart bypass surgeries. While this reduced bio-fouling, the cellophane membrane was water, as well as gas, permeable, which continued to allow some proteins to come into contact with the electrode surface. Finally, in 1956, Clark improved his design by replacing the cellophane with a hydrophobic membrane (now universally known as the Clark oxygen electrode, Fig. 2.1b),[12] which addressed the bio-fouling problem more completely. The electrode design, featuring a hydrophobic membrane, is still in use today, more than a half century after its initial publication. Later studies by Clark included continual patient oxygen monitoring,[13] the use of pyrolitic graphite electrodes for biological oxygen measurement,[14] and the design of portable solid-state amplifiers for his instrumentation.[15] The Clark oxygen electrode continues to be used to this day, with little or no modifications beyond those presented in his 1956 paper.[12] More

recently, the application of a hydrophobic film of Nafion® to a bare Pt electrode[16,17] has permitted oxygen sensors to be incorporated into smaller instrumental platforms. While later cathodes in Clark electrodes were actually quite small, due to the incorporation of the reference half-cell within the electrode enclosure (Fig. 2.1b), the entire sensor assembly is considerably more bulky. Application of the hydrophobic membrane directly to the Pt surface allows separation of the two electrochemical half-cells, without minimizing prevention of biofouling, and allows for smaller sensor designs, including applications in scanning probe techniques. Although these are not Clark electrodes *per se*, they are designed around the key elements of the Clark oxygen electrode; a Pt cathode and a hydrophobic membrane to minimize biofouling.

The use of the Clark oxygen electrode for monitoring patient arterial blood oxygen levels has been almost completely supplanted by the introduction of non-invasive fingertip spectrophotometric oximeters.[18] Fingertip oximeters are capable of providing continual, real-time monitoring of the oxygen saturation in a patient's blood utilizing only a single fiber-optic probe in contact with the exterior of the patient's fingertip. The arterial blood oxygen saturation is then detected by measuring the fluctuations in light intensity due to the pulsatile flow of blood into the fingertip. In this way the transmitted light can be corrected for the absorption by the muscle and tissue portions of the fingertip (which is of a constant nature). While spectrophotometry is the currently preferred method of analysis for hospital patients, electrochemistry remains an important method of the determination of oxygen respiration rates of single cells[19] and tissue,[20] and has been proposed as a viability assay for islets destined for human transplantation.[21] Similarly, mitochondrial electrochemical respiration measurements have been more recently performed, including work presented later here, via multianalyte microphysiometry (MAMP)[22-24] and scanning electrochemical microscopy (SECM).[25-35]

Enzyme-modified electrodes

Another tool that finds use in modern electrochemical metabolic measurement, and one also introduced by Leland Clark,[36] is the enzyme-modified electrode. The introduction of enzyme electrodes to metabolic analyses has greatly increased the range of analytes detectable by electrochemistry. Additionally, the exquisite selectivity of enzymes toward their substrate of choice brings with it the highest level of specificity. This is especially critical given the extent of possible interferents in the highly complex samples used in metabolic analyses.[37] The first enzyme electrode was an adaptation of Clark's previous work with oxygen sensors. Instead of detecting dissolved oxygen, however, the enzyme sensor design utilized the Pt cathode to detect H_2O_2 generated by a peroxidase enzyme sandwiched between two permeable membrane layers, which were incorporated in lieu of the oxygen electrode's external hydrophobic membrane (see Fig. 2.1b). The electrode was designed to measure physiological glucose concentrations in blood, in concert with the Clark oxygen electrode, during heart bypass surgery. The basis for Clark's electrode is identical in principle, but not in design, to the enzyme electrodes presented later in this work. The enzyme utilizes a specific substrate (either lactate or glucose in our case), and in the process of substrate conversion generates H_2O_2 from dissolved oxygen. The peroxide then migrates toward the Pt electrode surface, which is biased at a potential to drive its oxidation, as shown in Eq. 2.1.

$$H_2O_2 \rightarrow 2H^+ + O_2 + 2e^- \text{ (E° = + 473 mV } \textit{vs.} \text{ Ag/AgCl, 3 M KCl)}^{38} \quad (2.1)$$

Alternate possibilities for modified enzyme electrode design include the use of an incorporated electrochemical mediator to replace the oxygen/peroxide couple. One advantage of the incorporation of an external mediator is that a lower potential can be used to drive the reaction at the electrode, depending on the choice of mediator to incorporate. There is the added possibility, however, of this mediator leeching from the sensor and contaminating the system under study.[39] Recent state of the art in enzyme electrode systems, however, attempts to eliminate the possibility of redox mediator leakage by providing a covalent linkage between the

electrode surface, the enzyme itself, and the incorporated mediator. This concept was originated by Heller and coworkers,[39] who linked glucose oxidase (GOx) to a hydrogel that incorporated Os(4,4'-dimethylbpy)$_2$Cl as a redox mediator. If there is a problem with the somewhat high reduction potential of peroxide, another possibility is to immobilize a second enzyme, such as horseradish peroxidase, on the electrode surface. With the inclusion of horseradish peroxidase, electrode potentials can be reduced by some 100 mV.[40] In situations where the oxidation potential of peroxide has not proven to be problematic, however, the simplest solution is generally the best and therefore no external mediator is required.

Insulin detection

Due to the rise in the prevalence of *diabetes mellitus* among the general populace, there has been a drastic increase in the number of investigations into the metabolic processes affected by diabetes over the past decade, and with it an increased demand for novel techniques to assist their research. Metabolic studies that focus on the mechanisms of islets and diabetes typically utilize either an immortalized cultured β cell line, or whole pancreatic islets extracted from mice or rats. The techniques possible for probing triggered insulin release include perfusion experiments coupled with *ex-situ* insulin detection via ELISA, radioimmunoassay, or chromatography.[41-43] Kennedy's group has used an electrophoresis-based immunoassay for insulin, and fluorescence spectroscopy for detection of the Zn co-factor and intracellular Ca levels.[44-48] While these methods have suitably low detection limits they either require extended periods of time to acquire data via *ex-situ* analysis, or require the addition of extraneous tags that could possibly alter the metabolic activity under study.[49-52] The use of direct electrochemical oxidation of insulin for a means of detection, on the other hand, avoids these problems and additionally allows real-time, *in-situ* data collection.[53-55]

The first electrochemical study of insulin release utilized 5-hydroxytryptamine (5-HT), which can be taken up by β cells and stored within insulin granules.[56] When insulin is released

by the cells, the 5-HT is released as well.[57-59] This technique, however, required preconditioning of the islets and lacked direct quantitative correlation between the detected 5-HT levels and amount of insulin secreted. While other investigations have electrochemically targeted the zinc cofactor of insulin,[60] there have been more recent developments in direct electrochemical oxidation of insulin at modified electrode surfaces. These sensor designs have included ruthenium metallodendrimers,[61] ruthenium dioxide,[45] ruthenium dioxide/cyanoruthenate,[45,62] and iridium oxide.[63] Of these, however, the iridium oxide sensors suffer from pH sensitivity and slow transport rates,[64] and the ruthenium oxide and metallodendrimer films have mixed oxidation states with complex e^- transfer kinetics that vary according to the crystal face of the electrode surface.[65]

While the majority of electrochemical investigations are done using noble metal electrodes, biological investigations tend to favor the more biologically friendly carbon-based electrodes.[66-69] The use of carbon as an electrode material for biological studies dates back to Leland Clark's use of pyrolitic graphite to measure epicardial oxygen concentrations.[14] Other forms of carbon electrodes have included glassy carbon,[67,70] graphite paste,[71-73] carbon fibers,[74-76] and most recently carbon nanotubes.[77-80] The first carbon nanotube insulin sensor was developed by Wang and Musameh,[78] and utilized a dimethylformamide (DMF) nanotube dispersion to create a film on the electrode, and recently Wang has incorporated ruthenium oxide into his nanotube film as well.[81] Wang's nanotube modified sensor, however, was found to have topographical inconsistencies caused by clumping of the nanotubes during evaporation of the DMF.[54] Salimi and coworkers have also recently developed an insulin sensor based on a glassy carbon electrode (GCE) modified with guanine and nickel oxide nanoparticles,[82] however this sensor lacks the ability of carbon nanotubes to prevent biofouling. Finally, in our labs we have developed an insulin sensor based on multiwalled carbon nanotubes and incorporating a small vinyl monomer, dihydropyran (DHP), which aids in cohesion and results in a film thin enough to be incorporated

in miniaturized sensor designs,[53,55] as well as to withstand the shear forces present in a microfluidic system.[54]

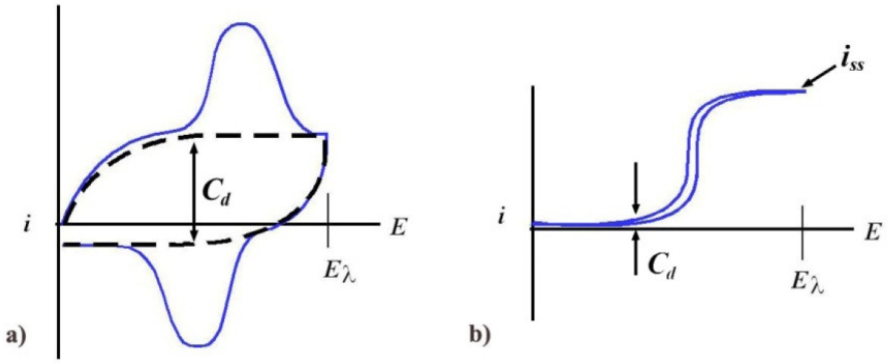

Figure 2.2; cyclic voltammograms for (a) macro and (b) ultramicroelectrodes. In (a) the dashed line shows the non-faradaic contribution to the total current measured. In (b) i_{ss} shows the steady-state current, and C_d shows the capacitance in both plots.

Ultramicroelectrodes

As the focus of investigation shifts from tissues and large numbers of cultured cells to individual cells, the quantities of targeted analytes become smaller and smaller, as do the currents generated during their detection. As these analytical signals are reduced the double-layer capacitance (C_d) of the electrodes, and for macro sized electrodes the non-faradaic currents they generate, becomes larger than the analytical signal (Fig. 2.2a), *i.e.,* the faradaic current due to the analyte gets 'buried' into the background non-faradaic current. The double-layer capacitance of a given electrode is a function of the radius (r) of the disc electrode and the interfacial capacitance of the electrolyte (C_d^0, typically 10 – 50 $\mu F/\text{cm}^2$),[83] shown in Eq. 2.2.

$$C_d = \pi r^2 C_d^0 \tag{2.2}$$

Given this equation, for example, decreasing the size of an electrode from 1 mm to 1 µm would cause a corresponding decrease in the double-layer capacitance by some six orders of magnitude (from approximately 1 µF to 1 pF). The corresponding reduction in the magnitude of background current has led to the design and implementation of smaller electrodes, which are called

ultramicroelectrodes (UMEs) if their diameter is smaller than 25 µm.[83] Due to their reduced size, they have drastically smaller capacitive charging currents (Fig. 2.2b), and thus have a higher sensitivity/lower limit of detection. Another difference between macro and UMEs is the relationship between their Faradaic current and diffusion. In the voltammogram shown in Fig. 2.2a, for the macro electrode, as the potential is swept, the current climbs initially, then falls off due to the reacted mediator blocking diffusion of fresh mediator to the electrode surface. The equivalent voltammogram for the UME (Fig. 2.2b) shows no diffusion limitation.

The desire to use UMEs in biological investigations, where carbon is often the electrode material of choice, has led to the development of the carbon fiber UME. Carbon fibers are typically 5 – 10 µm in diameter and are manufactured by heating threads of polymers, such as acrylonitrile/methyl methacrylate, in an anaerobic environment.[84] The heating process vaporizes most of the non-carbon atoms, and some of the carbon atoms, leaving behind fibers that are almost exclusively composed of crystalline carbon. Because of their small size, carbon fibers can be easily incorporated without further modification into UME designs. Passing the carbon fibers through a flame will also burn off some of the carbon, a process known as flame etching, allowing smaller electrode tips to be constructed from carbon fibers as well.[85,86]

Instrumental Platforms

The work presented here exclusively focuses upon electrochemical methods of analysis to study different biological systems, using two different instrumental platforms. Studies on large groups of cultured cells (300,000 – 500,000 in number), and on small groups of pancreatic islets (75 – 100), were performed using the MAMP. Smaller scale experiments were conducted on single pancreatic islets, single cultured cells, and analog ion channels in reconstituted bilayer lipid membranes (BLMs) using the SECM.

Multianalyte microphysiometer

The MAMP is a microfluidic platform for the electrochemical metabolic profiling of live cultured cells. The MAMP was developed by modifying an existing instrument, known as the Cytosensor Microphysiometer® (Molecular Devices, Sunnyvale, CA), which was originally released in 1990,[87] and has since been discontinued. The Molecular Devices instrument utilizes a light addressable potentiometric sensor (LAPS) to measure changes in the pH of a low-buffered media caused by the metabolic activity of the cells entrapped in the device, and was offered in either a 4-channel or 8-channel configuration. Although it was somewhat successful in its endeavors, the original instrument is limited in that it is only capable of measuring one metabolite, H^+.[24] While the use of extracellular acidification can be indicative of overall metabolic activity, it in no way allows the determination of which particular pathway is targeted in the event of a change in metabolic activity. A schematic of the cell chamber of the device is shown in Fig. 2.3.

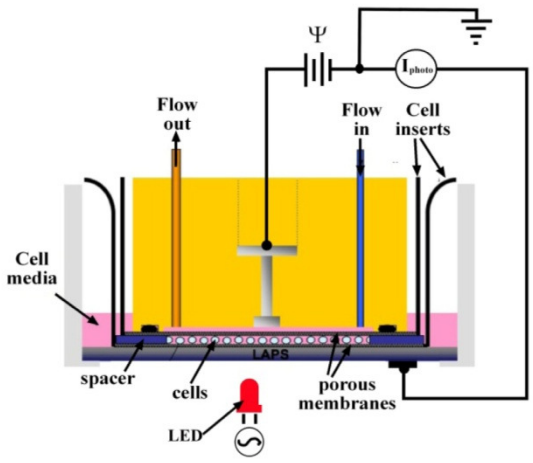

Figure 2.3; Schematic of the Cytosensor Microphysiometer LAPS sensor and sensor head assembly. The bias (Ψ) is applied between the CE in the sensor head and the base of the LAPS silicon, and the photocurrent (I_{photo}) is measured as a function of applied potential. The surface of the LAPS in contact with the solution is covered with an insulating Si oxynitride coating.

The LAPS, like a ChemFET,[88] is an insulated semiconductor device that responds to changes in polarization at its electrode/electrolyte interface (*i.e.*, surface potential) with a corresponding change in the electric field within the semiconductor itself.[89] When an appropriate bias (Ψ) is applied to the silicon, the majority of charge carriers at the insulator interface are depleted. In this state, a transient photocurrent (I_{photo}) can be generated in response to transient illumination of the silicon itself, due to the creation of e^-/ hole pairs by the incoming photons. In the case of the Cytosensor Microphysiometer®, the LAPS is an n-type doped silicon wafer topped with an oxynitride insulating coating. The oxynitride consists of Si–O and Si–NH_2 groups which can bind to H^+ ions present in solution, giving pH sensitivity to the electrode.

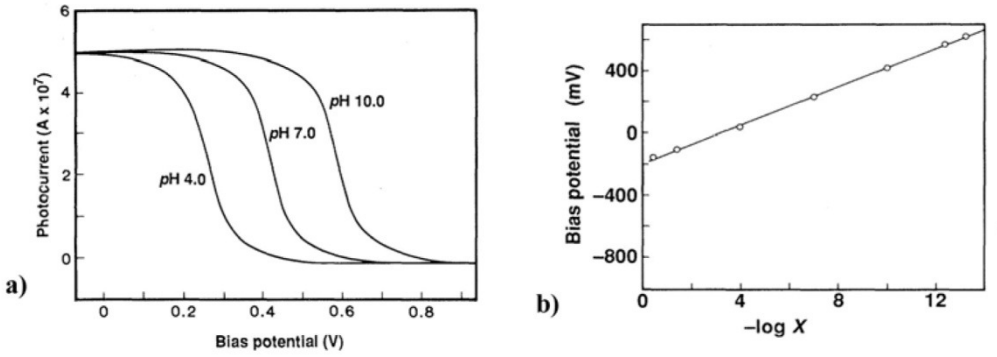

Figure 2.4; (a) the I_{photo} response as a function of Ψ at three different pH values. The value for Ψ at the inflection point is a function of solution pH. (b) a plot of inflection point potentials as a function of pH (log X, with X = $[H^+]$) for a series of solutions with pH values ranging from 2 – 12, illustrating a Nernstian response of 59 mV/pH unit @ 25 ºC. [Adapted from Hafeman][89]

The instrument utilizes a 3-electrode system, with the counter electrode (CE) directly above the LAPS and the reference electrode (RE) located downstream. In this configuration, Ψ is applied between the RE and the LAPS and I_{photo} is measured between the LAPS and electrical ground (see Fig. 2.3). Three overlaid voltammograms showing the I_{photo} response as a function of Ψ are shown in Fig. 2.4a for solutions with pH values of 4, 7, and 10. As Ψ is swept (from -100 mV to + 950 mV) I_{photo} decreases. The inflection point of the decrease in I_{photo} is pH dependent, and shifts toward more positive potentials as the pH of the solution increases. The shift in the

I_{photo} inflection point follows a Nernstian response of 59 mV per pH unit, as shown in the calibration plot in Fig. 2.4b, for the pH range of 2 – 12.[89]

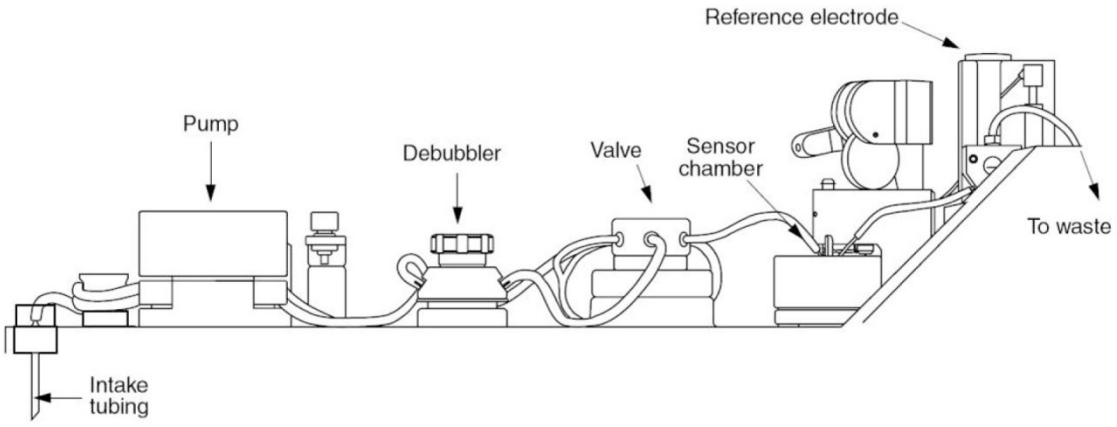

Figure 2.5; A schematic of a single channel of the original Molecular Devices Cytosensor Microphysiometer®, showing the media intake, peristaltic pump, debubblers, sensor chamber, and downstream RE [Adapted from Cytosensor Microphysiometer® manual].[87]

In addition to the LAPS, for each individual channel the instrument contains separate solution lines, peristaltic pumps, media debubblers, and separate heater/thermocouple controllers for the inline solution and the cell chamber itself (Fig. 2.5).[87] This enables multiple different experiments to be conducted simultaneously, limited of course by the number of available channels on the instrument. All instrumental functions are controlled by, and data are output to, proprietary software run on the Macintosh personal computer platform. The Cytosensor® also incorporates a RE filled internally with 2 M KCl rather than the typical 3 M KCl, in order to prevent salt creep frequently encountered with concentrated KCl solutions, and is placed downstream from the cell chamber in order to prevent excessive changes in the osmolality of the cell media which could be caused by KCl leeching from the electrode.

While the instrument was successful in the application of pH monitoring as an indicator of overall cellular metabolism, the lack of functionality with respect to additional analytes made further investigation into the specific modes of metabolic interference problematic. In order to

expand on the capabilities of the device, a series of modifications were made in our labs for the purpose of enabling the simultaneous measurement of multiple analytes.[22] A schematic of a simplified cellular metabolic pathway is shown in Fig. 2.6.[24] This figure depicts a simplified model of cellular energy pathways as monitored by four key biomarkers; oxygen, glucose, lactate, and H^+ production. Stock Molecular Devices sensor heads were modified to incorporate enzyme modified electrodes for lactate oxidase (LOx) and GOx (Pt discs, 0.5 mm), an electrode for oxygen determinations (Pt disc, 127 µm), and an additional CE (Pt disc, ~2 mm) to separate

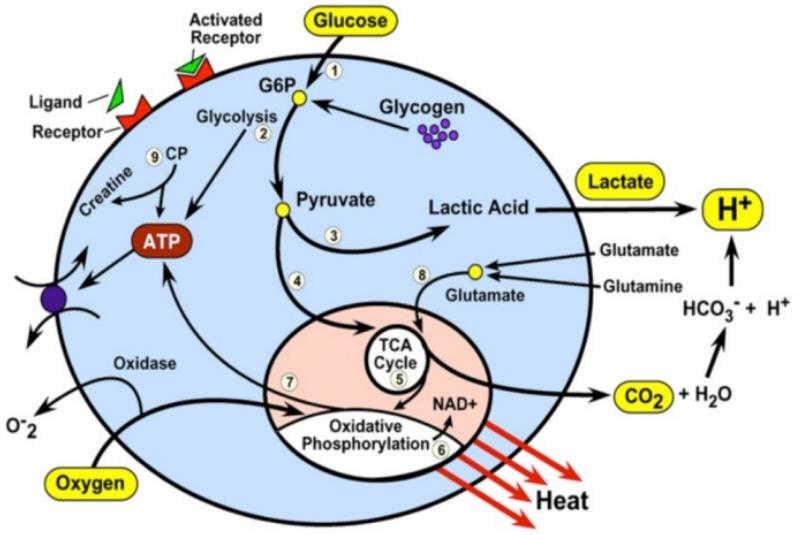

Figure 2.6; A simplified cellular metabolic pathway, showing how the monitoring of four biomarkers (oxygen, glucose, lactate, and extracellular acidification) can be used to follow changes in the metabolic activity of a live cell [Adapted from Eklund].[22]

cross-talk caused by the simultaneous operation of amperometric and LAPS sensors.[22-24,90] A photo of a modified sensor head is shown in Fig. 2.7. A dedicated multipotentiostat was also designed and implemented to allow simultaneous collection of amperometric signals in the instrument's 4 or 8-channel configurations.

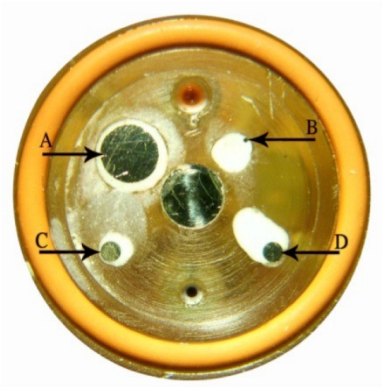

Figure 2.7; A modified Molecular Devices sensor head. The added electrodes include (A) a 2 mm Pt CE, (B) 127 µm Pt disc for oxygen, (C,D) 0.5 mm Pt discs for GOx and LOx electrodes.

The detection of glucose, lactate, and oxygen are accomplished via amperometry. Of the three only the detection of oxygen is done via direct reduction; at a Pt disc coated with Nafion® which acts as a barrier to biofouling. The resulting reaction at the electrode surface is most likely a 4 proton, 4 e^- process, as shown in equation 2.3.[83]

$$O_2 + 4H^+ + 4e^- \rightarrow 2H_2O \quad (E° = -500 \text{ mV } \textit{vs.} \text{ Ag/AgCl, 3 M KCl}) \tag{2.3}$$

Glucose and lactate detection is performed indirectly via enzyme modified electrodes, using GOx and LOx respectively. Since both enzymes produce H_2O_2, which is detected at the Pt disc electrode, they share the same potential bias. The detection is indirect in that the electrode senses the H_2O_2 produced by the enzyme, and not the substrate itself. The enzyme catalyzed reactions in the case of GOx and LOx respectively, and for electrochemical oxidation of hydrogen peroxide at the Pt electrode are the following:[83]

$$D-glucose + O_2 \xrightarrow{GOx} D-gluconolactone + H_2O_2 \tag{2.4}$$

$$L-lactate + O_2 \xrightarrow{LOx} pyruvate + H_2O_2 \tag{2.5}$$

$$H_2O_2 \rightarrow 2H^+ + O_2 + 2e^- \ (E° = +473 \text{ mV } \textit{vs.} \text{ Ag/AgCl, 3 M KCl})^{38} \tag{2.6}$$

The sensors are constructed by hand casting an aqueous gel matrix consisting of the enzyme, bovine serum albumin (BSA), and glutaraldehyde as a crosslinking agent onto their respective Pt

electrodes. A Nafion® layer may also be optionally added to the glucose oxidase film to prevent biofouling of the electrode.

All experiments performed in the MAMP, and in the Cytosensor Microphysiometer® as well, are done using a flow/stop-flow protocol that allows measurements to be performed in the absence of convection within the cell chamber. The general protocol utilizes 80 seconds of flow followed by 40 seconds of quiescence (stop-flow) while the measurements are being recorded. This also allows the buildup of cellular products and the greater depletion of glucose and oxygen due to metabolic activity, increasing the effective sensitivity of the electrodes over what would be possible in a continuous flow mode. This can be seen in Fig. 2.8 (solid line),[53] which depicts the response of a GOx electrode. At the initiation of the stop-flow (t = 0 s), the peristaltic pump cuts off and the supply of fresh glucose is stopped. During the stop-flow, the current decreases due to

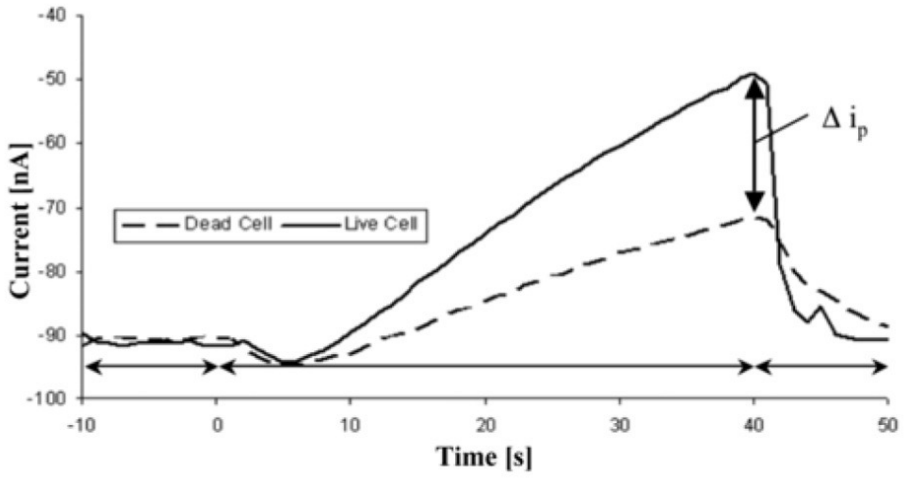

Figure 2.8; The response of a GOx enzyme electrode during a stop-flow cycle in the presence of live cells (solid line) and after the cells have been killed with alamethicin (dashed line).[53]

depletion of the solution glucose by both the processes at the enzyme electrode and to the cellular metabolism itself. At the end of the stop-flow (t = 40 s), the pump turns on, and the glucose in the chamber is replenished. In order to eliminate external factors (such as depletion of analyte by the electrode) from calculations of cellular metabolic rates, at the end of the experiment the cells

are killed by addition of alamethicin, a peptaibol antibiotic that is known to form water channels in the outer cell membrane,[91-93] to the extracellular media. The response of the same electrode after killing the cells is shown as the dashed line in Fig. 2.8. The difference between the '*dead cell*' stop-flow peak and the '*live cell*' peak (Δi_p) is then the portion of the Faradaic current that can be directly attributed to the metabolic activity of the cells themselves. Similar calculations are performed with the lactate and oxygen electrodes, to ensure that only the portion of the signal that can be attributed to the cell's activity is used to calculate metabolic rates. After the cells are killed, the sensors are then calibrated individually via standard addition to calculate the exact sensor response to be used in quantitative calculations.

Scanning electrochemical microscopy

SECM is a non-invasive variant of scanning probe microscopy developed by the Bard lab in 1989.[94,95] Although related to the scanning-tunneling microscope and the atomic force microscope, it utilizes non-destructive electrode potentials and operates exclusively in the non-contact imaging mode using UMEs as imaging tips. The current generated at the UME is a direct function of the concentration of the redox mediator and, unlike with macro-scale electrodes, is not affected by diffusion of mediator toward or away from the electrode tip. Because of the extremely small size of the electrode, the product diffuses away from the electrode tip as soon as it is formed, providing no hindrance to the incoming diffusion of fresh mediator. The current reaches a stable plateau instead, known as a *steady state current* (i_{ss}). The value of i_{ss} for a disc UME, at an infinite distance from a substrate ($i_{ss,\infty}$), is given by Eq. 2.7.[83]

$$i_{ss,\infty} = 4nFDCa \tag{2.7}$$

In the Eq. (2.7) n is the number of e^- transferred in the reaction, F is Faraday's constant (96,485 C mole^{-1}), D is the diffusion coefficient of the redox species (cm^2 s^{-1}), C is the concentration of the redox species in solution (mole·cm^3), and a is the radius of the UME's conductive tip (cm).

Using equation (2.7) at a 5 µm electrode (a = 2.5 µm) for a 1 mM solution of ferrocene (D = 1.70 × 10^{-05} cm^2 s^{-1}),[96] n = 1 and we would expect the following current:

$$i_{ss(\infty)} = 4(1)\left(96{,}485\,\frac{\text{C}}{\text{mole}}\right)\left(1.70\times10^{-5}\,\frac{\text{cm}^2}{\text{s}}\right)(10^{-6}\,\frac{\text{mole}}{\text{cm}^3})(2.5\times10^{-4}\text{cm}) = 1.6\text{ nA} \quad (2.8)$$

The current as the tip approaches a substrate will change, however, and it is this change that permits what Bard has termed the concept of 'feedback current imaging'.[95] This concept depends on the Faradaic current of a redox mediator and the diffusion of that mediator to and from the tip of an UME (Fig. 2.9a).[65] There are two different possibilities for the type of feedback one might experience during an SECM experiment when the UME tip is near a substrate. *Positive feedback* occurs between an UME and a conducting substrate (Fig. 2.9b). The redox mediator (O) diffuses

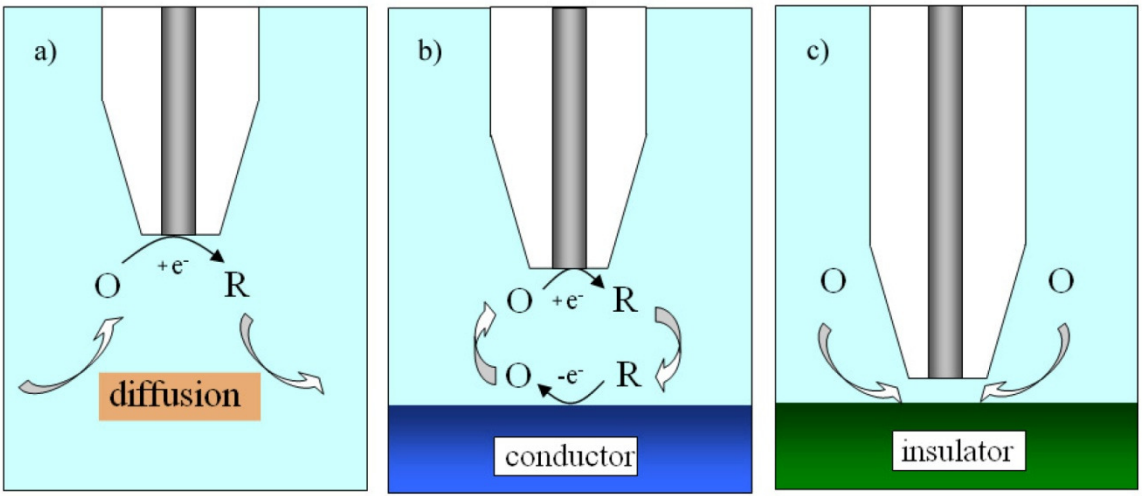

Figure 2.9; (a) the diffusion of the oxidized form of a redox mediator (O) to the biased tip of an UME where it gains an electron, converting it to the reduced form (R) and then diffuses away again. (b) the concept of positive feedback over a conductive substrate. (O) diffuses to the UME tip, where it gains an electron converting it to (R), which can diffuse to the conductive substrate and be regenerated as (O). This creates a positive feedback loop, increasing the faradaic current as the UME approaches the substrate. (c) the concept of negative feedback, where an insulating substrate blocks the flow of (O) to the electrode surface, limiting the extent of the reaction, and thus the Faradaic current generated [Adapted from Nagy].[65]

to the tip, which is biased at a potential that converts the mediator to its reduced form (R). The conductive substrate, if properly biased, can then regenerate (R) to its original form as (O) via oxidation. The extent of regeneration, and thus the magnitude of current generated, depends upon the distance between the UME tip and the substrate. *Negative feedback* occurs in the event the

UME is close to an insulating substrate (Fig. 2.9c). The mediator (O) diffuses to the tip, which like the previous case is biased, driving its conversion to (R). When the UME is in close proximity to the substrate, however, there is a restriction in the flow of (O) to the UME tip, creating a diffusional hinderance that effectively reduces the Faradaic current. Additionally, since the substrate is not conductive it can not drive the reverse reaction, and (R) will simply diffuse into the bulk of the solution. The combined effects of the diffusional hinderance and lack of mediator recycling leads to a dramatic decrease in current as the UME tip approaches the substrate surface.

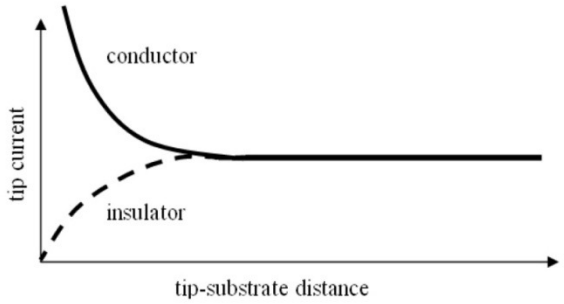

Figure 2.10; The faradaic current passed as an UME approaches a conductive substrate (solid line) and an insulating substrate (dashed line) [adapted from Nagy].[65]

The ability of both *positive feedback* and *negative feedback* to produce images can be shown by observing how the Faradaic current changes as the tip approaches each type of substrate (Fig 2.10).[94] As the UME approaches a conductive substrate (solid line), the extent of redox mediator that reaches the substrate for regeneration increases, while the distance it must travel between the two is reduced, creating a feedback effect. This *positive feedback* loop then causes a nearly exponential increase in Faradaic current as the UME approaches to within one tip diameter of the substrate. In the case of an insulating substrate, as the UME gets closer and closer to the substrate, there is an increasing blockage of the diffusion of unreacted redox mediator to the tip, resulting in a drastic decrease in measured Faradaic current at the UME tip. In either case, the Faradaic tip current (i_{tip}) is a function of the UME to substrate distance, and

therefore the current can be recorded and used to create a topographical image. In order to generate an SECM image, the tip is scanned in a raster pattern in the X and Y dimensions while maintaining a constant Z-axis position (*i.e.,* constant height mode), using either piezo-electric inchworm motors, or precision stepper motors (Fig 2.11). While the tip is being scanned, the current is recorded as a function of its position in the X-Y plane.

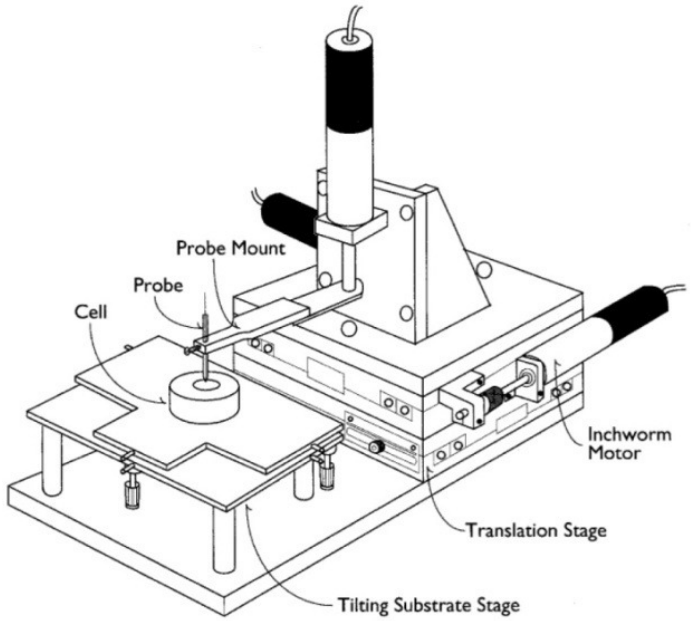

Figure 2.11; Schematic of the inchworm piezo stage of the commercial available CH Instruments SECM. Each axis is controlled by an individual inchworm. The *x-* and *y-axis* inchworms are connected to a sliding translation stage, while the *z-axis* is connected to the UME via a probe mount [adapted from Bard].[83]

Additionally, SECM imaging may be accomplished in either *constant height* or *constant distance* modes, depending on the capabilities of the instrument (Fig. 2.12). First generation SECM instruments, including those used for the work presented here, are capable of only *constant height* imaging. In this imaging mode the UME tip is held at a constant position vertically while rastering horizontally in the x-y plane to collect data (the solid line in Fig. 2.12). No matter the variation in topography, the z-axis position of the UME probe will not change.

Since the current signal is dependent on the tip-surface distance, image resolution will suffer in areas where the surface being imaged is farther from the UME tip (area shaded red in Fig. 2.12). The addition of a z-axis feedback loop to the instrument, present in second generation SECM instruments, allows the z-axis tip-substrate distance to remain constant (dotted line in Fig. 2.12). This allows the tip to be maintained at the ideal distance from the substrate (1–2 tip diameters)[97] for maximum image resolution (area shaded yellow in Fig. 2.12). In this imaging mode, topographical and chemical data may be collected simultaneously by recording the UME z-axis tip deflection along with tip current. There are differing methods to accomplish constant distance imaging, including *constant current* mode,[97] dampening of tip modulation,[98] and monitoring AC tip impedance.[99-101]

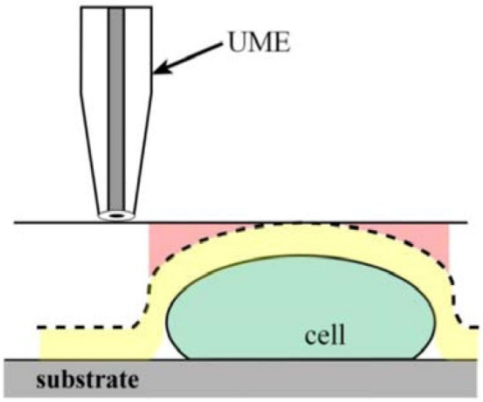

Figure 2.12; Constant height *vs.* constant distance imaging modes. In constant height mode (solid line), the *z-axis* position of the UME is fixed. In constant distance mode (dotted line), the *z-axis* distance is constantly modulated to maintain a constant tip-substrate distance. Since the signal generated in imaging is distance dependant, it is critical to maintain tip-substrate separation within 1-2 tip diameters (yellow shaded area). When that tip distance is exceeded in constant height mode (red shaded area), image resolution will suffer.

Although the SECM was initially applied to biological investigations soon after being introduced,[102] more recent investigations have led to specialized instrumental configurations for biological investigations, termed biological scanning electrochemical microscopes (Bio-SECM).[101] Under most circumstances, in biological applications topographical imaging is always performed in the *negative feedback* mode due to the insulating nature of biological surfaces.

Topographical imaging, however, is neither the only nor the most useful aspect of Bio-SECM. Another, more biologically relevant, feature of Bio-SECM is accomplished via generation-collection (GC) mode[97] (Fig. 2.13). In this technique, a redox molecule or biomarker is generated

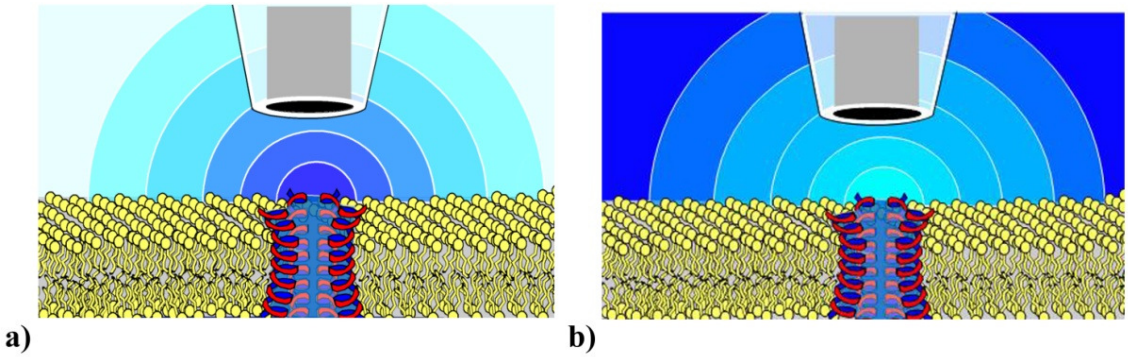

Figure 2.13; GC-imaging mode utilizes a substance generated at the substrate. In the case of biological imaging, the substance may either be (a) produced by the cell or (b) consumed by the cell.

by the substrate or in our case the biological entity (red plume in Fig 2.13), and collected at the UME tip via an electrochemical reaction. This produces a diffusional gradient, with the highest concentration at the source of production.[103] Alternately, if the biological subject is consuming the substance instead of generating it an inverse diffusional gradient will be seen, with the maximum concentration in the bulk solution and the minimum concentration at the point of uptake (not shown). In the case of oxygen respiration, where the oxygen molecules freely diffuse through the entire cell membrane, a uniform area of depletion is seen surrounding the cell.[25,30,104] The GC imaging mode therefore allows monitoring of actual biological processes in real-time, and therefore generation of *spatio-temporal* maps of biological activity across the surface of a live cell or organism.

The adaptation of Bio-SECM to metabolomic studies will allow a critical jump to be made from the macro scale to the ultramicro scale. Previous methods like GC/MS, NMR, or even MAMP all are limited in their sensitivities, as well as their ability to track metabolic changes in real time. While more than adequate to study tissue samples, or even large numbers of cultured

cells, these techniques lack the ability to be employed in the investigation of single-cell metabolic studies. While it is true that *in vivo* cells are constantly in contact with other cells via messaging, the ability to understand what happens on the single cell level is critical to understanding the inner mechanisms of cellular metabolism, and determining the extent of variations in metabolic activity within individual cellular phenotypes. Also in addition to increased sensitivity, the Bio-SECM promises the ability to study biochemical activity on a spatial as well as temporal scale.

References

(1) Danneel, H. *Z. Elektrochem.* **1897-98**, *3*, 227.
(2) Heyrovsky, J.; Shikata, M. *Rec. trav. Chim., Pays,-Bas.* **1925**, *44*, 496.
(3) Baumberger, J. P. *J. Gen. Physiol.* **1933**, *17*, 1-6.
(4) Muller, O. H.; Baumberger, J. P. *Trans. Electrochem. Soc.* **1937**, *71*, 12.
(5) Muller, O. H.; Baumberger, J. P. *Trans. Electochem. Soc.* **1937**, *71*, 14.
(6) Baumberger, J. P. *Cold Spring Harbor Symposia on Quantitative Biology* **1939**, *7*, 195-215.
(7) Winzler, R. J.; Baumberger, J. P. *J. Cell. Comp. Physiol.* **1938**, *12*, 183-211.
(8) Silver, I. A. *Phys. Med. Biol.* **1967**, *12*, 285-299.
(9) Davies, P. W.; Brink, F., Jr. *Rev. Sci. Inst.* **1942**, *13*, 524-533.
(10) Clark, L. C., Jr.; Helmsworth, J. A.; Kaplan, S.; Sherman, R. T.; Taylor, Z. *Surg. Forum* **1953**, *4*, 93-96.
(11) Clark, L. C., Jr.; Wolf, R.; Granger, D.; Taylor, Z. *J. Appl. Physiol.* **1953**, *6*, 189-193.
(12) Clark, L. C., Jr.; Kaplan, S.; Matthews, E. C.; Schwab, L. *J. Thorac. Surg.* **1956**, *32*, 576-582.
(13) Clark, L. C., Jr. *Surg. Forum* **1960**, *11*, 143-144.
(14) Clark, L. C., Jr.; Clark, E. W. *Ala. J. Med. Sci.* **1964**, *1*, 142-148.
(15) Clark, L. C., Jr.; Becattini, F. *Ala. J. Med. Sci.* **1967**, *4*, 337-339.
(16) Litong, J.; Ping, J.; Jiannong, Y.; Yuzhi, F. *Talanta* **1992**, *39*, 145-147.
(17) Parthasarathy, A.; Dave, B.; Srinivasan, S.; Appleby, A. J.; Martin, C. R. *Journal of the Electrochemical Society* **1992**, *139*, 1634-1641.
(18) Yoshia, I.; Shimada, Y.; Tanaka, K. *Med. Biol. Eng. Comp.* **1980**, *18*, 27-32.
(19) Hutter, E.; Renner, K.; Pfister, G. *Biochem. J.* **2004**, *380*, 919.
(20) Kuznetsov, A. V.; Strobl, D.; Ruttmann, E. *Anal. Biochem.* **2002**, *305*, 186.
(21) Zacharovova, K.; Berkova, Z.; Spacek, T.; Kriz, J.; Dovolilova, E.; Girman, P.; Koblas, T.; Jezek, P.; Saudek, F. *Transplant. P.* **2005**, *37*, 3454-3456.
(22) Eklund, S. E.; Cliffel, D. E.; Kozlov, E.; Prokop, A.; Wikswo, J. P.; Baudenbacher, F. *Anal. Chim. Acta* **2003**, *496*, 93-101.
(23) Eklund, S. E.; Kozlov, E.; Taylor, D. E.; Baudenbacher, F.; Cliffel, D. E. *Methods Mol. Biol.* **2005**, *303*, 209-223.
(24) Eklund, S. E.; Taylor, D.; Kozlov, E.; Prokop, A.; Cliffel, D. E. *Anal. Chem.* **2004**, *76*, 519-527.
(25) Ciobanu, M.; Taylor, D. E., Jr.; Wilburn, J. P.; Cliffel, D. E. *Anal. Chem.* **2008**, *80*, 2717-2727.
(26) Amemiya, S.; Guo, J.; Xiong, H.; Gross, D. A. *Anal. Bioanal. Chem.* **2006**, *386*, 458-471.

(27) Bard, A. J.; Li, X.; Zhan, W. *Biosens. Bioelectron.* **2006**, *22*, 461-472.
(28) Holt, K. B.; Bard, A. J. *Biochemistry* **2005**, *44*, 13214-13223.
(29) Torisawa, Y. S.; Shiku, H.; Yasukawa, T.; Nishizawa, M.; Matsue, T. *Biomat.* **2005**, *26*, 2165-2172.
(30) Kaya, T.; Numai, D.; Nagamine, K.; Aoyagi, S.; Shiku, H.; Matsue, T. *Analyst* **2004**, *129*, 529-534.
(31) Kaya, T.; Nagamine, K.; Oyamatsu, D.; Shiku, H.; Nishizawa, M.; Matsue, T. *Lab Chip* **2003**, *3*, 313-317.
(32) Torisawa, Y. S.; Shiku, H.; Kasai, S.; Nishizawa, M.; Matsue, T. *Int. J. Cancer* **2004**, *109*, 302-308.
(33) Kaya, T.; Torisawa, Y. S.; Oyamatsu, D.; Nishizawa, M.; Matsue, T. *Biosens. Bioelectron.* **2003**, *18*, 1379-1383.
(34) Torisawa, Y. S.; Kaya, T.; Takii, Y.; Oyamatsu, D.; Nishizawa, M.; Matsue, T. *Anal. Chem.* **2003**, *75*, 2154-2158.
(35) Kaya, T.; Nishizawa, M.; Yasukawa, T.; Nishiguchi, M.; Onouchi, T.; Matsue, T. *Biotechnol. Bioeng.* **2001**, *76*, 391-394.
(36) Clark, L. C., Jr.; Lyons, C. *Ann. NY Acad. Sci.* **1962**, *102*, 29-45.
(37) Griffin, J. *Drug Discov. Today* **2004**, *1*, 285-293.
(38) "Electrochemical Series", in *CRC Handbook of Chemistry and Physics*, (*87th Edition*), Lide, D. R. ed.,Taylor and Francis, Boca Raton, FL.
(39) Ohara, T. J.; Rajagopalan, R.; Heller, A. *Anal. Chem.* **1994**, *66*, 2451-2457.
(40) Ho, W. O.; Athey, D.; McNeil, C. J.; Hager, H. J.; Evans, G. P.; Mullen, W. H. *J. Electroanal. Chem.* **1993**, *351*, 185-197.
(41) Cuhna, D. A.; Carniero, E. M.; Alves, M. d. C.; Jorge, A. G.; Morais de Sousa, S.; Boschero, A. C.; Saad, M. J. A.; Velloso, L. A.; Rocha, E. M. *Am. J. Physiol.* **2005**, *289*, E768-E775.
(42) Porksen, N.; Nyholm, B.; Veldhuis, J. D.; Butler, P. C.; Schmitz, O. *Am. J. Physiol. Endocrinol. Metab.* **1997**, *273*, E908-E914.
(43) Yang, C.; Huang, H.; Zhang, H.; Liu, M. *Anal. Lett.* **2006**, *39*, 2463-2473.
(44) Gorski, W.; Aspinwall, C. A.; Lakey, J. R. T.; Kennedy, R. T. *Electroanal. Chem.* **1997**, *425*, 191-199.
(45) Huang, L.; Shen, H.; Atkinson, M. A.; Kennedy, R. T. *Proc. Natl. Acad. Sci. U.S.A.* **1995**, *92*, 9608-9612.
(46) Qian, W.-J.; Peters, J. L.; M., D. G.; Gee, K. R.; Kennedy, R. T. *Biotechniques* **2004**, *37*, 922-933.
(47) Roper, M. G.; Shackman, J. G.; Dahlgren, G. M.; Kennedy, R. T. *Anal. Chem.* **2003**, *75*, 4711-4717.
(48) Shackman, J. G.; Dahlgren, G. M.; Peters, J. L.; Kennedy, R. T. *Lab Chip* **2005**, *5*, 55-63.
(49) Brothers, S. P.; Janovick, J. A.; Conn, P. M. *J Clin Endocrinol Metab* **2003**, *88*, 6107-6112.
(50) Koller, K. J.; Whitehorn, E. A.; Tate, E.; Ries, T.; Aguilar, B.; Chernov-Rogan, T.; Davis, A. M.; Dobbs, A.; Yen, M.; Barrett, R. W. *Anal Biochem* **1997**, *250*, 51-60.
(51) Romano, J. D.; Schmidt, W. K.; Michaelis, S. *Mol Biol Cell* **1998**, *9*, 2231-2247.
(52) Tolbert, L. M.; Lameh, J. *J Neurochem* **1998**, *70*, 113-119.
(53) Ciobanu, M.; Wilburn, J. P.; Snider, M. T.; Cliffel, D. E.,*Multianalye microphysiometry of pancreatic islets*, Vanderbilt University, 2008, *unpublished work*.
(54) Snider, R. M.; Ciobanu, M.; Rue, A. E.; Cliffel, D. E. *Anal. Chim. Acta.* **2008**, *609*, 44-52.
(55) Wilburn, J. P.; Ciobanu, M.; Cliffel, D. E.,*Scanning Electrochemical Microscopy of Pancreatic Islets*, Vanderbilt University, 2008, *unpublished work*.

(56) Barbosa, R. M.; Silva, A. M.; Tome, A. R.; Stamford, J. A.; Santos, R. M.; Rosario, L. M. *Biochem. Biophys. Res. Commun.* **1996**, *228*, 100-104.
(57) Hellman, B.; Lernmark, A.; Sehlin, J.; Taljedal, I. B. *Biochem Pharmacol* **1972**, *21*, 695-706.
(58) Lundquist, I.; Ekholm, R.; Ericson, L. E. *Diabetologia* **1971**, *7*, 414-422.
(59) Lernmark, A. *Horm Metab Res* **1971**, *3*, 305-309.
(60) Maghasi, A. T.; Halsall, H. B.; Heineman, W. R.; Rodriguez-Rolob, H. L. *Anal. Biochem.* **2004**, *326*, 183-189.
(61) Cheng, L.; Pacey, G. E.; Cox, J. A. *Anal. Chem.* **2001**, *73*, 5607-5610.
(62) Cox, J. A.; Gray, T. *Anal. Chem.* **1989**, *61*, 2462-2464.
(63) Pikulski, M.; Gorski, W. *Anal. Chem.* **2000**, *72*, 2696-2702.
(64) Elsen, H. A.; Slowinska, K.; Hull, E.; Majda, M. *Anal. Chem.* **2006**, *78*, 6356-6363.
(65) Nagy, Z.; You, H. *Electrochim. Acta* **2002**, *47*, 3037-3055.
(66) Hobkirk, J. A. *J. Dent.* **1975**, *3*, 271-287.
(67) Kenner, G. H.; Brown, S. D.; Pasco, W. D.; Marshall, A. E.; Lovell, J. E. *J Biomed Mater Res* **1975**, *9*, 111-120.
(68) Lauslahti, K.; Patiala, H.; Rokkanen, P.; Tarvainen, T.; Rautavuori, J.; Tormala, P. *Ann. Biomed. Eng.* **1983**, *11*, 495-498.
(69) Sakas, D. E.; Simpson, B. A.; Krames, E. *Operative Neuromodulation, Volume 2: Neural Networks Surgery*; Springer: New York, 2007.
(70) Ikarashi, Y.; Iwatsuki, H.; Blank, C. L.; Maruyama, Y. *J Chromatogr* **1992**, *575*, 29-37.
(71) Wang, J.; Bonakdar, M. *Talanta* **1988**, *35*, 277-280.
(72) Kovach, P. M.; Ewing, A. G.; Wilson, R. L.; Wightman, R. M. *J Neurosci Methods* **1984**, *10*, 215-227.
(73) Marsden, C. A.; Bennett, G. W.; Brazell, M.; Sharp, T.; Stolz, J. F. *J Physiol (Paris)* **1981**, *77*, 333-337.
(74) Wightman, R. M.; Jankowski, J. A.; Kennedy, R. T.; Kawagoe, K. T.; Schroeder, T. J.; Leszczyszyn, D. J.; Near, J. A.; Diliberto, E. J., Jr.; Viveros, O. H. *Proc Natl Acad Sci U S A* **1991**, *88*, 10754-10758.
(75) Kawagoe, K. T.; Jankowski, J. A.; Wightman, R. M. *Anal Chem* **1991**, *63*, 1589-1594.
(76) Moore, L. C.; Clausen, C.; Bowden, E. F.; Birzgalis, A. *Am J Physiol* **1987**, *252*, F1158-1166.
(77) Chen, R. S.; Huang, W. H.; Tong, H.; Wang, Z. L.; Cheng, J. K. *Anal Chem* **2003**, *75*, 6341-6345.
(78) Wang, J.; Musameh, M. *Anal. Chim. Acta* **2004**, *511*, 33-36.
(79) Zhang, R.; Wang, X.; Shiu, K. K. *J Colloid Interface Sci* **2007**, *316*, 517-522.
(80) Zhu, J. J.; Xu, J. Z.; Hu, Z.; Chen, H. Y. *Front Biosci* **2005**, *10*, 521-529.
(81) Wang, J.; Tangkuaram, T.; Loyprasert, S.; Vazquez-Alvarez, T.; Veerasai, W.; Kanatharana, P.; Thavarungkul, P. *Anal. Chim. Acta* **2007**, *581*, 1-6.
(82) Salimi, A.; Noorbakhash, A.; Sharifi, E.; Semnani, A. *Biosens. Bioelectron.* **2008**, *24*, 792-798.
(83) Bard, A. J.; Faulkner, L. R. *Electrochemical Methods; Fundamentals and Applicaitons*, 2d. ed. ed.; John Wiley & Sons, Inc.: New York, NY, 2001.
(84) Edie, D. D. *Carbon* **1998**, *36*, 345-362.
(85) Strand, A. M.; Venton, B. J. *Anal Chem* **2008**, *80*, 3708-3715.
(86) Huang, W. H.; Pang, D. W.; Tong, H.; Wang, Z. L.; Cheng, J. K. *Anal Chem* **2001**, *73*, 1048-1052.
(87) Cytosensor Microphysiometer System; User's Manual; Molecular Devices Corporation: Sunnyvale CA, 1995.
(88) McKinley, B. A.; Saffle, J.; Jordan, W. S.; Janata, J.; Moss, S. D.; Westenskow, D. R. *Med Instrum* **1980**, *14*, 93-97.

(89) Hafeman, D. G.; Parce, J. W.; McConnell, H. M. *Science* **1988**, *240*, 1182-1185.
(90) Eklund, S. E.; Snider, R. M.; Wikswo, J. P.; Baudenbacher, F.; Prokop, A.; Cliffel, D. E. *J. Electroanal. Chem.* **2006**, *587*, 333-339.
(91) Bak, M.; Bywater, R. P.; Hohwy, M.; Thomsen, J. K.; Adelhorst, K.; Jakobsen, H. J.; Sorensen, O. W.; Nielsen, N. C. *Biophys J* **2001**, *81*, 1684-1698.
(92) Mueller, P.; Rudin, D. O. *Nature (London, U. K.)* **1968**, *217*, 713-719.
(93) Tieleman, D. P.; Berendsen, H. J. C.; Sansom, M. S. P. *Biophys J* **2001**, *80*, 331-346.
(94) Bard, A. J.; Denuault, G.; Friesner, R. A.; Dornblaser, B. C.; Tuckerman, L. S. *Anal Chem* **1991**, *63*, 1282-1288.
(95) Bard, A. J.; Fan, F. R.; Pierce, D. T.; Unwin, P. R.; Wipf, D. O.; Zhou, F. *Science* **1991**, *254*, 68-74.
(96) Mirkin, M. V.; Richards, T. C.; Bard, A. J. *Phys. Chem.* **1993**, *97*, 7672.
(97) Bard, A. J.; Mirkin, M. V., Eds. *Scanning Electrochemical Microscopy*; Marcel Dekker: New York, 2001.
(98) Ballesteros Katemann, B.; Schulte, A.; Schuhmann, W. *Chemistry* **2003**, *9*, 2025-2033.
(99) Ervin, E. N.; White, H. S.; Baker, L. A. *Anal Chem* **2005**, *77*, 5564-5569.
(100) Ervin, E. N.; White, H. S.; Baker, L. A.; Martin, C. R. *Anal Chem* **2006**, *78*, 6535-6541.
(101) Kurulugama, R. T.; Wipf, D. O.; Takacs, S. A.; Pongmayteegul, S.; Garris, P. A.; Baur, J. E. *Anal. Chem.* **2005**, *77*, 1111-1117.
(102) Lee, C.; Kwak, J.; Bard, A. J. *Proc. Natl. Acad. Sci. U.S.A.* **1990**, *87*, 1740-1743.
(103) Wilburn, J. P.; Wright, D. W.; Cliffel, D. E. *Analyst* **2006**, *131*, 311-316.
(104) Takii, Y.; Takoh, K.; Nishizawa, M.; Matsue, T. *Electrochim. Acta* **2003**, *48*, 3381-3385.

CHAPTER III

ORGANOPHOSPHATE TOXICITY STUDIES *VIA* MULTIANALYTE MICROPHYSIOMETRY *

Due to the relationship between the health of an organism and a balanced metabolism, individual elements (*i.e.*, metabolic precursors or products) of the biological metabolic pathway (*e.g.*, biomarkers) can be utilized to study, detect, and diagnose diseases and metabolic disorders.[1-5] In addition to dysfunctions originating from live pathogens, such as a virus or bacteria, metabolic profiling can also be utilized to detect the presence of, or study the effects of, a chemical toxin.[6-10] The techniques of the emerging field of metabolomics, therefore, with their unique focus on the detection of subtle changes in cellular metabolism, are optimally suited for this method of investigation.[11-16]

Background

OP toxins are esters of phosphoric acid (Fig. 3.1), with applications including insecticides, pesticides, herbicides, and biological nerve agents. Large dose exposure to OP compounds has been shown to rapidly induce neurotoxicity in humans,[17-20] and long-term exposure to sub-lethal levels leads to a condition known as neuropathy,[21] which is marked by a deranged function of neural and motor activity. While there have been recent studies focusing on elucidation of the specific neurochemical pathways implicated in OP toxicity,[22,23] the significance of these pathways is not yet completely understood.[24] Without an in-depth knowledge of the

---

*This project was a collaborative effort involving both the collection of experimental data and the use of data to generate and evaluate an intracellular pathway model. The portions of this chapter concerning the development (section 3.B) and the validation (section 3.D.2) of the model are solely the work of J. W. Jenkins, J. E. Hood, and S. Sundaram of the CFD Research Corporation. They remain here, as opposed to placed in an appendix, because they are critical to explaining the motivation for the research and to assist in evaluation of results.

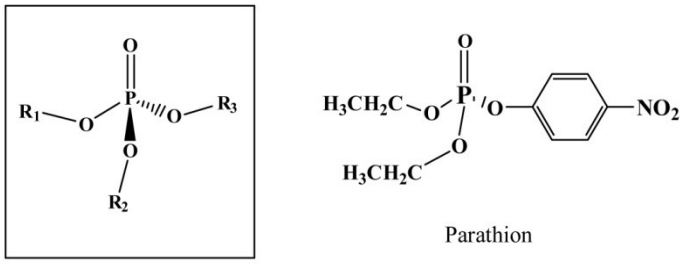

Figure 3.1; OP compounds are esters of phosphoric acid with three possible substituent groups. OP compounds utilized in these toxicity studies were parathion (R_1 and R_2 are ethyl, and R_3 is paranitrophenyl).

pathways involved, the development of therapeutic agents is currently done via combinatorial investigations,[25-27] in a more or less trial and error methodology. This study aims to combine experimental measurements and computational analysis of cellular processes in order to better understand the mechanism of OP-induced neurotoxicity and to point the way toward pharmacological targets for therapeutics/protectants.

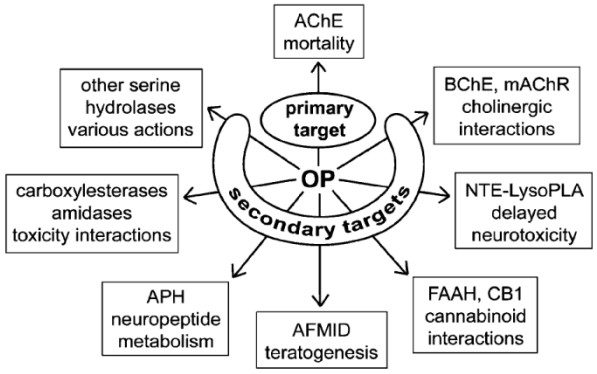

Figure 3.2; A schematic of the primary and known secondary targets for OP-induced neurotoxicity.

OP compounds are known to induce toxicity primarily through inhibition of acetylcholinesterase (AChE) in the plasma membrane of neural cells.[28-31] AChE itself is a highly active enzyme that degrades excess acetylcholine (ACh) present in the synapse. With AChE blocked, excess synaptic ACh rapidly over stimulates both nicotinic (nAChR) and muscarinic (mAChR) cholinergic receptors.[32-35] In addition to the primary target of AChE, there are multiple secondary targets of OP compounds as well[36,37] (Fig. 3.2). Studies utilizing $AChE^-$ knockout

mice (mice lacking AChE) have shown a higher susceptibility toward OP-induced toxicity in mice without AChE,[38] strongly suggesting alternate modes of action. Butyryl cholinesterase (BChE), which also works on ACh, has been implicated as a possible secondary target resulting in acute OP-induced toxicity.[38-40] Additionally, delayed neuropathy is thought to be linked to OP action through neuropathy target esterase (NTE), which although associated with the nervous system is distinct from AChE.[41-44] It is also known that chlorpyrifos (see Fig. 3.1), a specific OP compound, acts directly upon multiple components of the adenylyl cyclase cascade,[45-48] which helps to control intracellular calcium levels via regulation of the production and degradation of cAMP. Chlorpyrifos' modes of action include direct modulation of adenylyl cyclase activity, affecting functions of G-proteins linking neurotransmitters and hormones to cyclase activity, and the expression of neurotransmitter receptors acting within the cascade.[49,50]

Stimulation of either nAChR or mAChR will result in an increase in intracellular Ca^{2+} concentration[51-53] (Fig. 3.3). The source of the increase, however, is different for each receptor system. For the nAChR system, stimulation results in an opening of the nicotinic ligand-gated ion channel and a subsequent influx of Na^{+}, which depolarizes the cell membrane causing L-type voltage-dependent Ca^{2+} channels to open.[54] Conversely mAChR targeting results in activation of phospholipase C (PLC) and resulting in the hydrolysis of phosphatidylinositol biphosphate (PIP_2) to inositol triphosphate (IP_3) and diacylglycerol (DAG).[55,56] Newly produced IP_3 binds to (and opens) the IP_3-dependent Ca^{2+} channel located on the endoplasmic reticulum. This, in turn, releases stored Ca^{2+} which effectively increases the intracellular concentration. Regardless of the mode of action, overstimulation of cholinergic receptors by excess ACh in the cholinergic synapse has been shown to disrupt normal cellular calcium function in PC12 cells.[57,58]

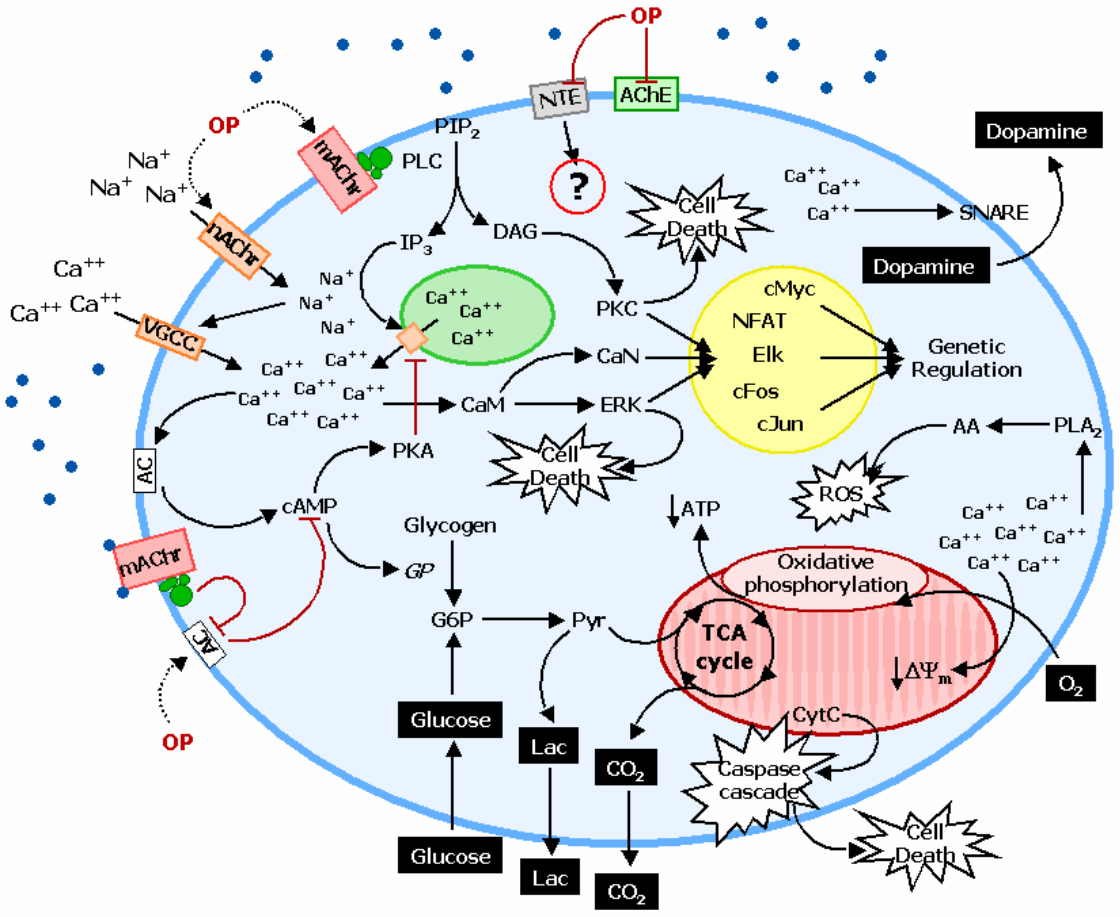

Figure 3.3; a graphic depiction of the modes of action of OP-induced neurotoxicity upon nAChR and mAChR.

In neuronal cells normative changes in intracellular Ca^{2+} concentration drive a diverse set of cellular responses, including modulation of the rate of cellular metabolic processes, the induction of cellular signaling cascades, and increases in neurotransmitter release such as dopamine,[59] GABA, and aspartate.[60] When intracellular Ca^{2+} levels are high for long periods of time, however, the cell becomes susceptible to a wide variety of cytotoxic phenomena, including "pathological" protein phosphorylation,[61] which leads to cell death.[62] Other problems with long-term elevated levels of intracellular Ca^{2+} include increased calmodulin (CaM) activity,[63-65] sustained protein phosphorylation[66] and excessive reactive oxygen species (ROS) formation.[62] ROS, in particular, have been shown to cause mitochondrial damage and impairment of metabolic function,[67] and excessive ROS formation can lead to caspase-dependent cell death.[68] Finally,

increased intracellular Ca^{2+} leads to activation of transcriptional factors through mitogen-activated protein (MAP) kinase cascades and upregulation of tyrosine hydroxylase activity.[69-71]

OP cytotoxicity is also responsible for the release of catecholamines from PC12 cells through a prolonged increase in intracellular Ca^{2+} concentration.[59,60] Catecholamines (*e.g.*, dopamine) are produced from tyrosine through a series of enzymatic reactions.[72-74] Tyrosine is converted to 3,4-dihydroxyphenylalanine (DOPA) through the action of tyrosine hydroxylase (regulated by PKC, PKA and kinase cascades).[69-71] DOPA can then be converted to dopamine through the action of DOPA decarboxylase. Dopamine can be further metabolized to norepinephrine. Once produced, the catecholamines are stored in granules located near the plasma membrane. The release of catecholamines through exocytosis is driven by a transmembrane proton gradient created by the activity of an ATPase in the granules.[75] Intracellular Ca^{2+} catalyzes the granule/cell membrane fusion event by activating the Ca^{2+}-dependent soluble N-ethylmaleimide-sensitive fusion (SNARE) complex.[76] OP-induced release of large quantities of catecholamines increases the extracellular concentration of catecholamines, ultimately leading to well-documented long term cytotoxic effects in diseases such as Parkinson's.[77]

Development of Intracellular Pathway Model

Once the primary intracellular pathways and processes involved in OP cytotoxicity have been identified, the individual pieces of the pathway are coalesced into a quantitative dynamic intracellular pathway model. The pathways summarized below focus primarily on the down-stream effects of the inhibition of AChE. Pathway connectivity was fully prescribed for the pathways identified during the literature search.

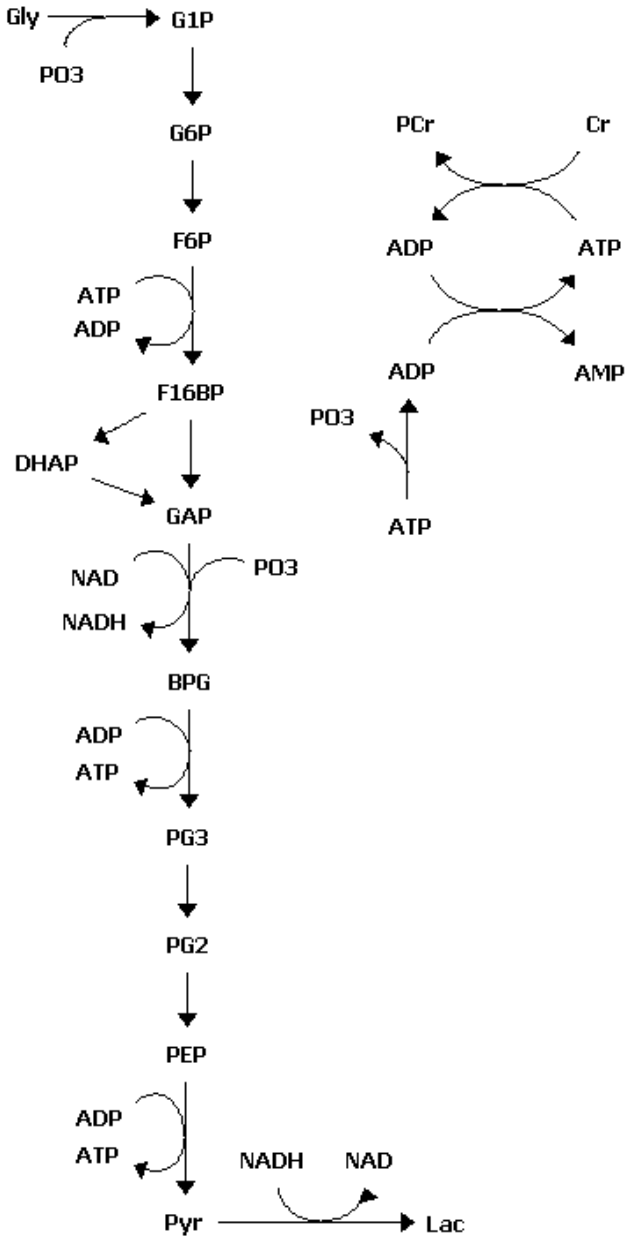

Figure 3.4; Model of Glycolysis pathway [adapted from Lambeth[25]]

Central Carbon Metabolism

The glycolysis model (Fig. 3.4) used in this work is modeled after the one originally proposed by Lambeth.[78] It contains validated equations for each enzymatic reaction in central carbon metabolism as well as for ATP buffering. All enzymes are implemented with fully reversible kinetic equations, with the reverse V_{max} calculated using a Haldane relation. The individual glycogen phosphorylase isozymes *A* and *B* are accounted for, which allows for inclusion of independent isozyme dependencies on metabolites, such as AMP. The phosphofructokinase (PFK) reaction includes the AMP activation and ATP inhibition observed experimentally. A Cleland Bi-Bi reaction is used for the creatine kinase ATP buffering kinetics. Creatine kinase can be inhibited by ATP, ADP, and phosphocreatine, consistent with experimental information. The final model consists of 14 reactions and 21 species. The glycolysis model ultimately takes glycogen and glucose and produces lactate. However, part of the pyruvate produced during glycolysis is transformed into acetyl coenzyme A and sent into the mitochondrial TCA cycle.

A detailed mitochondrial model (Fig. 3.5) was constructed, including oxidative phosphorylation and matrix processes. The primary input to the model is acetyl coenzyme-A (AcCoA), which is a shared point of convergence for the oxidation of glucose as well as fatty acids. The TCA cycle completes the oxidation of AcCoA to CO_2 and produces NADH and $FADH_2$, providing the driving force for oxidative phosphorylation. The respiratory chain oxidizes NADH and $FADH_2$. Pumping protons across the mitochondrial inner membrane establishes an electrochemical gradient, or proton motive force ($\Delta\mu_H$), composed of an electrical gradient ($\Delta\Psi_m$) and a proton gradient (ΔpH). This proton motive force drives the phosphorylation of matrix ADP to ATP by the F_1F_0-ATPase (ATP synthase). The large $\Delta\Psi_m$ of the inner membrane (-150 to -200 mV; matrix negative with respect to the cytoplasm) determines the electrochemical transport of ions, including the co-transport of ATP and ADP by the adenine

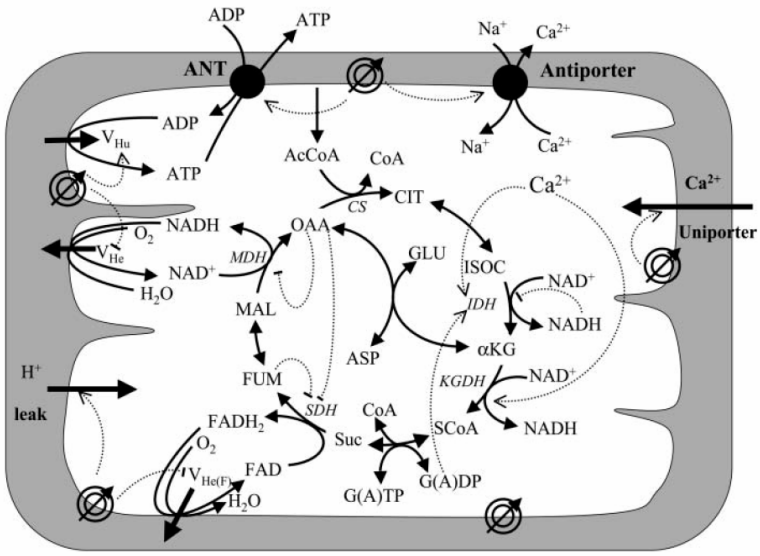

Figure 3.5; Mitochondrial model adapted from Cortassa[26]. The concentric circles with an arrow across located at the inner mitochondrial membrane represent the inner membrane potential ($\Delta\Psi_m$). Dotted arrows indicate regulatory interactions either positive (arrowhead) or negative (–).

nucleotide translocation, Ca^{2+} influx via the Ca^{2+} uniporter, and Ca^{2+} efflux via the Na^+/Ca^{2+} antiporter. The model also accounts for the explicit dependence of the TCA cycle enzymes isocitrate dehydrogenase and α-ketoglutarate dehydrogenase on Ca^{2+}. In this way, the rate of Ca^{2+} uptake by mitochondria is involved in membrane polarization through the TCA cycle and oxidative phosphorylation. Calcium dynamics are an important part of this model, because the primary action of OP compounds is to cause a prolonged increase in cytosolic Ca^{2+} concentration. The final model consists of 27 chemical species and 22 detailed reaction fluxes governed by specie inhibition/activation.[79]

Signaling and Calcium Dynamics

A summary of the pathways included in the model is shown in Figure 3.6, which includes:[80]

- Phospholipase C activation and intracellular calcium release.
- Protein kinase C activation and MAPK cascade activation.
- Adenylyl cyclase activation and cAMP production.
- Phospholipase A_2 activation and arachidonic acid production.
- The inclusion of kinase and phosphatase activation and inactivation for positive and negative feedback loops.

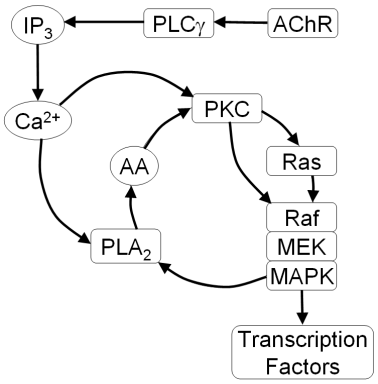

Figure 3.6; a summary of the complex pathway, showing the major signaling routes.

The model was modified to account for IP_3 regulated endoplasmic calcium release and extracellular calcium influx.[81] Pathways within the signaling model are linked through second messengers such as arachidonic acid that are produced in one pathway and used as an input to another pathway. An alternative way that pathways are linked is through enzyme activation. Enzymes whose activation was regulated by one pathway were coupled to substrates belonging to other pathways. The input to the signaling model is the extracellular acetylcholine concentration, which activates muscarinic receptors on the cell surface, ultimately leading to the release of calcium and activation of protein kinases. The complete pathway used in the model is shown in Fig. 3.7.

Experimental

Materials

All materials were used without modification unless otherwise noted. Glassy carbon rods (1 mm diameter) were obtained from Structure Probe, Inc. (West Chester, PA). All microphysiometer consumables were purchased from Molecular Devices (Sunnyvale, CA). PC12

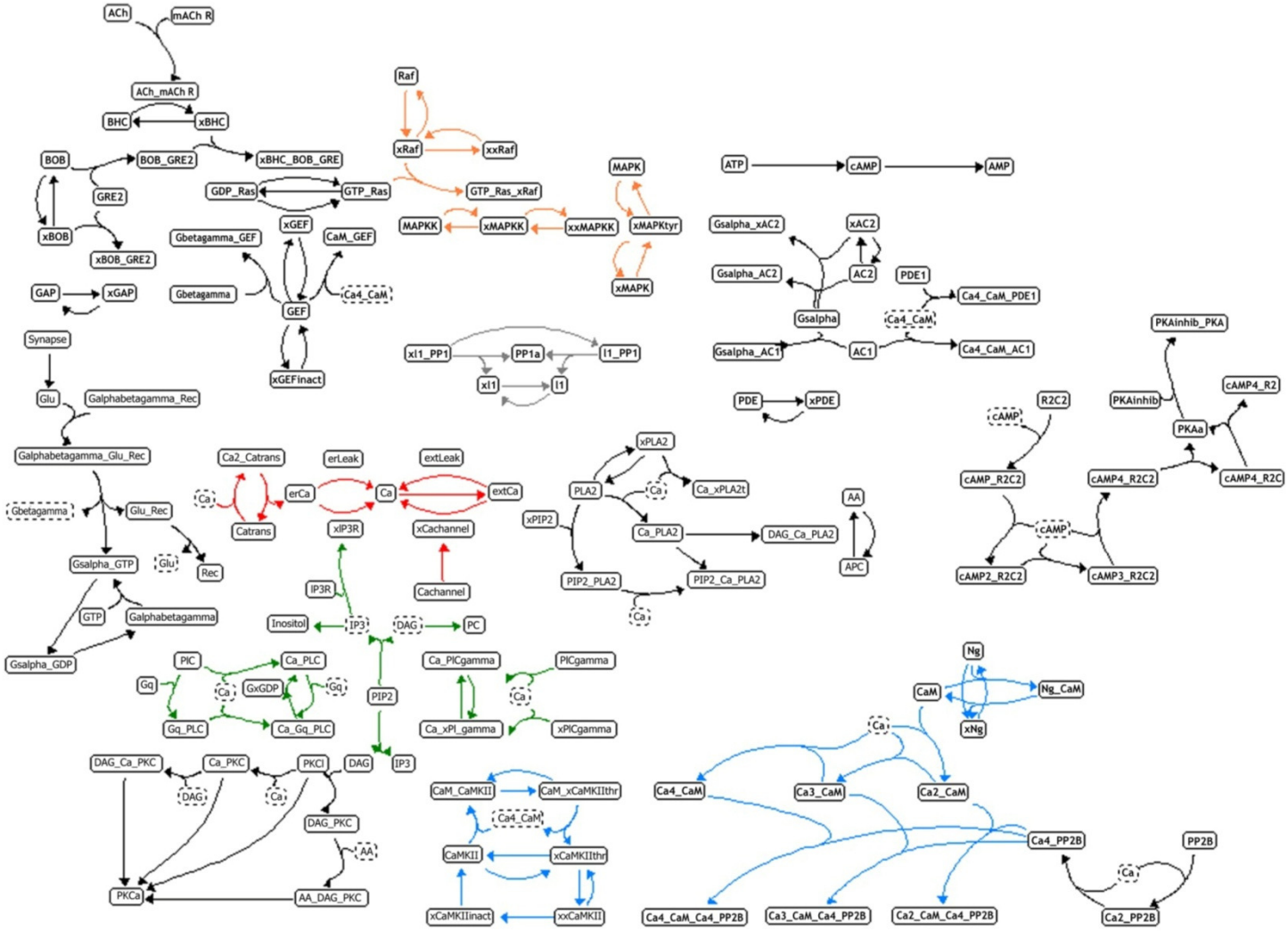

Fig. 3.7; Signaling cascade including initial activation via acetylcholine, MAPK cascade, formation of cAMP, and activation of PLC and PKA [adapted from Bhalla[80]].

cells, Ham's F12K media, fetal bovine serum (FBS) and horse serum were ordered from the American Type Culture Collection (ATCC). Dulbecco's phosphate buffered saline (DPBS), HEPES, DMSO, and dopamine from Fisher. Collagen (type IV, from human placenta), 1,6-hexanedioldiacrylate, parathion, 1,6-hexanedioldiacrylate, potassium tetrakis(4-chlorophenyl) borate, Ebecryl 600 (bisphenol A epoxydiacrylate), Uvecryl P36 (copolymerizable benzophenone photoinitiator) and 0.5 mm Ag wire were ordered from Sigma-Aldrich. Calcium bis[4-(1',1',3',3'-tetramethylbutyl)phenyl] phosphate (CaTBPP) was obtained from Dojindo Molecular Technologies, Inc. ASTM Type I (18 $M\Omega \cdot cm^{-1}$) analytical grade deionized water (DW) was obtained with a Solution 2000 Water Purification System from Solution Consultants.

Electrochemical measurements for calibration and sensitivity testing, the chloridizing of the Ca^{2+} sensor, as well as Ca^{2+} detection during MAMP experiments, was accomplished using a model 660A potentiostat (CH Instruments, Austin, TX), in the included Faraday cage with picoamp current booster, and using a standard 3-electrode electrochemical setup. Experiments utilized MAMP sensor heads as WE, commercial macro Ag/AgCl, 3 M KCl RE (CH Instruments model CHI111), and Pt mesh or coiled Pt wire CEs fabricated in our lab. Ferrocenylmethyltrimethylammonium hexafluorophosphate (FcTMA) was prepared according to the method of Mirkin and co-workers.[82]

Cell Culture and Preparation

A frozen PC12 cell culture was obtained from ATCC. This culture was thawed, seeded in growth medium (Ham's F12K medium with 2 mM L-glutamine adjusted to contain 1.5 g/L sodium bicarbonate, 82.5%; horse serum, 15%; fetal bovine serum, 2.5%, hereafter referred to as growth media) and placed in an incubator for propagation (5% CO_2, 37 ºC). In order to provide a cell repository, a number of cells (equivalent to the original culture) were separated after the initial propagation, re-frozen, and stored in vapor-phase liquid nitrogen. In the event of active

cell line contamination or failure to thrive, this repository permits restoration with a minimal loss of time. PC12 cells were grown on sterile dishes and/or cell culture vials coated with collagen type-IV (mouse or human) to promote adhesion. Cells were subcultured every 5-9 days, depending upon when confluency was achieved. Cells cultured in 90 mm dishes had growth media changed daily, while those cultured in larger vials necessitated less frequent media change.

To prepare cells for use in the MAMP, Cytosensor® capsule cups, contained in a 12 well plate, were coated with type-IV collagen (to promote PC12 adhesion) from a solution in 0.5% acetic acid to achieve a coverage of 5×10^{-6} g cm^{-2}. The 12 well plate was then loosely covered, allowing for ventilation during evaporation, then placed into an oven at 35 °C for 12 – 24 hours, or until dry. The cups were then washed 3x with Dulbecco's phosphate buffered saline (DPBS), which was prepared with sterile water, and once with 70% EtOH, and stored at 5 °C until use.

MAMP experiments were scheduled to coincide with cell culture cycles to retain maximal propagation rates from the cells. During subculturing, excess PC12 cells removed during transfer were utilized to seed the type-IV collagen coated Cytosensor® capsule cups. The previously coated capsule cups were removed from refrigeration and allowed to come to room temperature, then rinsed 3x with growth media. The cells were transferred under sterile conditions in a ventilated hood, then given fresh growth media and returned to the incubator overnight prior to use in the MAMP the following day. This allows the cells at least 12 hours to recover from transfer and to attach to the membrane in the capsule cup. Shortly prior to insertion in the MAMP, the growth media is removed manually via aspiration with a transfer pipette and replaced with running media. The cell cups are then transferred to the MAMP and the cells are allowed to re-equilibrate to 37 °C prior to the initiation of measurements.

MAMP Procedure

The '*running medium*' contains glucose at an 11 mM concentration and, due to atmospheric pressure, oxygen at an equilibrium concentration of 0.24 mM. The

microphysiometer pumps medium into the cell chamber for specified amount of time (t_{flow}), and then stops the flow for a certain amount of time (t_{stop}) in order to measure the production/depletion of metabolites. For the purposes of our experiments, t_{flow} was 2.5 minutes, and t_{stop} was 30 seconds. Due to the limited solubility of OP compounds in aqueous solutions, the *running medium* was supplemented with 2.5% DMSO.

Initial experiments followed levels of oxygen, lactate, glucose, and cellular H^+ production, while later experiments replaced the oxygen sensor with a 1 mm carbon electrode for dopamine detection. The carbon electrodes were coated with Nafion® to minimize signal distortion caused by ascorbic acid (AA). Additionally, a potentiometric Ca^{2+} sensor was incorporated into the existing microphysiometer framework, increasing the number of potential biomarkers to six (4 metabolic and 2 signaling). A flow-cell sensor with a similar geometry was identified in the literature,[83] and the existing sensor head was modified accordingly. During experimentation, however, it was determined that the crosstalk created by use of three different instruments (LAPS potentiostat, MAMP multipotentiostat, and a separate potentiostat for Ca^{2+} determination) in the same microfluidic chamber was too prohibitive for data collection. For this reason, in MAMP channels where Ca^{2+} measurements were performed no amperometric sensors were included. LAPS measurements for extracellular acidification, however, were performed in conjunction with Ca^{2+} measurements, and only Ca^{2+} data from cells with equivalent rates of extracellular acidification were utilized for analysis. All potentials reported for MAMP studies are *vs*. the MAMP internal Ag/AgCl, 2 M KCl RE.

a. Dopamine Measurements

The detection of dopamine using oxidative amperometry is well-established in the neuroscience community. The preferred electrode material for dopamine detection on the macro scale is a GCE. Calibration of the GCE was performed using a standard solution of 10^{-4} M dopamine in HEPES cell buffer (130 mM NaCl, 10 mM HEPES, 1.5 mM $CaCl_2$, 0.5mM

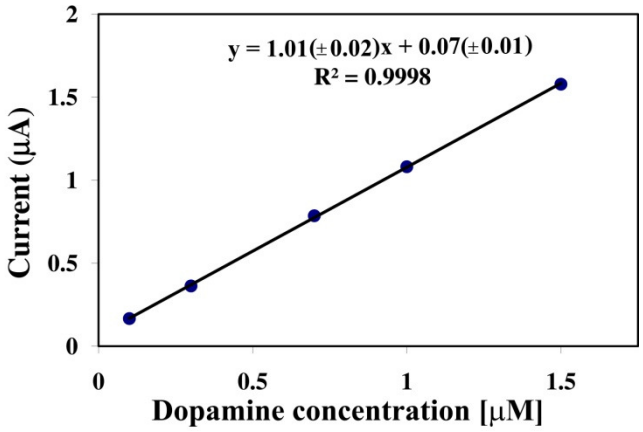

Figure 3.8; A amperometric calibration plot for the GCE incorporated in the MAMP sensor head, showing current as a function of Log (dopamine concentration).

$MgSO_4$, 1.3 mM KH_2PO_4, 34 mM Dextrose, pH adjusted to 7.4), hereafter referred to only as cell buffer. The cell buffer was used to spike a 10.00 ml sample to produce the calibration curve. The addition of 1, 10, 50, 100, 500, and 1000 µL (e.g., 1, 9, 40, 50, 400, and 500 µL successive additions) made concentrations of 10^{-8}, 10^{-7}, $5x10^{-7}$, 10^{-6}, $5x10^{-6}$, and 10^{-5} M dopamine. Measurements were taken via Square-Wave Voltammetry (SWV) with scans from − 0.3 V to + 0.5 V (*vs.* Ag/AgCl, 3 M KCl RE) taken in 4 mV increments (40 mV amplitude and 50 Hz frequency). Figure 3.8 shows a calibration curve of current (pA) versus Log (Dopamine concentration, M) for the range tested.

b. Calcium Measurements

The detection of Ca^{2+} was performed via potentiometry with an ion-selective electrode, based on a 0.5 mm Ag disc integrated into the MAMP sensor head assembly. The sensor was adapted from previous work published by Dimitrakopoulos.[83] Sensor fabrication began by chloridizing the Ag disc in a 100 mM KCl solution by applying a potential of + 0.5 V, *vs.* Ag/AgCl, 3 M KCl RE for 15 – 20 minutes. The freshly chloridized electrode was then washed with copious amounts of DI water. The chloridized electrode surface was then covered with a photo-polymerizable mixture consisting of Ebecryl 600 (44.8%), Uvecryl P36 (5.3%),

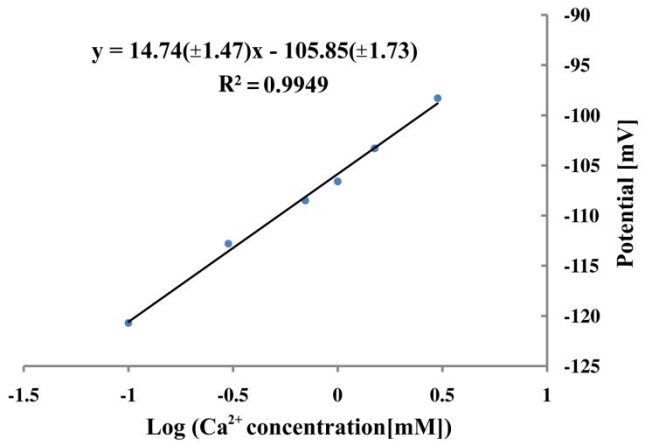

Figure 3.9; A plot showing the potentiometric response of the Ca^{2+} MAMP sensor. The sensor has a decidedly sub-Nernstian response of ~ 15 mV per decade of Ca^{2+} concentration.

1,6-hexanedioldiacrylate (22.3%), potassium tetrakis(4-chlorophenyl)borate (0.6%), dioctylphenyl phosphonate (20.9%) and the ionophore CaTBPP (6.1%) using a fine brush. The entire sensor head assembly was then irradiated with an ultraviolet lamp (140 W quartz halogen) under an argon blanket to preserve an inert atmosphere during polymerization, and the mixture was cured until hard and transparent (~ 5 minutes). The resulting film was then washed with ethanol and DI water, and pre-conditioned in a 100 mM $CaCl_2$ solution (pH 5.0) overnight prior to any measurements.

Figure 3.9 shows a calibration curve for the Ca^{2+} sensor over the range from 0.1 to 3 mM Ca^{2+}. While the electrode response is linear (R^2 = 0.9874) the response is decidedly sub-Nernstian, yielding 17.2 mV of sensor response per decade (over 1.3 decades) instead of the theoretical 29.6 mV for a bivalent cation. It is unclear why this is the case, as the original sensor was reported to have a hyper-Nernstian response of 32.3 mV/decade of concentration.[83] Anecdotally, the sensors were cured with a quartz-halogen UV source which generated excess amounts of heat, enough in fact to discolor the epoxy used to seal them into the sensor head, which could have damaged the film during polymerization. Additionally, the sensors were only

utilized for one round of experiments, so variations in sensor response from batch to batch could not be observed.

Results and Discussion

Experimental Data

In order to study the dynamic aspects of cellular metabolism in real time, as required for metabolomic studies, a technique should be able to track multiple key biomarkers in real time as a function of metabolic agent exposure to live cells. The results of one such set of experiments for the exposure of PC12 cells to the OP agent parathion is shown in Fig. 3.10. The experiment followed the cellular production of H^+, lactate and dopamine, and for the uptake of glucose and Ca^{2+} as a function of time for a variety of concentrations of parathion ranging from 1 µM to

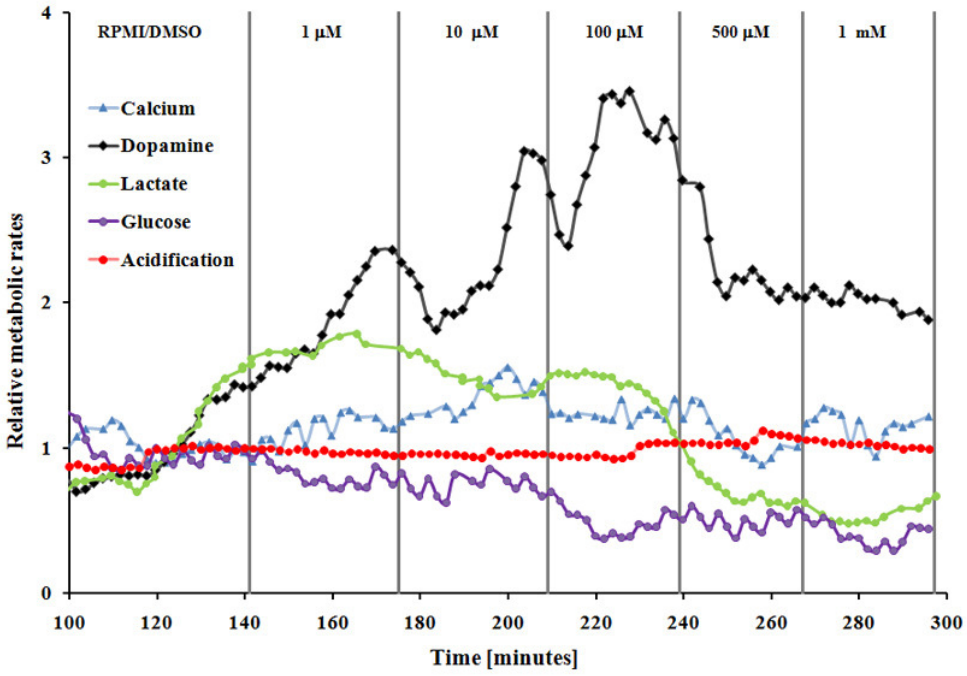

Figure 3.10; Relative changes in metabolic functions as a result of the exposure of PC12 cells to the OP toxin parathion. The results for Ca^{2+} (blue triangles) and glucose (purple circles) uptake, as well as expression of dopamine (black diamonds), lactate (green circles) and H^+ (red circles) were followed during exposure of the cells to levels of parathion ranging from 1 µM to 1 mM in a mixture of MAMP running media containing 2.5% DMSO. The levels were normalized with respect to the levels observed prior to exposure to parathion, and data points were smoothed via adjacent averaging (n = 3) to facilitate the observation of any trends as a function of OP exposure.

1 mM. The figure depicts the changes in metabolic activities, rather than the direct quantitative activity, which has been normalized with respect to the initial levels prior to exposure, in order to evaluate the effect of the multiple cellular pathways to the different levels of toxin exposure. The data points have also been smoothed, via adjacent averaging (n = 3) to better represent the trends of the changes in metabolic activity as a function of increasing parathion concentration. The use of such a plot is to elucidate possible ties between different pathways that might not be obvious looking at the individual data sets. For example, while the data for H^+ production appears nearly flat throughout the experiment, three jumps are observable. The first, at ~ 190 minutes, coincides with the beginning of a decrease in glucose uptake. The next two, at around 230 and 260 minutes respectively, coincide with the initiations of a decrease in lactate metabolism. While the cause of

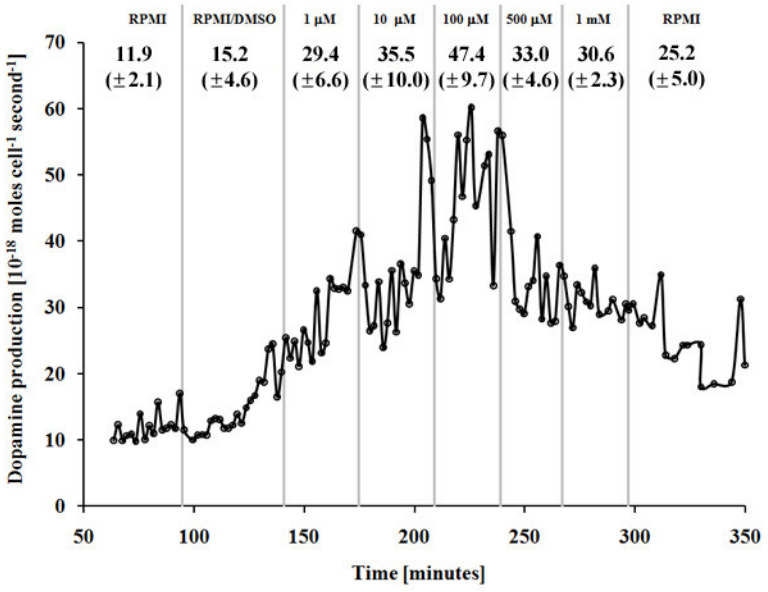

Figure 3.11; changes in dopamine release from PC12 cells in response to exposure to the OP toxin parathion. Numbers given are production in attomoles (10^{-18} moles) per cell per second, with standard deviations. Parathion concentrations, listed on the graph, were 1 µM, 10 µM, 0.1 mM, 0.5 mM, and 1 mM. Data was F-tested and t-tested, and the differences in the mean and variance for all parathion exposures were found to be significant at the 95% confidence level with respect to both the initial RPMI and DMSO media as controls data (see Appendix B).

these events may not be readily discernable, or even definitively linked, they can suggest possibilities for further investigation or for inclusion in future *in-silico* analyses.

While it is common to look at relative changes in metabolic activity for toxicity studies, the field of metabolomics focuses on quantitative, more than qualitative, analyses of metabolites. The same dopamine data, converted to production per cell per second, is presented in Fig. 3.11. The data shows that rather than a continual level of dopamine production at any given OP exposure, dopamine is actually released in bursts of variable intensity. During the course of the experiment, average dopamine production ranged from $10 - 60 \times 10^{-18}$ moles cell^{-1} second^{-1}. The dopamine production is initially stimulated by addition of DMSO to the media, and increasingly stimulated by addition of 1 µM and 10 µM parathion concentrations. The average dopamine production remains constant through the 100 µM exposure, albeit with increase burst intensity, then both intensity and average output begins to decline upon exposure to 500 µM and 1 mM

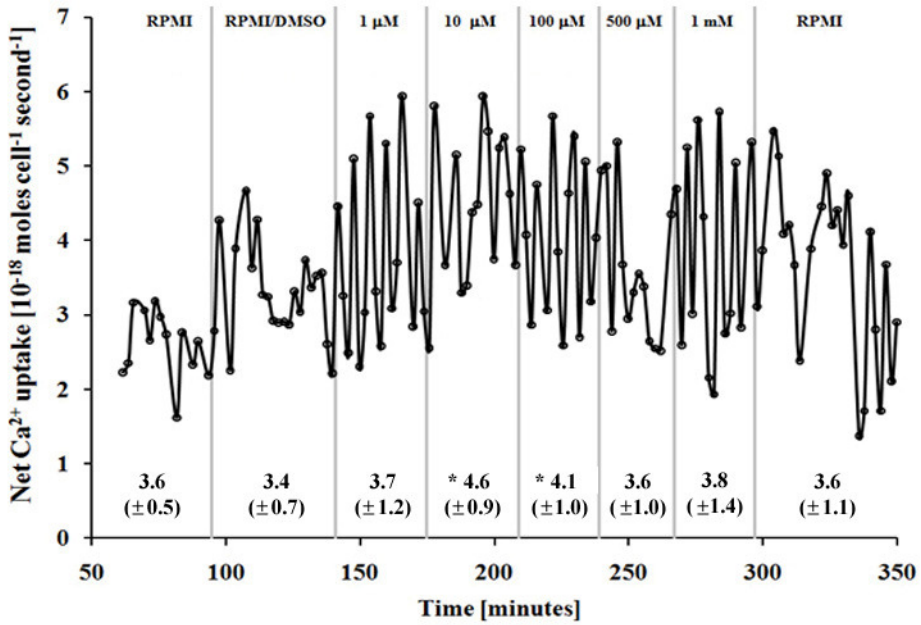

Figure 3.12; fluctuations in net Ca^{2+} uptake by PC12 cells in response to exposure to the OP toxin parathion. Numbers given are uptake in attomoles (10^{-18} moles) per cell per second, with standard deviations. Parathion concentrations, listed on the graph, were 1 µM, 10 µM, 0.1 mM, 0.5 mM, and 1 mM. Data was F-tested and t-tested, and the differences in the mean and variance for only the 10 and 100 µm parathion exposures were found to be significant at the 95% confidence level with respect to the DMSO media data (see Appendix B).

parathion. The removal of all parathion decreases the intensity of the fluctuations in dopamine production, and allows a partial recovery to the basal metabolic production rate.

The quantitative net uptake of Ca^{2+} by the PC12 cells during the course of the experiment is shown in Fig. 3.12. Variations in Ca^{2+} uptake were seen to range from ~ 1.5 to 6×10^{-18} moles $cell^{-1}$ $second^{-1}$. Ca^{2+} uptake and release is known to occur in an oscillatory form in neurons, and uptake can be seen to modulate significantly after exposure to parathion. A slight increase in net Ca^{2+} can be observed from the 1 µM to the 10 µM parathion exposure, and is maintained throughout the 100 µm exposure, but subsequent increases in parathion concentration do not seem to increase the maximum detected levels beyond that. Statistically, according to F-test and t-test analysis, the 10 µM and 100 µM exposures are the only two significantly different at the 95% confidence level from the DMSO control data (see Appendix B). This is probably due

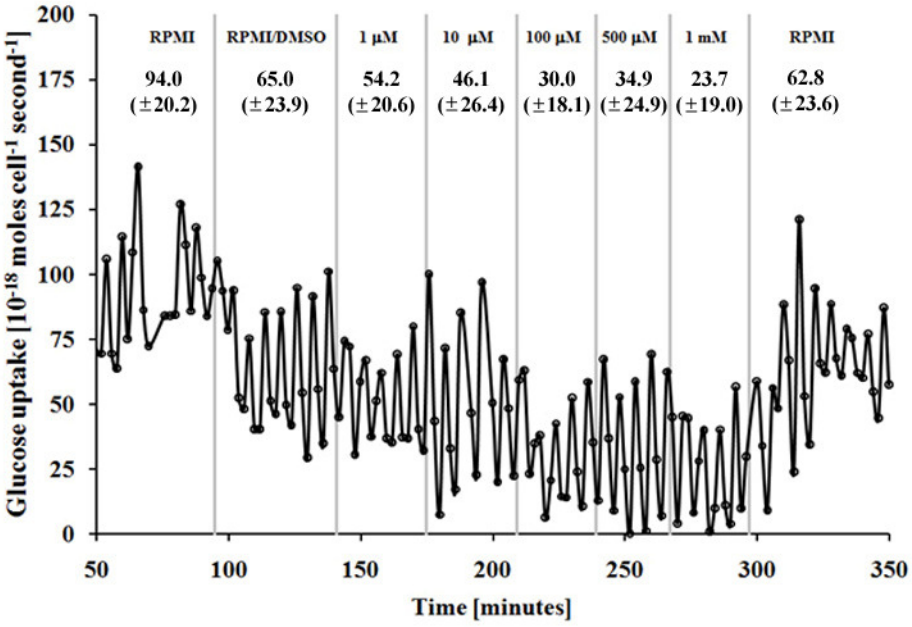

Figure 3.13; changes in glucose uptake by PC12 cells in response to exposure to the OP toxin parathion. Numbers given are glucose uptake in attomoles (10^{-18} moles) per cell per second, with standard deviations. Parathion concentrations, listed on the graph, were 1 µM, 10 µM, 0.1 mM, 0.5 mM, and 1 mM. Data was F-tested and t-tested, and the differences in the mean and variance for all parathion exposures were found to be significant at the 95% confidence level with respect to both the initial RPMI and DMSO media as controls (see Appendix B).

to the low signal to noise ratio caused by attempting to measure small fluctuations in Ca^{2+} media concentration against a high bulk background concentration.

Like Ca^{2+} uptake, the glucose uptake observed by the PC12 cells showed an oscillatory trend (Fig. 3.13). Unlike the previous measurements, however, the glucose uptake was observed to reduce below the level of detection, shown in Fig. 3.13, at a several points during the 500 µM and 1 mM OP exposures. The consequences of this would be a virtual shutdown of the entire glycolytic pathway. Prior to parathion exposure, the average glucose uptake is observed to be $75 - 80 \times 10^{-18}$ moles $cell^{-1}second^{-1}$ for RPMI only, decreasing to ~ 60×10^{-18} moles $cell^{-1}$ $second^{-1}$ after DMSO is mixed with the media. Average glucose uptake after parathion exposure tends to decrease in proportion to increasing parathion concentration.

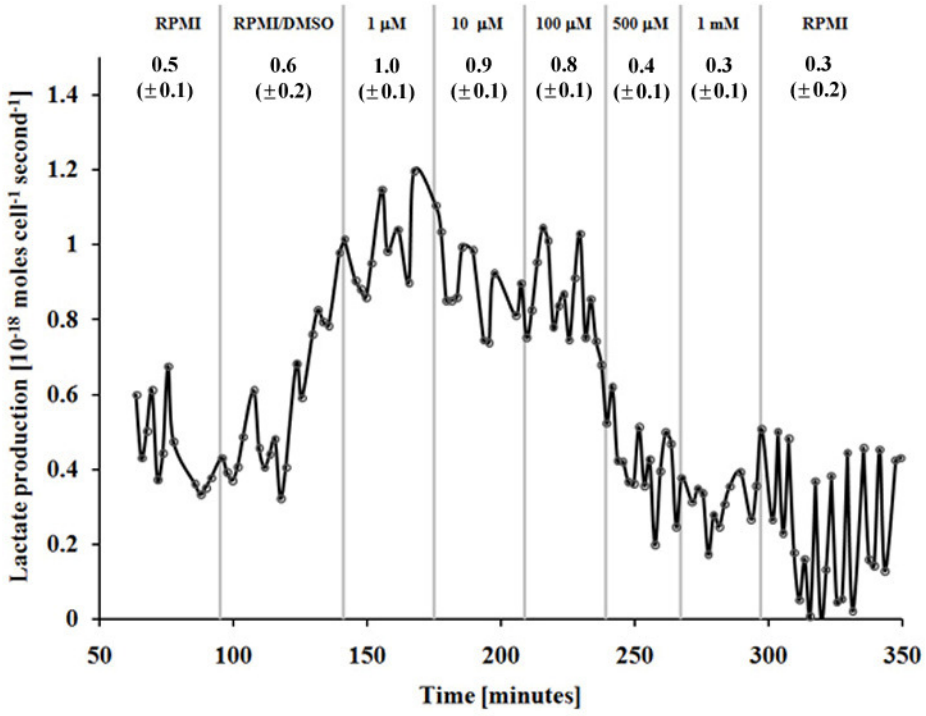

Figure 3.14; changes in lactate production by PC12 cells in response to exposure to the OP toxin parathion. Numbers given are production in attomoles (10^{-18} moles) per cell per second, with standard deviations. Parathion concentrations, listed on the graph, were 1 µM, 10 µM, 0.1 mM, 0.5 mM, and 1 mM. Data was F-tested and t-tested, and the differences in the mean and variance for all parathion exposures were found to be significant at the 95% confidence level with respect to both the initial RPMI and DMSO media as controls data (see Appendix B).

The changes in lactate production of PC12 cells measured during the experiment are presented in Fig. 3.14. An initial increase in lactate production, indicative of a shift toward anaerobic metabolism, is observed upon exposure to DMSO. Lactate production continues to increase throughout the 1 μM parathion exposure, where production averages ~ 1×10^{-18} mole $cell^{-1}$ $second^{-1}$. After this point production decreases gradually for the 10 μM and 100 μM exposures prior to dropping off steeply after being exposed to 500 μM parathion. The same average production (~ 0.3×10^{-18} mole $cell^{-1}$ $second^{-1}$) is then observed until the parathion is removed. After return to normal RPMI media, the average production drops further (to ~ 0.2×10^{-18} mole $cell^{-1}$ $second^{-1}$) at which time an oscillatory production pattern initiates.

Validation of Signaling and Metabolic Pathways

a. Validation of Glycolysis Model

Modeling of metabolic enzyme kinetics requires the consideration of enzymatic kinetic mechanisms such as Ordered Bi-Bi, Random Bi-Bi, Ping Pong Bi-Bi and Multi-site Ping Pong kinetics. Enzyme kinetics are known to be highly regulated by competitive and non-competitive inhibition/activation. In addition to metabolic enzyme kinetics, metabolite membrane transport mechanisms need to be accounted for because the predictions will ultimately be compared to microphysiometer experimental data. During validation, model parameter values used in the glycolysis model were based on previously published experimental values,[78] with equations and coefficients taken from that work. Since all model equations are fully reversible, a thermodynamic analysis of the pathway can be performed. The overall equilibrium expression for glycolysis is:

$$K_{eq} = C_{Lac}^2 \left(\frac{C_{ATP}}{C_{ADP} C_{PO_3}} \right)^3 \tag{3.1}$$

Running the dynamic model to steady state yields an overall equilibrium coefficient of 1.559×10^{19} M^{-1}. This translates to a free energy drop of -27.32 kcal mol^{-1}, in excellent agreement with the published value.[84] Each individual reaction was tested for equilibrium accuracy and compared to the published values[84] with excellent agreement. The model dependence on cellular ATP usage was tested in order to determine the redox and phosphorylation potential within the cytosol. Figure 3.14 is a plot of the steady-state dependence of the model under increasing ATP usage loads. Initially, the redox potential increases with increased carbon flux through the

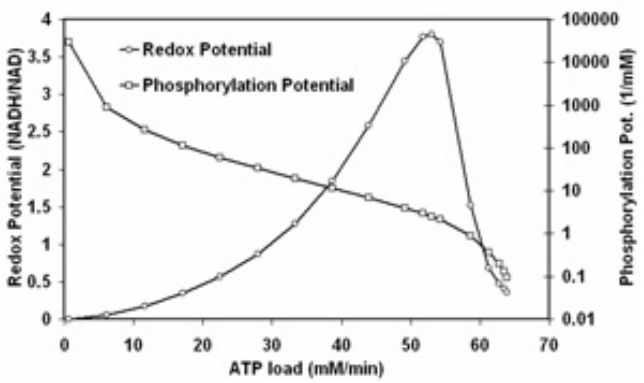

Figure 3.15; Plot of the cytosolic redox and phosphorylation potential variation with ATP usage.

glycolysis cycle. The redox potential attains a maximum at an ATP usage of approximately 55 mM/min. Past this point, there is a sharp drop in the cytosolic ATP concentration due to a breakdown in the ATP buffering. This causes an increase in ADP and free phosphate, indicated by a rapid decrease in the cytosolic phosphorylation state of the cell (Fig. 3.15). Total carbon flux through the system increases linearly with ATP usage throughout the entire range (Fig. 3.16), indicating that the total carbon flux is relatively insensitive to the redox and phosphorylation potential within the cell, and primarily determined by ATP usage. Enzymes responsible for NAD/NADH turnover (LDH and GAPDH) do not contribute heavily to the carbon flux control.[85] This explains the insensitivity of the total carbon flux to the cytosolic redox potential.

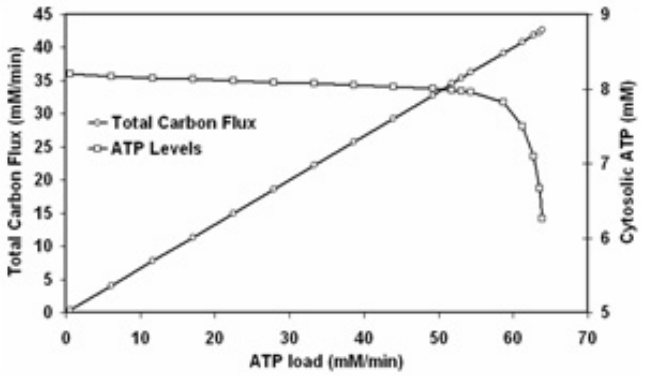

Figure 3.16; Plot of the total carbon flux and cytosolic ATP level variation with ATP usage.

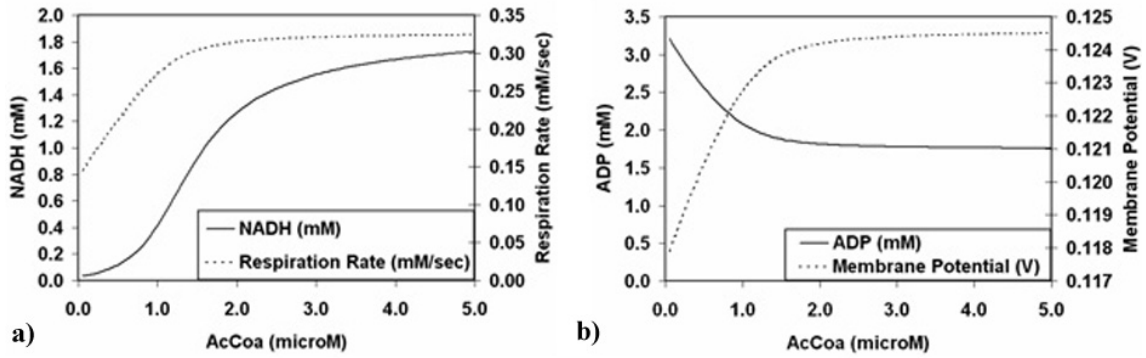

Figure 3.17; Dependence of the NADH (a) and ADP (b) components of the metabolic model to nutrient availability.

b. Validation of Mitochondrial Model

Steady state model response to substrate availability was examined by varying the AcCoA concentration. Increasing the AcCoA concentration to a maximum of 5 mM causes a twofold increase in the respiration rate (V_{O2}); beyond this point the V_{O2} saturates (Fig. 3.17a). The increase in V_{O2} is driven by the generation of NADH in the range of 0.01–1.6 mM (Fig. 3.17a). The increasing respiration rate also causes an increase in the usage of ADP, decreasing the mitochondrial concentration from 3.2 to 1.75 mM (Fig. 3.17b). The V_{O2} at low AcCoA concentration is driven primarily by consumption of glutamate (see Fig. 3.5). Stimulation of electron transport is associated with a 6 mV increase (Fig. 3.18) in membrane potential ($\Delta\Psi_m$).

The linear relationship between V_{O2} and $\Delta\Psi_m$ (Fig. 3.18) is in agreement with experimental results.[79]

Mitochondrial function is altered by Ca^{2+} in two opposing ways. First, the influx of Ca^{2+} causes a decrease in the $\Delta\Psi_m$, decreasing the proton motive force. Second, the presence of Ca^{2+} in the mitochondria stimulates the production of NADH, increasing the proton motive force. The

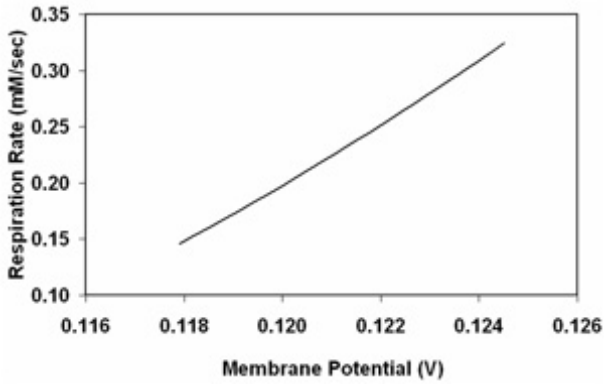

Figure 3.18; Dependence of the mitochondrial respiration rate on membrane potential.

steady state response of the model to changes in cytosolic Ca^{2+} concentration in the physiological range (0.01 to 2.0 μM) is shown in Figure 3.18. Mitochondrial Ca^{2+} exponentially increases once the cytosolic Ca^{2+} concentration increases to above 0.50 μM. The mitochondrial Ca^{2+} concentration continues to increase to 30 μM without saturation (Fig. 3.19a). The threshold value for cytosolic Ca^{2+} is set by the relative rates of the Ca^{2+} uniporter and the Na^+/Ca^{2+} antiporter, which are coupled indirectly through $\Delta\Psi_m$. The resultant mitochondrial Ca^{2+} profile compares well with experimental results.[79]

An increase in the V_{O2} with increasing mitochondrial Ca^{2+} is evident in Figure 3.19a. Along with the increasing V_{O2}, the steady-state flux through the Ca^{2+}- sensitive dehydrogenases also increases with increased mitochondrial Ca^{2+} (isocitrate dehydrogenase (IDH) shown in Fig. 3.19a). The dependence of $\Delta\Psi_m$ on mitochondrial Ca^{2+} illustrates the opposing action of Ca^{2+} transport. Below a cytosolic Ca^{2+} concentration of 0.40 μM, the membrane potential increases to

a maximum value of 125 mV. An increase in the cytosolic Ca^{2+} concentration beyond this point causes a large influx of Ca^{2+}, decreasing the $\Delta\Psi_m$ by depolarizing the inner membrane.

At low cytosolic Ca^{2+} concentration, the increase in dehydrogenase activity increases the concentration of NADH within the mitochondria. The decrease in NADH at higher cytosolic Ca^{2+} concentration is caused by the saturation of the stimulatory effect on dehydrogenase activity

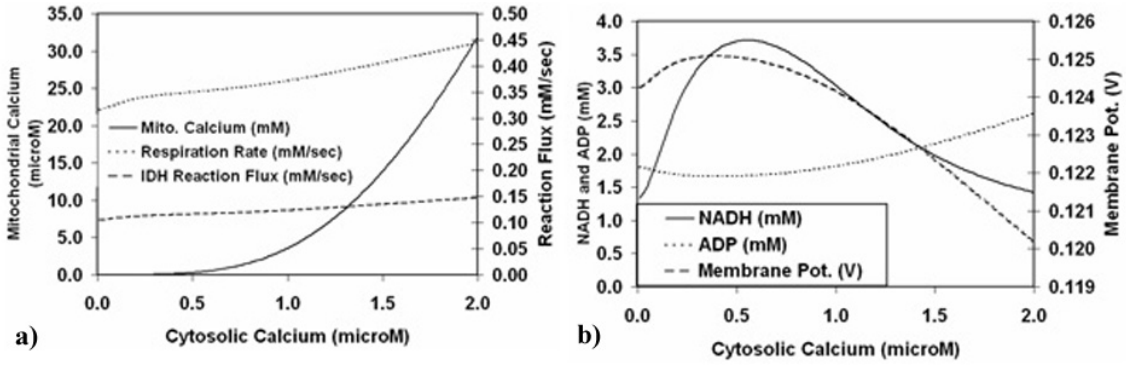

Figure 3.19; Dependence of the mitochondrial model on cytosolic Ca^{2+} concentrations.

concomitant with an increase in respiration rate (Fig. 3.19b). The dependence of ADP on cytosolic Ca^{2+} is the result of the interplay of the NADH and respiration. The dip in ADP concentration is driven by the increased availability of NADH, while the increase in ADP concentration results from a rapid decline in the NADH levels. The ADP increase does not directly track with the NADH decrease because ADP is consumed during respiration.

c. Intracellular Signaling and Calcium Dynamics Model Performance

In contrast to the metabolic pathways, signaling pathway mechanisms can be modeled primarily by mass-action kinetics. Initial species association/dissociation interactions are required to induce downstream protein phosphorylation/dephosphorylation through various protein kinase and phosphatase reactions. Metabolic and signaling pathways are linked via second messengers (i.e. calcium, cAMP), the availability of high-energy phosphate pools, and the redox state of the cell. General biochemical reactions included in this cellular signal transduction

network include ligand-protein interactions, protein-protein interactions, protein phosphorylation and dephosphorylation, enzymatic activity and trafficking of second messengers, such as calcium, cAMP, and IP_3. All kinetic coefficients used in the signaling and calcium dynamics model were taken from previously published experimental and theoretical studies.[80,81]

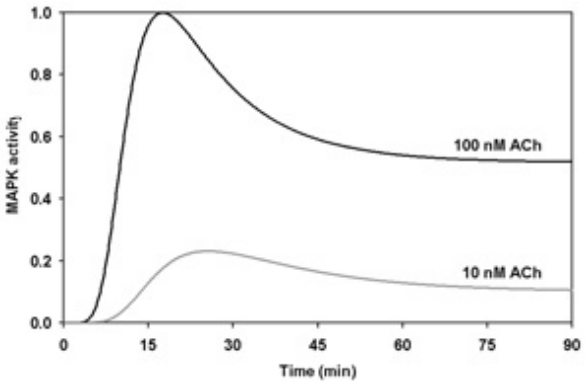

Figure 3.20; Plot of MAPK activity with variation in ACh concentration.

A set of example calculations were performed in order to demonstrate the signaling pathway. The cell is assumed to be in homeostasis at time zero, at which time the cell is exposed to acetylcholine. The acetylcholine buildup is assumed to be caused by the inhibition of the acetylcholinesterase by an OP compound. The activation of mitogen activated protein kinases (MAPKs), PLCγ, and intracellular Ca^{2+} was plotted in order to demonstrate the dose response behavior of the model. Figure 3.20 illustrates the dose-dependent activation of MAPK at the two concentrations of acetylcholine (10 and 100 nM). The sharp increase in MAPK activity is attributed to rapid extracellular influx of calcium into the cytoplasm and concomitant release of calcium from the endoplasmic pools. The relatively slower phosphatase action then reduces the overall activity, however, even at a small dose there is persistent activation of 10% MAPK. At a higher dose, the time scale for activation is much faster, with a peak activation of close to 100%, and approximately 50% remaining active with persistent acetylcholine stimulation.

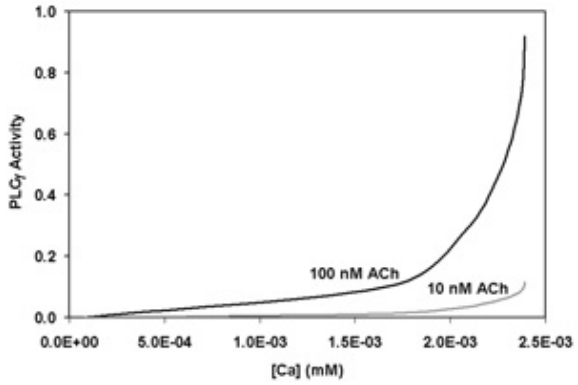

Figure 3.21; Plot of PLCγ activity against cytosolic calcium concentration with variation in ACh concentration.

Figure 3.21 is a plot of the dependence of PLCγ activity on cytosolic calcium. This plot indicates that there is a concentration range where the PLCγ activity increases linearly with calcium concentration. However, as the cytosolic calcium concentration increases to approximately 2 μM, the activity increases rapidly for the high dose curve and shows only modest increase with the low dose curve. The rapid increase in activity is due to a positive feedback loop between the secondary messenger IP_3 and calcium release, which is catalyzed by PLCγ.

d. Validating Dopamine Release Model

A model of dopamine release was constructed using the existing signaling pathway models, and was fitted to the data. The model accounts for the buildup of acetylcholine in the extracellular space due to the inhibition of the acetylcholinesterase (AChE) by parathion. The excess acetylcholine binds to the acetylcholine receptor (AChR) and activates the PLCγ–Ca^{2+} complex leading to the formation of IP_3. The excess IP_3 causes the release of Ca^{2+} from the endoplasmic reticulum causing an increase in the cytosolic calcium, ultimately catalyzing the release of dopamine (Fig. 3.22).

We used the existing virtual MAMP simulation environment to fully couple the pump/stop action of the MAMP and its sensors to the predictive, dynamic model of dopamine

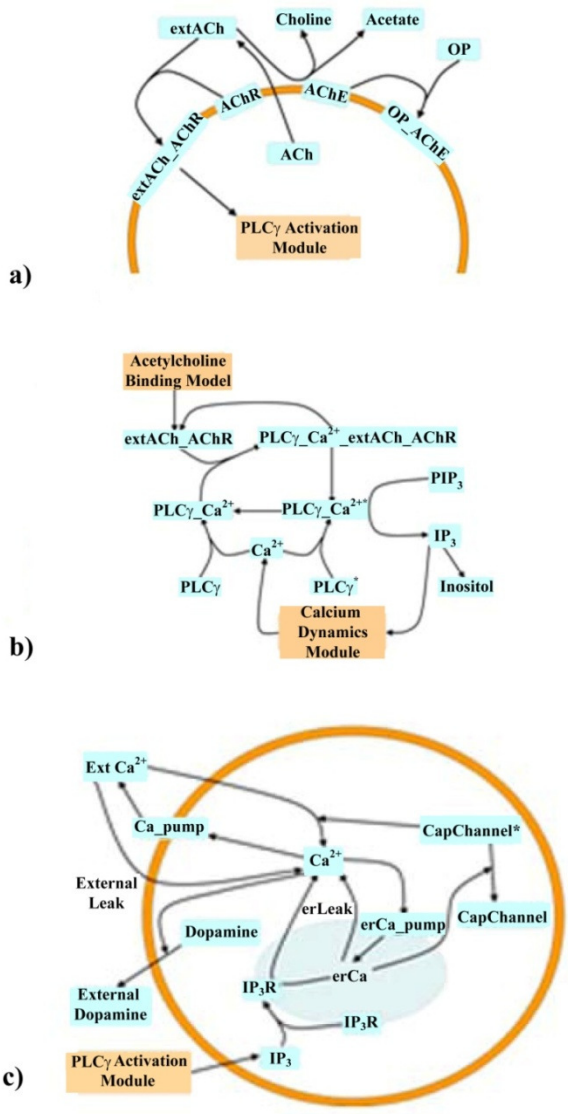

Figure 3.22; (a) OP compounds bind to AChE, causing an increase in acetylcholine (ACh). The excess ACh binds to the ACh receptor activating the PLCγ pathway. (b) The bound AChR complex triggers the formation of IP3 catalyzed by the PLCγ–Ca^{2+} complex. (c) IP3 triggers the release of Ca^{2+} from the endoplasmic reticulum, increasing the cytosolic calcium concentration, leading to the release of dopamine.

release. Simulations were performed using the coupled system with an MAMP pump time of 80 sec and a stop time of 40 sec. The parathion scheduling and cytosolic calcium response is given in Fig. 3.23. Cytosolic calcium rises rapidly with increasing parathion concentration (Fig. 3.24), due to the positive feedback loop formed between PLCγ and cytosolic Ca^{2+} (see Fig. 3.21). The

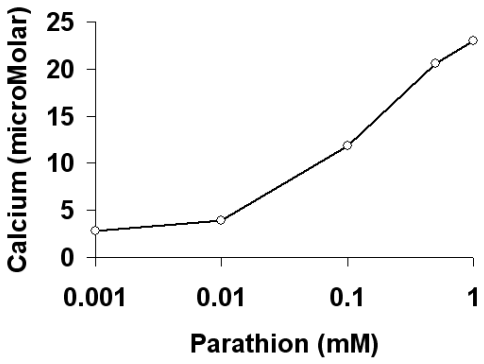

Figure 3.23; Correlation between cytosolic Ca^{2+} concentration and parathion exposure.

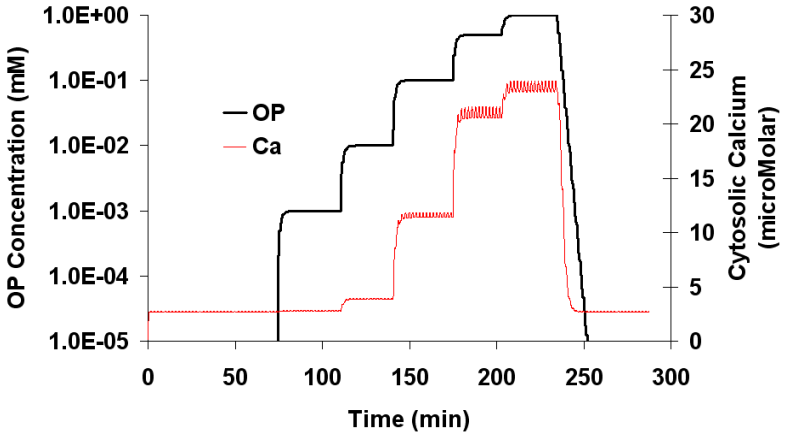

Figure 3.24; Parathion scheduling and the cytosolic calcium response.

response of the measured and simulated dopamine release by the system in response to the parathion scheduling shown in Figure 3.25. The model predicts the basal release of dopamine quite well. As with the data, the model predicts an increased dopamine release with increasing parathion concentration, up to a parathion concentration of 100 µM. At this point the model predicts a decrease in the overall release of dopamine. The model also captures the some of the "spiking" of dopamine release during transitions from one parathion concentration to another. The spikes are due to an abrupt increase in the release rate upon changing cytosolic Ca^{2+} concentrations, temporarily depleting the internal dopamine stores. Once the release rate gets

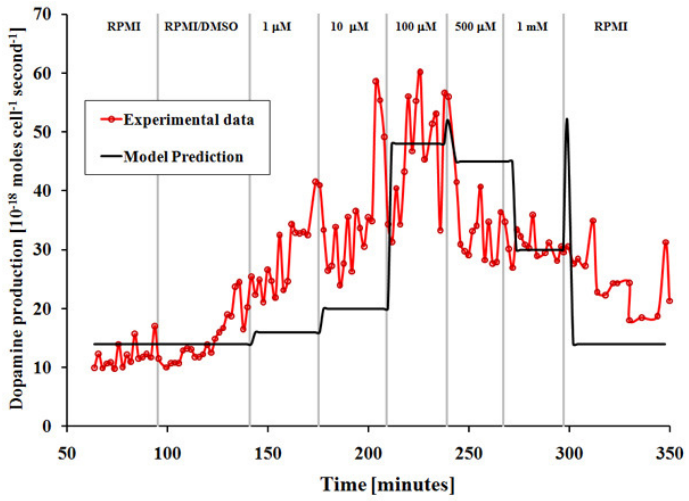

Figure 3.25; Comparison of the experimentally measured dopamine release to the release projected by the assembled model system.

high enough, the rate of production of dopamine is insufficient to replenish internal stores, and the amount of dopamine released decreases. Therefore, the model is capable of capturing the salient features of the dependence of dopamine release in PC12 cells upon external parathion concentration.

Conclusions

Two new sensors, for dopamine and Ca^{2+}, were incorporated into the MAMP platform and used for the first time. While the dopamine sensor successfully recorded production, due to less than favorable signal-to-noise ratios, the Ca^{2+} sensor was less reliable. With the exception of the previously mentioned Ca^{2+} data, the mean and variance for all data collected for each parathion exposure was found to be statistically significant at the 05% confidence level (full F-test and t-test results are in Appendix B).

The model neuronal cell line PC12 was utilized to examine the effects of exposure of the OP compound parathion at a variety of concentrations ranging from 1 µM to 1 mM. Quantitative as well as qualitative data were presented for the OP mediated changes in the metabolic cellular uptake of glucose and Ca^{2+}, as well as for changes in the production of lactate, and dopamine.

Qualitative data was also presented for the changes in extracellular acidification during parathion exposure.

A complete cell signaling pathway model was assembled *in-silico* by researchers at CFD Research corporation using data collected in our labs during prior MAMP experiments. This model was then applied to the data presented here in order to evaluate its ability to predict dopamine production by PC12 cells due to parathion exposure. The comparison of the dopamine model predictions to the experimental data collected shows agreement for the overall trends in dopamine production as a function of exposure to parathion.

Acknowledgements

All works reported in this chapter related to construction of pathway models, and analysis of data collected with respect to the validation of those models, were performed at the CFD Research Corporation (Huntsville, AL), by J. W. Jenkins, J. E. Hood, and S. Sundaram. PC12 cells for these experiments were cultured and maintained by Eugene Kozlov and Rachel Greene in the Prokop lab at the Department of Chemical Engineering, Vanderbilt University.

References

(1) Bongiovanni, M.; Casana, M. *Medicinal Chemistry* **2008**, *4*, 513-519.
(2) Camacho, P. M.; Lopez, N. A. *Clinical Chemistry and Laboratory Medicine* **2008**, *46*, 1345-1357.
(3) Cottingham, K. *Journal of Proteome Research*, ACS ASAP.
(4) Kimura, E.; Cooke, J. P. *Baiosaiensu to Indasutori* **2008**, *66*, 615-620.
(5) LaVallie, E. R.; Dorner, A. J.; Burczynski, M. E. *Current Opinion in Pharmacology* **2008**, *8*, 647-653.
(6) Eaton, D. L.; Daroff, R. B.; Autrup, H.; Bridges, J.; Buffler, P.; Costa, L. G.; Coyle, J.; McKhann, G.; Mobley, W. C.; Nadel, L.; Neubert, D.; Schulte-Hermann, R.; Spencer, P. S. *Critical Reviews in Toxicology* **2008**, *38*, 1-125.
(7) Mantovani, A.; Maranghi, F.; La Rocca, C.; Tiboni, G. M.; Clementi, M. *Reproductive Toxicology* **2008**, *26*, 1-7.
(8) Plant, N. *Toxicology* **2008**, *254*, 164-169.
(9) Watson, D. E.; Ryan, T. P.; Stevens, J. L. *Biotechnology: Pharmaceutical Aspects* **2006**, *4*, 255-270.
(10) Zhou, C.; Li, C. *Zhongguo Shuichan Kexue* **2007**, *14*, 864-871.
(11) Kim, Y. S.; Maruvada, P.; Milner, J. A. *Future Oncology* **2008**, *4*, 93-102.

(12) Kravcukova, P.; Marekova, M.; Ostro, A. *Chemicke Listy* **2008**, *102*, 15-20.
(13) Lewis, G. D.; Asnani, A.; Gerszten, R. E. *Journal of the American College of Cardiology* **2008**, *52*, 117-123.
(14) Lewis, G. D.; Gerszten, R. E. *Clinical Proteomics* **2008**, 279-293.
(15) Naraoka, H.; Suzumura, K.-i.; Takeuchi, K.-i.; Sasayama, T. *Rinsho Byori* **2008**, *56*, 335-342.
(16) Soga, T.; Ohashi, Y.; Tomita, M. *Saishin Igaku* **2007**, *62*, 2040-2047.
(17) Pelegrino, J. R.; Calore, E. E.; Saldiva, P. H. N.; Almeida, V. F.; Peres, N. M.; Vilela-de-Almeida, L. *Ecotoxicology and Environmental Safety* **2006**, *64*, 251-255.
(18) Stokes, L.; Stark, A.; Marshall, E.; Narang, A. *Occupational and Environmental Medicine* **1995**, *52*, 648-653.
(19) Tuovinen, K. *Toxicology* **2004**, *196*, 31-39.
(20) Marrs, T. C. *Pharmacol. Ther.* **1993**, *58*, 51-66.
(21) Richardson, R. J. *J Toxicol Environ Health* **1995**, *44*, 135-165.
(22) Quistad, G. B.; Barlow, C.; Winrow, C. J.; Sparks, S. E.; Casida, J. E. *Proc Natl Acad Sci U S A* **2003**, *100*, 7983-7987.
(23) Winrow, C. J.; Hemming, M. L.; Allen, D. M.; Quistad, G. B.; Casida, J. E.; Barlow, C. *Nat Genet* **2003**, *33*, 477-485.
(24) Damodaran, T. V.; Abdel Rahman, A.; Abou-Donia, M. B. *Neurochemical Research* **2000**, *25*, 1579-1586.
(25) Hill, C. M.; Li, W. S.; Thoden, J. B.; Holden, H. M.; Raushel, F. M. *J Am Chem Soc* **2003**, *125*, 8990-8991.
(26) Johnson, J. L.; Cusack, B.; Hughes, T. F.; McCullough, E. H.; Fauq, A.; Romanovskis, P.; Spatola, A. F.; Rosenberry, T. L. *Abstracts of Papers, 226th ACS National Meeting, New York, NY, United States, September 7-11, 2003* **2003**, BIOL-150.
(27) Watkins, L. M.; Kuo, J. M.; Chen-Goodspeed, M.; Raushel, F. M. *Proteins: Structure, Function, and Genetics* **1997**, *29*, 553-561.
(28) Jortner, B. S. *Toxicology and Applied Pharmacology* **2008**, *233*, 162-167.
(29) Kavitha, P.; Rao, J. V. *Environmental Toxicology and Pharmacology* **2008**, *26*, 192-198.
(30) Muthulakshmi, R.; Bindhuja, M. D.; Revathi, K.; Saravanan, R. *Indian Journal of Environment and Ecoplanning* **2008**, *15*, 199-206.
(31) Rotundo, R. L.; Ruiz, C. A.; (University of Miami, USA). Application: WO
WO, 2008, pp 36pp.
(32) Liu, X.; Sood, S.; Liu, H.; Horner, R. L. *Journal of Physiology (Oxford, United Kingdom)* **2005**, *565*, 965-980.
(33) Purves, D.; Augustine, G. J.; Fitzpatrick, D.; Katz, L. C.; LaMantia, A.-S.; McNamara, J. O.; Williams, S. M. *Neuroscience, 2nd Edition*; Sinauer Associates, 2001.
(34) Svedberg, M. M.; Bednar, I.; Nordberg, A. *Neuropharmacology* **2004**, *47*, 558-571.
(35) Svedberg, M. M.; Svensson, A.-L.; Bednar, I.; Nordberg, A. *Neuroscience Letters* **2003**, *340*, 148-152.
(36) Casida, J. E.; Quistad, G. B. *Chemical Research in Toxicology* **2004**, *17*, 983-998.
(37) Eldefrawi, M. E.; Albuquerque, E. X.,Sch. Med.,Univ. Maryland,Baltimore,MD,USA., (1987).
(38) Lockridge, O.,Annual Report A811804, US Army MRMC, (2002).
(39) Lockridge, O.,Annual Report A962724, US Army MMRC, (2004).
(40) Potter, W. T.; Garry, V. F.; Kelly, J. T.; Tarone, R.; Griffith, J.; Nelson, R. L. *Toxicology and Applied Pharmacology* **1993**, *119*, 150-155.
(41) Chang, P.; Wu, Y. *Zhongguo Yaolixue Yu Dulixue Zazhi* **2005**, *19*, 462-465.
(42) Chang, P.; Wu, Y. *Zhonghua Laodong Weisheng Zhiyebing Zazhi* **2006**, *24*, 382-384.
(43) Glynn, P. *Arhiv za Higijenu Rada i Toksikologiju* **2007**, *58*, 355-358.
(44) World Health Organization,Environmental Health Critera #63, (1986).

(45) Auman, J. T.; Seidler, F. J.; Slotkin, T. A. *Developmental Brain Research* **2000**, *121*, 19-27.
(46) Garcia, S. J.; Seidler, F. J.; Slotkin, T. A. *Environmental Toxicology and Pharmacology* **2005**, *19*, 455-461.
(47) Huff, R. A.; Abu-Qare, A. W.; Abou-Donia, M. B. *Archives of Toxicology* **2001**, *75*, 480-486.
(48) Meyer, A.; Seidler, F. J.; Aldridge, J. E.; Tate, C. A.; Cousins, M. M.; Slotkin, T. A. *Environmental Health Perspectives* **2004**, *112*, 295-301.
(49) Pope, J. *J. Toxicol. Environ. Health B Crit. Rev.* **1999**, *2*, 161-181.
(50) Song, X.; Seidler, F. J.; Saleh, J. L.; Zhang, J.; Padilla, S.; Slotkin, T. A. *Toxicology and Applied Pharmacology* **1997**, *145*, 158-174.
(51) Dickinson, J. A.; Hanrott, K. E.; Mok, M. H. S.; Kew, J. N. C.; Wonnacott, S. *Journal of Neurochemistry* **2007**, *100*, 1089-1096.
(52) Dickinson Jane, A.; Hanrott Katharine, E.; Mok, M. H. S.; Kew James, N. C.; Wonnacott, S. *J Neurochem* **2007**, *100*, 1089-1096.
(53) Henning, R. H.; Duin, M.; van Popta, J. P.; Nelemans, A.; den Hertog, A. *British Journal of Pharmacology* **1996**, *117*, 1785-1791.
(54) Rosen, L. B.; Greenberg, M. E. *Proc Natl Acad Sci U S A* **1996**, *93*, 1113-1118.
(55) Evellin, S.; Nolte, J.; Tysack, K.; vom Dorp, F.; Thiel, M.; Oude Weernink, P. A.; Jakobs, K. H.; Webb, E. J.; Lomasney, J. W.; Schmidt, M. *Journal of Biological Chemistry* **2002**, *277*, 16805-16813.
(56) Wenzel, B.; Elsner, N.; Heinrich, R. *Journal of Neurophysiology* **2002**, *87*, 876-888.
(57) Aschner, M., Personal communication, 23 December 2005.
(58) Sun, X. H.; Liu, X. B.; Martinez, J. R.; Zhang, G. H. *Archives of Oral Biology* **2000**, *45*, 621-638.
(59) Turner, T. J. *Neuroscience* **2004**, *24*, 11328-11336.
(60) Jacobsson, S. O.; Cassel, G. E.; Karlsson, B. M.; Sellstrom, A.; Persson, S. A. *Arch Toxicol* **1997**, *71*, 756-765.
(61) Favaron, M.; Manev, H.; Siman, R.; Bertolino, M.; Szekely, A. M.; DeErausquin, G.; Guidotti, A.; Costa, E. *Proc Natl Acad Sci U S A* **1990**, *87*, 1983-1987.
(62) Candeo, P.; Favaron, M.; Lengyel, I.; Manev, R. M.; Rimland, J. M.; Manev, H. *J Neurochem* **1992**, *59*, 1558-1561.
(63) Peterson, B. Z.; DeMaria, C. D.; Yue, D. T. *Neuron* **1999**, *22*, 549-558.
(64) Russell, T. J.; Watson, G. M. *Journal of Experimental Zoology* **1995**, *273*, 175-185.
(65) Tokumitsu, H.; Soderling, T. R. *Journal of Biological Chemistry* **1996**, *271*, 5617-5622.
(66) Finnegan, S. G.; Lemmon, V. P.; Koenig, E. *Developmental Biology (Orlando, FL, United States)* **1993**, *156*, 230-242.
(67) Pereira, C.; Santos, M. S.; Oliveira, C. *Neurobiol Dis* **1999**, *6*, 209-219.
(68) Yuyama, K.; Yamamoto, H.; Nishizaki, I.; Kato, T.; Sora, I.; Yamamoto, T. *J Neurosci Res* **2003**, *73*, 351-363.
(69) Pozzan, T.; Di Virgilio, F.; Vicentini, L. M.; Meldolesi, J. *Biochem J* **1986**, *234*, 547-553.
(70) Vicentini, L. M.; Ambrosini, A.; Di Virgilio, F.; Meldolesi, J.; Pozzan, T. *Biochem J* **1986**, *234*, 555-562.
(71) Siegel, P. M. *Basic Neurochemistry, Molecular, Cellular, and Medical Aspects, 6th Edition.*; Lippencott, Williams, and Wilkins: Philadelphia, 1999.
(72) Fernstrom John, D.; Fernstrom Madelyn, H. *The Journal of nutrition* **2007**, *137*, 1539S-1547S; discussion 1548S.
(73) Morita, K.; Teraoka, K.; Oka, M.; Hamano, S. *Neurochemistry International* **1992**, *20*, 229-235.
(74) Seno Di Marco, G.; Vio, C. P.; Pavao dos Santos, O. F.; Schor, N.; Casarini, D. E. *Cellular Physiology and Biochemistry* **2007**, *20*, 919-924.

(75) Rebois, R. V.; Reynolds, E. E.; Toll, L.; Howard, B. D. *Biochemistry* **1980**, *19*, 1240-1248.
(76) Chen, Y. A.; Scales, S. J.; Duvvuri, V.; Murthy, M.; Patel, S. M.; Schulman, H.; Scheller, R. H. *J Biol Chem* **2001**, *276*, 26680-26687.
(77) Asanuma, M.; Miyazaki, I.; Ogawa, N. *Neurotox Res* **2003**, *5*, 165-176.
(78) Lambeth, M.; Kushmerick, M. *Ann. Biomed. Eng.* **2002**, *30*, 808-827.
(79) Cortassa, S.; Aon, M. A.; Marban, E.; Winslow, R. L.; O'Rourke, B. *Biophys J* **2003**, *84*, 2734-2755.
(80) Bhalla, U. S.; Iyengar, R. *Science* **1999**, *283*, 381-387.
(81) Eichwald, C.; Kaiser, F. *Biophys J* **1993**, *65*, 2047-2058.
(82) Forouzan, F.; Bard, A. J.; Mirkin, M. V. *Isr. J. Chem.* **1997**, *37*, 155-163.
(83) Dimitrakopoulos, L. T.; Dimitrakopoulos, T. *Electroanalysis* **2001**, *13*, 161-163.
(84) Mahler, H. R.; Cordes, E. H. *Biological Chemistry, 2nd Edition*; Harper and Row: New York, 1971.
(85) Richard, P.; Teusink, B.; Hemker, M. B.; Van Dam, K.; Westerhoff, H. V. *Yeast* **1996**, *12*, 731-740.

CHAPTER IV

METABOLIC PROFILING OF PANCREATIC ISLETS *VIA* MAMP AND SECM

Introduction

Diabetes Mellitus is a disease that currently affects approximately 246 million people worldwide,[1] resulting in impairment of physiological glucose metabolism. Diabetes is currently the fourth leading cause of death by disease world-wide, with one person every 10 seconds dying from a diabetes-related cause.[1] Normal glucose homeostasis is regulated in the pancreas by the islets of Langerhans through a feedback loop involving production of the hormones insulin and glucagon. There are three recognized subtypes of diabetes; type I diabetes, also known as early-onset diabetes, is generally thought to result from autoimmune destruction of insulin producing β-cells within the islets themselves, type II diabetes is caused by insulin resistance in muscle and liver tissue, which prevents uptake and storage of glucose in the body, and gestational diabetes, the final type, which only occurs during pregnancy. Regardless of the cause, chronic elevated glucose levels inevitably lead to abnormally high levels of reactive oxygen species in the blood, which in turn cause the symptomatic damage to the eyes, kidneys, nerves, and blood vessels.[2]

Pancreatic islets are true micro organs, consisting of four different cell types; α-cells which produce glucagon, β-cells which produce the hormone insulin, δ-cells which produce somatostatin, and pancreatic polypeptide producing PP-cells.[3] Glucose homeostasis is maintained specifically through the activities of α-cells, which produce glucagon in the event of hyperglycemia (low glucose), β-cells which produce insulin in the event of hypoglycemia (high glucose), and δ-cells whose role is the paracrine modulation of their neighboring α- and β-cells.[4] Therefore it is the antagonist action of both insulin and glucagon that ensures glycemia within the physiologically normative range.

While a majority of research focuses on murine (mouse or rat) islets, there are differences between murine and human islets. Murine islets, for example, tend to have higher concentrations of β-cells (85% *vs*. 54 % for human islets) and they are all located at the islet core (*vs*. a random cross-sectional distribution for human islets).[5,6] Insulin secretion can be triggered by glucose, K^+, amino acids, and a variety of other molecules.[7-10] Glucose stimulated insulin release has been shown to be biphasic in nature, with an initial short burst followed by a longer, sustained release.[11] The shorter bursts are thought to come from a β-cell 'ready release pool' while the sustained bursts come from a 'reserve pool.' The release of insulin from islet β-cells is known to be pulsatile in nature due to a cascading chain of events beginning with oscillations in membrane potential, which cause oscillations in Ca^{2+}, which in turn drive oscillations in insulin production.[12] The pulsatile nature of insulin release results in oscillations in blood concentrations *in-vivo* with two predominant periods, one high frequency (6 – 10 minutes) and the other low frequency (140 minutes), which is also called the ultradian periodicity.[13,14]

The first generation of islet viability assays were typically derived from general cell culture techniques (*i.e.*, dye based techniques),[15] and did not focus on insulin production capacity of pancreatic β-cells. This posed a problem because the islet as a whole has been shown to continue living after its β-cells have died.[16] Currently utilized non-electrochemical assays require either static immersion or perfusion while exposed to both low (2.8 – 3.3 mM) and high (16.7 – 20 mM) physiological glucose levels. The insulin secreted is then detected via *ex-situ* analysis utilizing radioimmunoassay,[17] chemiluminescence,[18] fluorescence microscopy,[19] or ELISA.[20]

Initial publications for electrochemical methods to assay insulin secretion itself utilized indirect methods of detection. In 1996, Barbosa[21] and co-workers discovered that the electroactive amine 5-HT, upon entering an islet, concentrates within insulin granules. Upon stimulation, the 5-HT is secreted along with insulin, and can be detected at a glass shielded carbon-fiber microelectrode. Without knowing the ratio of insulin to 5-HT within the granules,

however, quantitative estimations of insulin secretion are not possible. Later researchers have utilized chip-based capillary electrophoresis,[22] which is able to quantify insulin secretion with detection limits as low as 0.8 nM and at a 6 second sampling frequency, but which also requires the addition of fluorescein isothiocyanate-labeled insulin and a monoclonal anti-insulin antibody for detection. Anodic stripping voltammetry at a bismuth-coated glassy GCE[23] is also employed to indirectly detect insulin via its zinc co-factor. Finally, insulin exocytosis from isolated pancreatic β-cells can also be detected by changes in membrane capacitance,[24] but this method is not quantitative.

Direct electrochemical detection of insulin would be preferable, as it requires no added agents for detection, and would provide a real-time measure of insulin secretion, which would of course be the preferred assay of islet viability. One potential problem with direct electrochemical detection, however, could be the possibility of interference by somatostatin which is produced by islet δ-cells and has an oxidation potential close to that of insulin itself (+ 0.80 V for somatostatin, *vs*. + 0.88 V for insulin).[25] Early attempts at direct electrochemical insulin detection centered on ruthenium or iridium based systems. These included ruthenium dioxide/cyanoruthenate sensors,[26,27] ruthenium oxide films on carbon-fiber electrodes,[28] ruthenium metallo-dendrimers,[29] or iridium oxide films on glassy carbon.[30] The ruthenium oxide/dendrimer systems, however, have mixed redox states which result in complex electron transfer kinetics.[31] Likewise, the iridium oxide systems suffer from reduced kinetics due to the slower nature of proton transport, resulting in a slower electrode response and, more importantly, pH sensitivity. [32]

Recent years have seen the move toward biosensors based on carbon nanotubes, because of reduced susceptibility to biofouling[33] and increased electrocatalytic properties.[34] More recently, studies have shown specific propensity to catalyze electron transfer at biomolecules[35,36] as well as at embedded protein redox centers.[37,38] Wang and Musameh were the first to show insulin detection at a GCE modified with a multiwalled carbon nanotube/N,N-

dimethylformamide (MWCNT/DMF) film.[39] More recent efforts by Wang's group include a nanotube modified ruthenium oxide electrode, which further reduces biofouling tendencies, but adds the same pH sensitivity and mixed oxidation states of previous oxide films.[40] A chitosan/MWCNT composite electrode has also been demonstrated for insulin oxidation,[41] but the technique resulted in film thicknesses of ~ 10 μm, which is not feasible for use with UME sensors. An alternative MWCNT composite insulin sensor featuring DHP[42] has been previously developed in our labs during development of the multianalyte microphysiometer.[42-46] DHP is a relatively small vinyl ether (Fig. 4.1) that has been shown to self-polymerize, which allows for thinner adherent MWCNT films to be cast onto UME sensors. Furthermore, the MWCNT/DHP sensor was found to have a higher sensitivity, and a higher film cohesion, than the MWCNT/DMF sensors.[47]

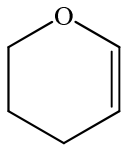

3,4-dihydro-2*H*-pyran

Figure 4.1; 3,4-dihydro-2H-pyran (DHP) is known to self polymerize, providing cohesion to the MWCNT film.

Recent studies in our lab have utilized the MAMP to study the metabolic activity of a wide variety of cell types, and with the addition of the MWCNT/DHP sensor we can now apply the MAMP toward pancreatic islet studies as well. Since it has been shown that lactate dehydrogenase (LDH) in islet β-cells is roughly 1/8 of that in other islet cell types, β-cells are thought to produce little, if any, lactate.[48] This fact gives us the opportunity to perform simultaneous measurements that target both β-cell metabolism (through insulin) and α-, δ-, and PP-cell metabolism (through lactate).

Experiments performed in the MAMP, however, track an *averaged* change in metabolism across a large number of islets (typically 75 – 100). While this allows us to follow

the overall response of the islet population, it does not permit the study of individual islets. In order to observe the activities of a single islet, which could lead to a better understanding of intra-islet metabolism and signaling, a more sensitive technique, and one more appropriate to the spatial scale of a single pancreatic islet, must be applied.

SECM has proven a valuable tool in the investigations of a variety of biological phenomena,[49-52] especially due to its ability to generate spatio-temporal maps of metabolic flux across a cell surface. Recent adaptations in the instrumentation of SECM have allowed easier inclusion of biological samples in experiments. These instruments are termed biological scanning electrochemical microscopes (Bio-SECM),[53] and typically feature the inclusion of an inverted microscope (for both assistance in positioning electrodes and imaging the subject) as well as other elements critical for maintaining a viable biological environment (stage heaters, perfusion, etc.).

The inception of SECM single cell investigations has led to a number of studies focusing on a variety of cell types, and extensive reviews are available elsewhere.[54,55] The difference in redox activities between metastatic and non-metastatic human breast cancer cells have been studied extensively.[56-60] These studies have also identified a class of redox mediators that are capable of penetrating the cell membrane, and investigated their distribution between the cytosol and nucleus. Several works have been published as well on the neuronal analog PC12 cell line, including imaging of topography and mitochondrial respiration[61-63] (also see Chapter 5), real-time changes in morphology,[64] as well as catecholamine release.[65] Recent work with other cell lines has included the imaging of NO release from T-HUVEC cells,[66] HeLa cell activity through the use of a ferrocene derivative,[67] and conversion of menadione to thiodione in single hepablastomas.[68] Work in our labs has also added the capability of using enzyme-coated UMEs to study the metabolic profiles of both glucose and lactate in cultured fibroblasts (see chapter 5), and to image analogs of ion channel systems in reconstituted lipid bilayer membranes (see chapter 6).

Experimental

Materials

All materials were used without modification unless otherwise noted. Insulin (from bovine pancreas, 27 USP units/mg) was purchased from Sigma. 3,4-Dihydro-2H-pyran (DHP), and Tween-80 were purchased from Acros, and KCl from Fisher. Cell-Tak™ cell and tissue adhesive was purchased from BD Biosciences. Glassy carbon rods (1 mm diameter) were obtained from Structure Probe, Inc. (West Chester, PA). Platinum rod (2 mm) was purchased from VWR. All microphysiometer consumables were purchased from Molecular Devices (Sunnyvale, CA). Insulin solutions were prepared from a stock of 10 mg/mL solution of insulin in 19.6 mM hydrochloric acid containing 0.02% v/v Tween-80. Dilutions were then made in 50 mM phosphate buffer (pH 7.4, 0.02% v/v Tween-80) immediately before use in experiments. MWCNTs were obtained as a gift from Dr. William Hofmeister and were manufactured as a byproduct of diamond deposition by microwave assisted chemical vapor deposition using an iron catalyst. An Astex Large Area Diamond Deposition System with a 5 kW microwave source was used. Nanotubes were purified through treatment with nitric acid, following the method of Dujardin *et al.*,[69] to remove the remaining catalyst and aggregates. Following purification, the nanotubes were dried in an oven (1300U, VWR Scientific) and stored in a desiccator.

ASTM Type I (18 MΩ) analytical grade deionized water (DI) was obtained with a Solution 2000 Water Purification System from Solution Consultants. All solutions used in UME analyses or for SECM imaging were filtered prior to use with 0.2 μm syringe filters from Fisher. Ferrocenylmethyltrimethylammonium hexafluorophosphate (FcTMA) was prepared according to the method of Mirkin and co-workers.[70]

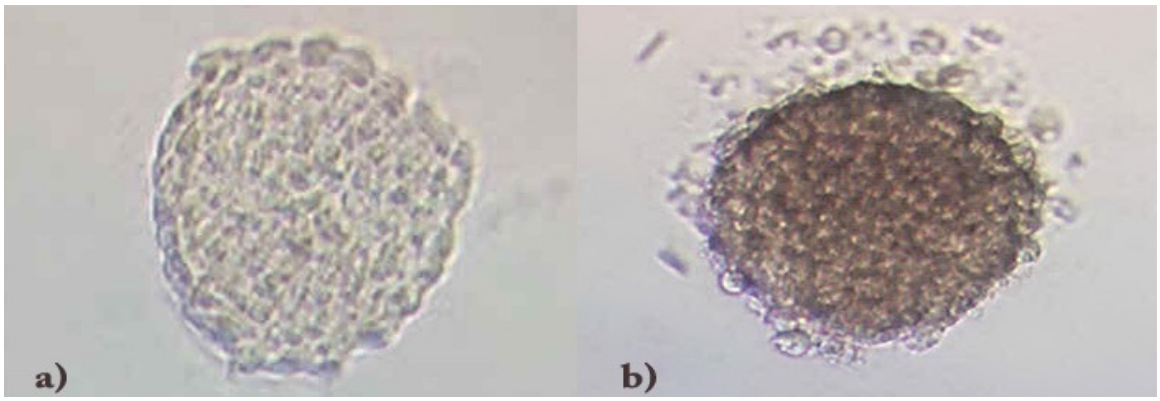

Figure 4.2; Islets were visually inspected prior to selection for experiments in the MAMP and the SECM. Healthy islets (a) were intact and translucent with a white to golden color, while unhealthy islets (b) had dark coloration (due to necrosis) and were observed to shed dying cells.

Islets

Male Friend leukemia virus B (FVB) mice were made available by the Islet Isolation Core of the Vanderbilt Diabetes Research and Training Center, where islets were isolated from these mice by Dr. Zhongyi Chen as described by Brissova *et al.*[71] FVB mice have been used previously as control models for basal levels in a number of studies of the effect of gene modification on insulin secretion.[72-74] The islets were cultured overnight in RPMI with 10% fetal bovine serum and 11 mM glucose. Upon receipt the islets were stored in an incubator at 37 °C and 5% CO_2 and typically used within 24 hours. Optical microscopy was used to qualitatively judge viability when choosing islets for both culturing and imaging. A transparent to golden color was indicative of a healthy subject (see fig. 4.2a), while the presence of necrotic (darkened) spots, or the visible shedding of cells, was indicative of a non-viable islet (see fig 4.2b).

In preparation for islet MAMP experiments, Cytosensor® capsule cups were coated with the tissue adhesive Cell-Tak™, then were dried at 37 °C, rinsed, then dried again. Islets, numbering 75 – 100, were handpicked from the culture media using a manual pipette, then rinsed 3x in 1 mM phosphate buffer supplemented with 100 mM NaCl and then placed onto the capsule

cup membrane. The islets were then coated with 5 µL of agarose, following the Molecular Devices suggestion for non-adherent cells in the Cytosensor Microphysiometer® (Fig. 4.3).[69]

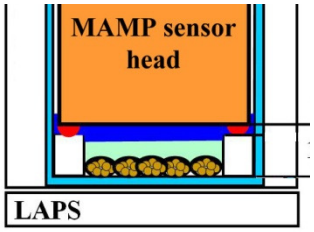

Figure 4.3; A schematic of the agarose entrapment of islets in the MAMP. The islets (in gold) are at the bottom of the capsule cup (light blue) and covered with 5 µl of agarose (green).

Prior to SECM experiments, the islets were individually washed by a series of manual extractions, each taking the minimum possible volume of liquid, under a stereo microscope via a manual micropipette into a much larger volume of fresh media (Hanks Buffered Salt Solution, HBSS) in a new, sterile culture dish. 35 mm glass bottom culture dishes (WillCo dishes), used for imaging, were initially coated with 10 µl Cell-Tak (BD Biosciences) to promote adhesion, then dried in an oven (1300U, VWR Scientific) at 37 °C for two hours, rinsed with several washings of sterile DI water (~100 µl each), then returned to the oven for a second drying. The islets were then transferred (also using the minimum possible volume) onto the coated surface of the culture dish, and covered with HBSS supplemented with 5 mM glucose. In preparation for imaging, dishes were removed from the incubator and placed in the stage warmer, and fresh media applied. The islets were allowed to rest at least 30 minutes, in order for the entire system to equilibrate and reach proper physiological temperature prior to imaging.

Instrumentation

a. CH Instrument 660A potentiostat

Electrochemical measurements for calibration and sensitivity testing were performed using a model 660A potentiostat (CH Instruments, Austin, TX), in the included Faraday cage

with picoamp current booster, and using a standard 3-electrode electrochemical setup. Experiments utilized MAMP sensor heads and UMEs as WE, commercial macro Ag/AgCl REs (CH Instruments model CHI111), and Pt mesh or coiled Pt wire CEs fabricated in our lab. Prior to use in experiments, insulin sensors (both for MAMP and SECM) were tested for sensitivity using constant potential amperometry with standard additions of insulin to 50 mM phosphate buffer (pH 7.4, 0.02 % v/v Tween-80). LSV was accomplished using a scan rate of 50 $mV \cdot s^{-1}$, while the bias used for constant potential amperometry was + 0.88 V *vs*. Ag/AgCl, 2M KCl RE.

b. MAMP

Islet experiments performed in the MAMP utilized a sensor head with an integrated 1 mm GCE in the place of the 0.5 mm Pt glucose sensor (see chapter 3 section B1). Electrical connection to the GCE was provided *via* silver epoxy to a Pt wire, and the assembly was sealed with Hysol® epoxy. The MWCNT solution was prepared in DI water (10.5 $mg \cdot ml^{-1}$), and the MWCNTs were dispersed by sonication. After 15 minutes 10 mg DHP was added while the suspension remained in the sonicator, and sonication was continued for another 15 minutes to mix thoroughly. MAMP insulin sensors were fabricated by drop-casting 3 µL of the MWCNT/DHP solution onto the electrode surface.

Due to hardware limitations, the glucose and lactate sensors in MAMP are forced to share the same potentiostat channel. This is typically not a problem, since they require the same potential bias. However, for islet experiments the glucose sensor in the MAMP was replaced with a MWCNT/DHP insulin sensor, requiring the potential bias of both to be set to + 0.88 V in order to enable insulin detection during the experiments. The lactate sensor was prepared as previously described (see chapter 3 section B1). All potentials reported for MAMP experiments are *vs.* Ag/AgCl, 2 M KCl.

Experiments in the MAMP that utilized a flow/stop-flow cycle were performed with 40 seconds of quiescent stop-flow, when measurements are performed, followed by 140 seconds of media flow ($20\ \mu l \cdot min^{-1}$) to replenish nutrients and remove waste from the cell chamber.

Continuous flow measurements were made using a slower flow rate of 4 $\mu l \cdot min^{-1}$. The media used all for islet experiments was HBSS (‘*running media*’), supplemented with glucose at either 2.8 mM (hereafter low glucose) or 16.7 mM (hereafter high glucose). In flow/stop-flow experiments, islets were initially perfused with low glucose HBSS for 40 minutes, followed by high glucose HBSS for 40 minutes, and finally returning to low glucose HBSS for 30 minutes. Flow/stop-flow experiments performed to determine effects of K^+ stimulation were done with the following sequence: low glucose (45 min.), high glucose (45 min.), low glucose (30 min.), high glucose (45 min.), low glucose (30 min.), low glucose + 50 mM KCl (48 minutes), then returning to low glucose. Identical control experiments were conducted in the absence of islets to determine the effect of variable glucose levels on the sensor response.

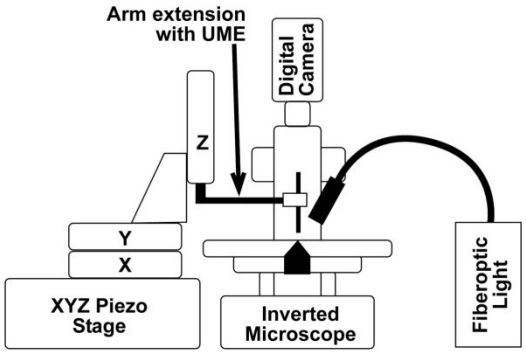

Figure 4.4; Schematic of the Bio-SECM setup incorporating an arm extension to hold the UME, inverted microscope with digital camera, and a fiberoptic light for additional illumination.

c. SECM

Experiments were performed using a Bio-SECM setup incorporating an inverted microscope (VistaVision, VWR) with digital camera (Pixera professional from Pixera Corp.), microscope stage temperature control with objective heater (TCII micro temperature controller, BioScience Tools) and a CH Instruments model 900 SECM (fig. 4.4) operating in the constant height mode. The use of an arm extension to hold the ultramicroelectrode (UME) allowed the positioning of the piezo micropositioners beside, rather than atop, the microscope platform. This

placement allows the microscope stage to move independently of the SECM tip so that cells/islets may be quickly positioned near the UME for imaging. The microscope stage and heater have been modified to adjust for substrate tilt (Fig. 4.5) by fabricating a stage insert that permits the heating stage to reside below the plane of the microscope stage. This prevents z-axis adjustments to level the substrate from moving the dish out of the short working distance of the microscope objectives. The heating stage '*floats*' below the stage insert and is held in place against the leveling screws by high strength rubber tubing, which wraps around the top of the stage insert to secure the heating stage. Since the microscope stage heater was designed for perfusion-type experiments, the internal thermocouple was removed from the perfusion tubing track, sterilized in EtOH, and placed directly into the cell culture dish during experiments to ensure proper temperature control. All reported potentials for SECM experiments are measured versus a Ag/AgCl, 3 M KCl RE.

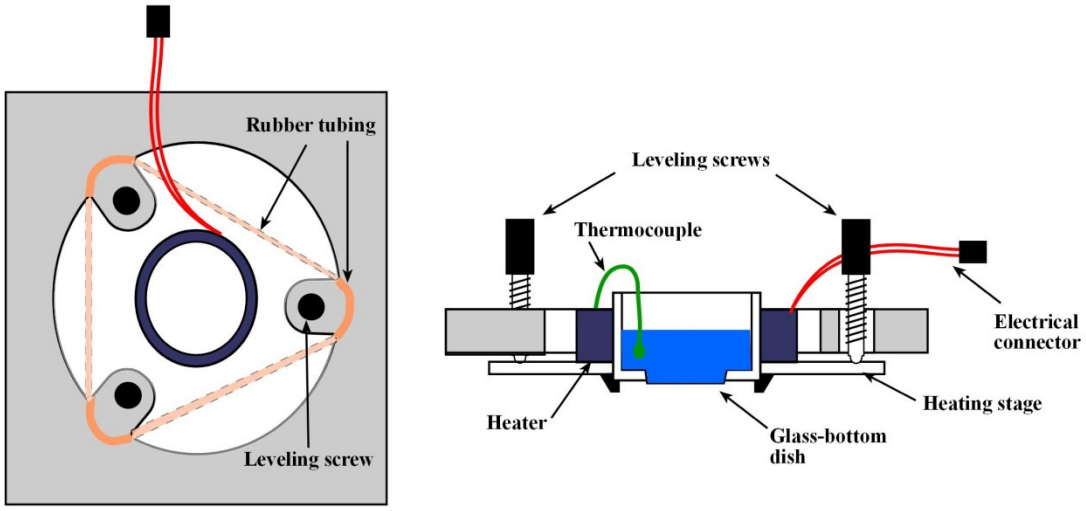

Figure 4.5; The modified stage insert for the inverted microscope top view (left) and a cutout cross section (right). The circular metal heating stage is supported from below by high-strength rubber tubing (orange, shown at left but omitted at right), and substrate tilt is adjusted via the three leveling screws. The heating stage thermocouple (in green) is immersed in the media inside the 35 mm glass-bottom dish to ensure proper temperature is maintained.

All UMEs utilized in these studies were of the disc-sealed-in-glass type, and had RG ratios[50] of ~ 5. Pt 25 μm and 10 μm electrodes were manufactured from Pt wire (Goodfellow), according to the method of Bard,[50] polished using sizes of alumina (Buehler) down to 0.05 μm on a polishing wheel (Metaserv 2000, Buehler), then sonicated in EtOH and DI water. UMEs were then electrochemically polished by cycling their potential in a solution of 0.5 M H_2SO_4. The electrodes were then tested by performing cyclic voltammetry (CV) in a solution of 1 mM FcTMA (E = + 0.65 V). Only Pt UMEs capable of reaching an increase in current of 800% (over initial steady state current values) during approach to a 2 mm Pt disc (*e.g.*, those with $I_T = 8$) were used for imaging purposes. Carbon fiber UMEs (cf-UMEs) were manufactured similar to Pt UMEs except using 7 μm carbon fibers gifted by Dr. Aurelio Galli (Vanderbilt University).

The insulin UME sensor was prepared using a 7 μm cf-UME by a slight modification of the MAMP procedure (see previous section). Casting of the MWCNT film was accomplished by dispensing a single droplet of the solution manually from an Eppendorf tip, and waiting for the MWCNTs to aggregate at the bottom of the droplet. The UME tip was then brought into contact with the mass of MWCNTs in the droplet and held there for 2 seconds, then withdrawn and held inverted (*i.e.*, tip down) until the film dried. The UME sensor was then carefully washed by repeatedly dipping into a vial of DI water and was stored in pH 7.0 phosphate buffer until use.

Probe scan curves (PSCs) and imaging of oxygen respiration were performed using Nafion coated 25 μm or 10 μm Pt UMEs (E_{tip} = − 0.5 V), in HBSS supplemented with 5 mM glucose. The Nafion coating was hand cast by dipping the UMEs in a 5% solution of Nafion in EtOH (Strem), followed by drying with the UMEs in an inverted position, and rinsing repeatedly with DI water. Topographical images were performed via the addition of 1 mM FcTMA to the HBSS islet media, with an uncoated 10 μm Pt UME (E_{tip} = + 0.65 V).

PSCs of insulin were obtained with the use of 7 μm carbon fiber UMEs coated with MWCNT/dihydropyran (E_{tip} = + 0.88V) as previously discussed. Prior to use in imaging

experiments, the UME insulin sensors were calibrated and tested for sensitivity via constant potential amperometry. A stock solution of 1.4 mM bovine insulin was prepared in 0.02% TWEEN detergent (acidified to pH 2.0). This solution was used to spike a pH 7.0 phosphate buffer solution to create total insulin concentrations of 200 nM, 500 nM, and 1 µM. After sensitivity testing, the UMEs were carefully rinsed by dipping into DI water and stored in pH 7.0 phosphate buffer until use. Insulin release was triggered by spiking the media surrounding the islet with sufficient glucose from a stock solution via a micropipette to allow the concentration within the dish to reach 16.7 mM.

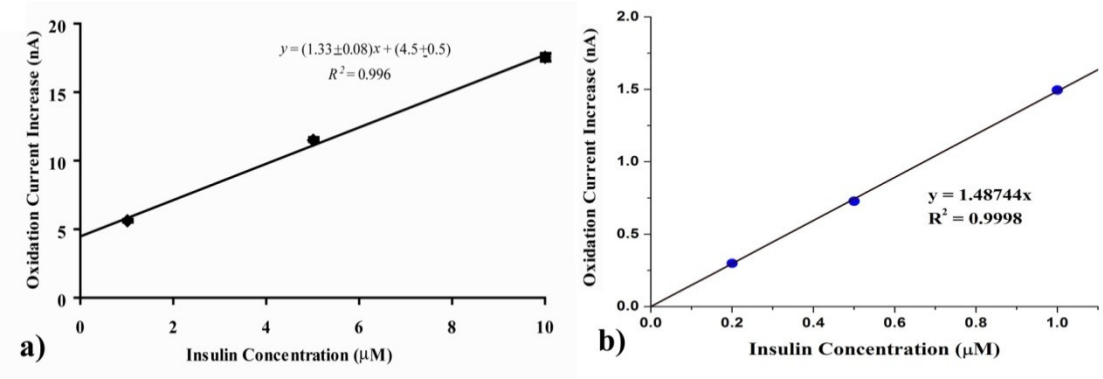

Figure 4.6; Calibration plots for (a) the macro-scale MAMP sensor and (b) the UME SECM insulin sensor. The sensitivities for the electrodes were 1 µM for the MAMP sensor and 200 nM for the UME sensor.

Sensor Calibration

Calibration plots for both an MAMP sensor and a UME insulin sensor are shown in Fig. 4.6. Both sensors show a linear response; with the MAMP the range is from 1 – 10 µM (Fig. 4.6a, $R^2 = 0.996$) while for the UME sensor the linear range is from 0.2 – 1.0 µM (Fig. 4.6b, $R^2 = 0.9998$). The calibration for the MAMP sensor utilizes an average of five stop-flow cycles (n = 5). The UME sensor provides nearly one decade higher insulin sensitivity (200 nM for the UME sensor *vs*. 1 µM for the MAMP sensor), and due to the reduced capacitance and background noise, a highly linear response that intercepts at the origin for zero insulin concentration.

MAMP Islet Experiments

a. Flow/stop flow experiments

The insulin response of a MAMP insulin sensor head during one flow/stop-flow cycle to the physiological release from a group of ~ 100 islets is shown in Fig. 4.7. The figure shows the current change due to the depletion of insulin in the solution immediately surrounding the sensor

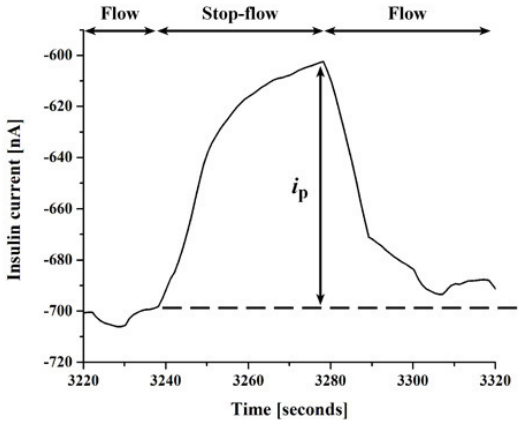

Figure 4.7; The response of an MAMP insulin sensor to the insulin produced by a number of pancreatic islets (~100) during a single stop-flow cycle. The peak current (i_p) is taken as the change from the baseline during the stop-flow period. The current is seen to decrease, instead of increase, due to diffusional limitations.

when the solution flow stops, causing the observed drop in current. The figure also depicts how measurements are made by subtracting the peak current from the baseline to get the peak height (i_p), which is proportional to the insulin present in the media. The raw data from a series of measurements performed using the MAMP insulin sensor in the presence of pancreatic islets (75 – 100), at physiological low and high glucose levels (2.7 mM and 16.8 mM respectively), is shown in Fig. 4.8. The overall sensor response, both baseline and peak size, can be seen to increase from low to high glucose levels, indicating an elevation of insulin exocytosis. In order to

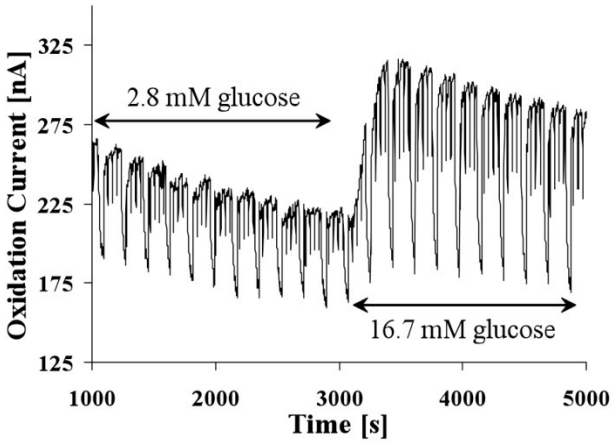

Figure 4.8; Raw MAMP insulin data for an experiment exposing islets (75 – 100) to low physiological glucose levels (2.8 mM) and high physiological glucose levels (16.7 mM).

evaluate the qualitative effect of changing the glucose level, we can assign the output at low glucose levels a normative state, and measure the percent change in activity as a result of increasing to high glucose levels.

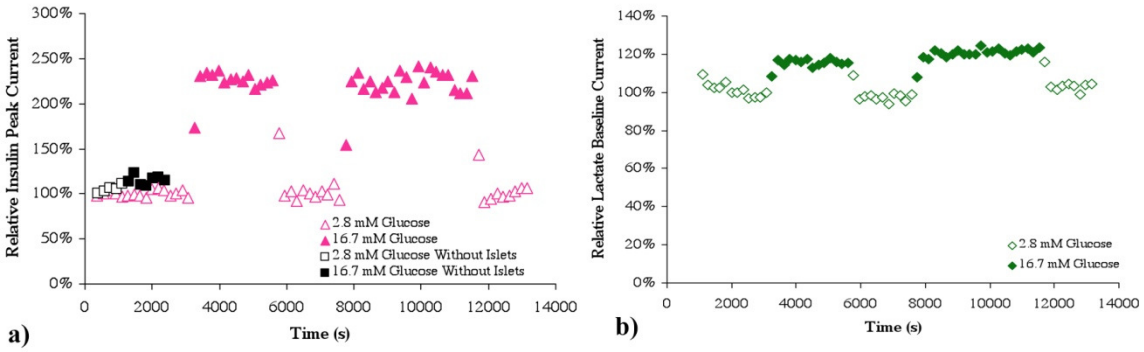

Figure 4.9; The responses of MAMP sensors for (a) insulin and (b) lactate. For the insulin sensor (a), results are shown for low and high glucose both in the absence of (squares) and presence of (triangles) ~ 100 islets, at low (2.8 mM) and high (16.7 mM) physiological glucose levels. (b) shows lactate production in the presence of islets at both low and high physiological glucose levels.

In Fig 4.9 the result of such an evaluation is presented for insulin (4.9a) and lactate (4.9b) production. The plot for insulin sensor response includes data collected both in the absence of (squares) and the presence of (triangles) islets. The data collected in the absence of islets, both at

low glucose (squares with white background) and high glucose (solid black squares) show virtually no significant effect of changing glucose concentration on the sensor in the absence of insulin production. The changes between low (pink triangles with white background) and high glucose levels (solid pink triangles) when islets are present, however, shows an increase of nearly 125% in the insulin signal as a result of increasing the glucose levels. This corresponds to more than double the output of insulin over the basal metabolic rate. When observing the lactate production for the same islets we see an approximately 15% increase in lactate production for high glucose (green diamonds) *vs*. that during low glucose (green diamonds with white background). Therefore when we see increases in both lactate and insulin production we are likely seeing simultaneous increases in metabolic rates of multiple cell types within the islet, further demonstrating the role of the islet as a true micro organ.

Since K^+ is also known to stimulate the release of insulin,[75] an experiment was performed to see if that could be observed in the MAMP, and if so to compare K^+ stimulated release to that of glucose. The result from three MAMP channels for the experiment is shown in Fig. 4.10. Instead of relative changes in insulin output, however, the response has been quantitatively calculated from the sensor's calibration response (see Fig. 4.6a) to show the insulin concentration (in μM) in the MAMP chamber. The figure shows low glucose (pink triangles with white background) and high glucose (solid pink triangles) as in the previous figures, followed by stimulation with 50 mM K^+ (solid purple triangles). As before, we see differing degrees of response to both glucose and K^+, due to the natural variation in physiological activity between the populations of islets. It is clearly visible that, at the level used in this experiment (50 mM K^+), high physiological glucose is a more potent stimulator of insulin release. It is also interesting to note differences in the relative magnitudes of stimulation for the two effectors between groups of islets; while high glucose caused a similar insulin response for Figs. 4.10a and 4.10b, K^+ stimulation for 4.10b is more than twice that seen in 4.10a, and likewise K^+ stimulation is similar

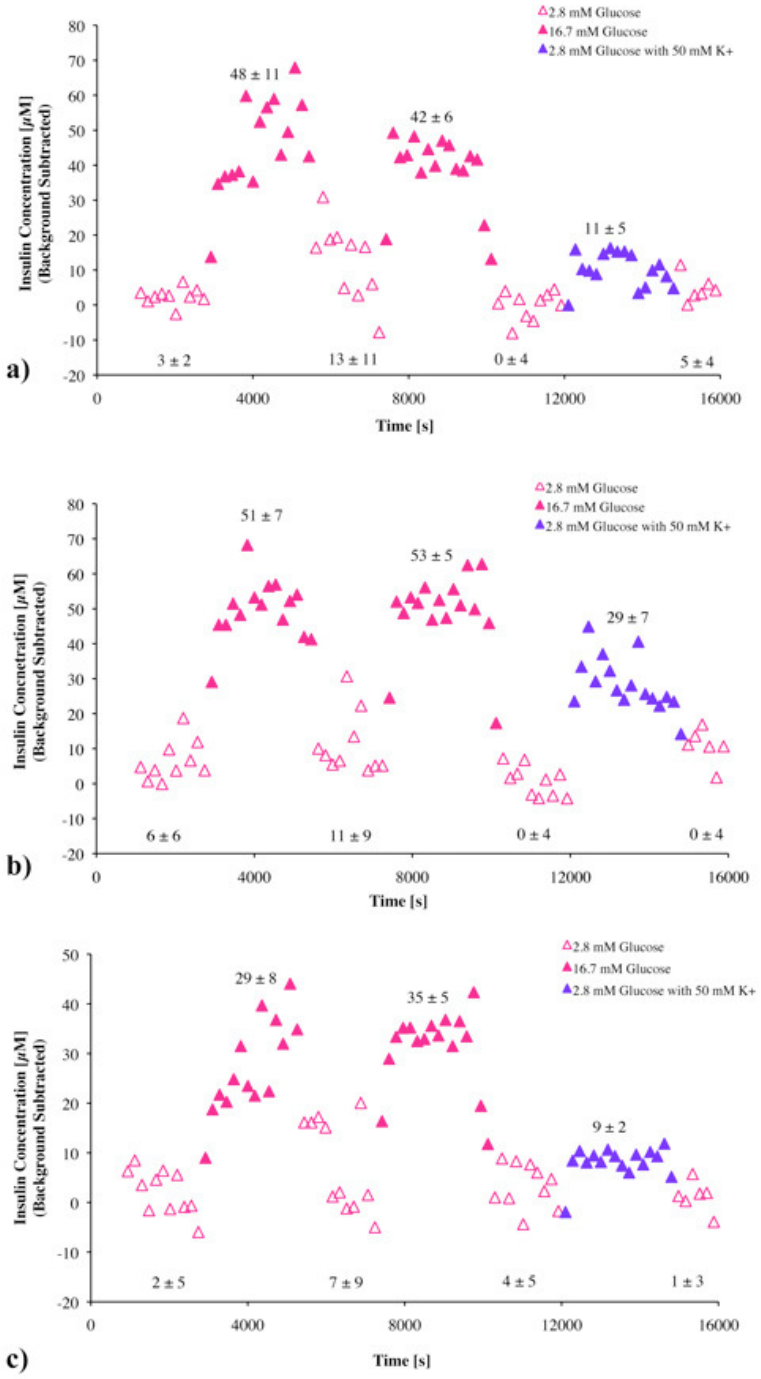

Figure 4.10; The results for the comparison of glucose stimulated (pink triangles) and K^+ stimulated (purple triangles) insulin release from ~ 100 islets in three different MAMP channels during a single experiment.

for 4.10a and 4.10c, but high physiological glucose resulted in nearly twice the insulin levels for 4.10a than seen in 4.10c.

b. Continuous flow MAMP

The MAMP can also be operated in a continuous flow mode, without a programmed flow/stop-flow cycle, like a traditional microfluidic device. The flow/stop flow parameters were initially designed into the Cytosensor® Microphysiometer to improve the sensitivity toward changes in extracellular pH caused by H^+ production. The continuous flow experiment was designed with the hope that it would enable the detection of oscillatory production of insulin, which is not possible in flow/stop-flow mode where temporal resolution is traded for an increase in sensitivity.

In initial control experiments, conducted without the inclusion of islets, it was observed that changing glucose levels affected the current response of the insulin sensor during continuous flow mode. Fig. 4.11 shows the sensor response after baseline correction as the media is changed from low to high and back to low glucose again. The difference in current for the two glucose levels was found to be 9.1 ± 0.9 nA. In order to correct the contribution by glucose to the overall sensor response, a correction value was calculated from this current difference. Since the difference in glucose concentrations between high and low glucose is 13.0 mM, this results in the addition of 0.7 ± 0.1 nA mM^{-1} glucose to the insulin sensor current.

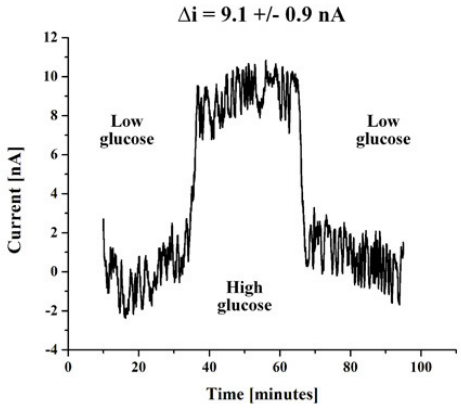

Figure 4.11; Current response of the MWCNT/DHP sensor, after background subtraction, to a change in media glucose concentration from physiological low (2.8 mM) to high (16.7 mM) and back to low. Current difference was 9.1 ± 0.9 nA.

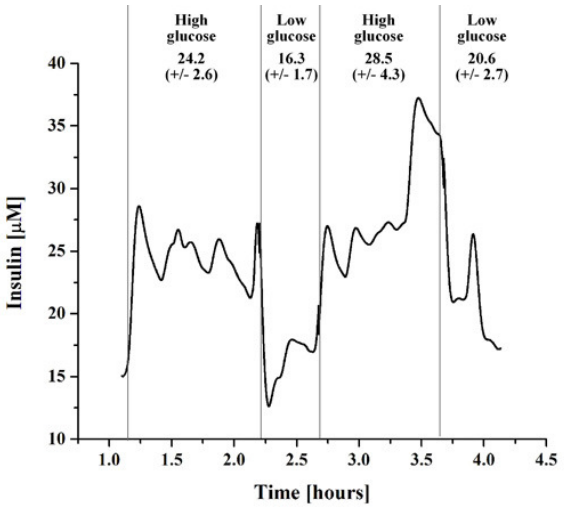

Figure 4.12; Results of a continuous flow MAMP experiment, showing the insulin levels [μM] generated by ~ 100 islets in response to alternating physiologically high (16.7 mM) and low (2.8 mM) glucose concentrations

The results of a live islet continuous flow MAMP experiment are presented in Fig. 4.12. This data has been baseline corrected and corrected for glucose interference for both low and high glucose levels. The figure depicts a continuous flow experiment at a 4 μl min^{-1} flow rate with data collected at 1 sample per second. Unlike the previous flow/stop-flow experiments (see previous section), insulin levels for the continuous flow experiment were calculated using a standard addition calibration (using 1 μM and 25 μM insulin) at the end of the experiment (not shown). The first high glucose interval results in an insulin concentration of 24.2 ± 2.7 μM within the MAMP chamber, followed by a low glucose course resulting in a decrease of insulin levels to 16.3 ± 1.8 μM. Returning the glucose to high levels results in a return to approximately the previous levels (25.8 ± 1.4 μM) for ~ 40 minutes, followed by a sustained higher production of insulin (33.2 ± 3.6 μM) for ~ 11 minutes (data not included on the graph). The average insulin concentration throughout this high glucose course is 28.8 ± 4.4 μM. The final decrease of solution glucose to the low physiological level results in a decrease of insulin to 20.6 ± 2.8 μM throughout the remainder of the experiment.

As previously mentioned, it was hoped that the continuous flow mode would enable the observation of oscillations in islet insulin exocytosis; monitoring of insulin oscillations is not possible in the flow/stop-flow mode. High frequency insulin oscillations have been observed at intervals of 6 – 10 minutes, while low frequency oscillations have been documented at ~ 140 minute intervals.[14] A rudimentary analysis of the data presented in Fig. 4.12 presents two distinct possibilities for periodic insulin production. Fig. 4.13 presents the same data as 4.12, but

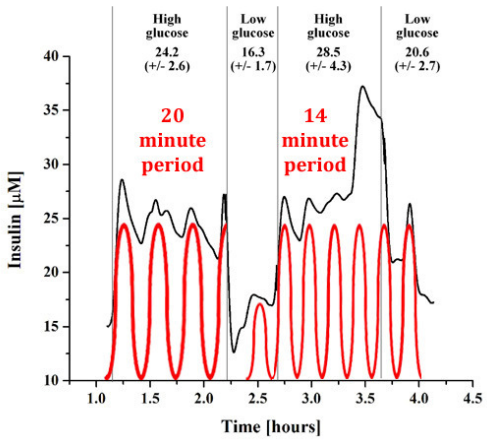

Figure 4.13; Results of an FFT analysis of the continuous flow data, showing only noise in the area from 6 minutes (10 hours^{-1}) to 10 minutes (6 hours^{-1}) where literature indicates high frequency insulin oscillations should occur.

includes red traces representing pulsatile releases at periods of 20 minutes (left) and 14 minutes (right) respectively. While the insulin release is clearly not completely due to pulsatile secretion at these intervals, they possibly represent at least a contribution to the observed insulin output.

SECM Islet Experiments

Topographical imaging was obtained in the form of a false color current profile, which was obtained by the inclusion of a redox mediator (FcTMA, E = + 0.65 V) in the supporting media. Since FcTMA is not permeable to cell membranes[76] the resulting current profile follows

the SECM principle for negative feedback, so that the current decreases as the UME probe gets closer to the islet. The resulting topographical profile for one such islet is shown in figure 4.14a. The PSC trace above the false color image, equivalent to a cross section across the yellow line in the image, shows that the islet presents a roughly spherical profile, slightly flattened around the edges.

Another benefit of the nature of the instrument is the possibility of using the same probe to detect multiple analytes by changing the tip potential. In order to demonstrate this, after acquisition of the full topographical profile the probe potential was reset for oxygen reduction (E_{tip} = − 0.5 V) and a second image was recorded (Fig 4.14b). The current dips as the probe passes over the islet due to the depletion of oxygen in the surrounding media caused by mitochondrial respiration within the individual cells of the islet. It can be seen that the oxygen

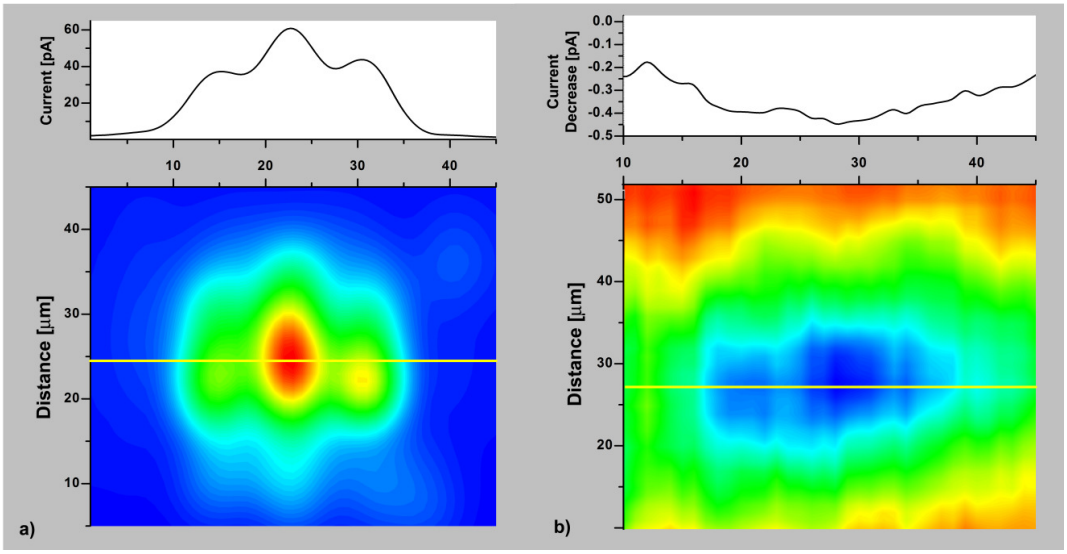

Figure 4.14; (a) A topographical 3D current profile map (FcTMA; E_{tip} = + 0.65 V) and (b) oxygen respiration profile (E_{tip} = - 0.5 V) for a pancreatic islet obtained with a Nafion coated 10 µm Pt UME. The topographical image (a) shows a roughly hemispherical shape and the respiration profile (b) is the approximate mirror image of (a), indicating uniform respiration throughout the islet. The horizontal line across the profile depicts the direction and location of the PSC shown in the inset above each image. Potentials reported *vs*. Ag/AgCl, 3 M KCl.

PSC (Fig. 4.14b, top) is roughly the inverse image of the corresponding topographical PSC (Fig. 4.14a, top) for the same cross section of the islet, inferring a uniform respiration throughout the islet. This is what would be expected since the mechanism for O_2 transport across the cell membrane is passive diffusion. In order to better demonstrate this, Fig. 4.15 depicts a false color current topographical image, with contour lines from a similar oxygen image overlaid on top. The oxygen current proceeds from low to high as the topography goes from high to low.

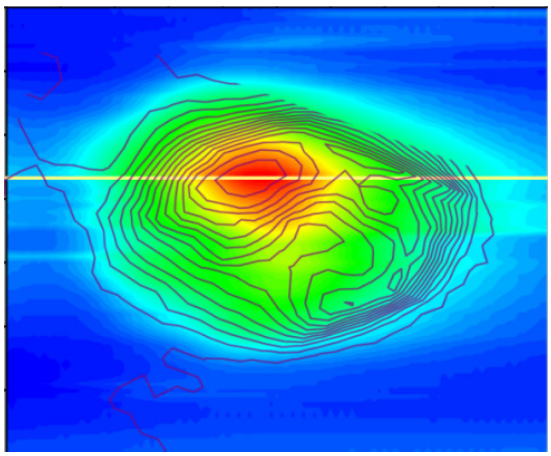

Figure 4.15; The contour lines of an SECM respiratory profile overlaid on the topographical image for the same islet, showing a uniform depletion of O_2 in the media surrounding the islet. The O_2 concentration map is an inverse of topography. Both images obtained with the same 10 µm Pt UME; for respiratory profile E_{tip} = – 0.5 V and for topography E_{tip} = + 0.65 V, both *vs.* Ag/AgCl, 3M KCl RE.

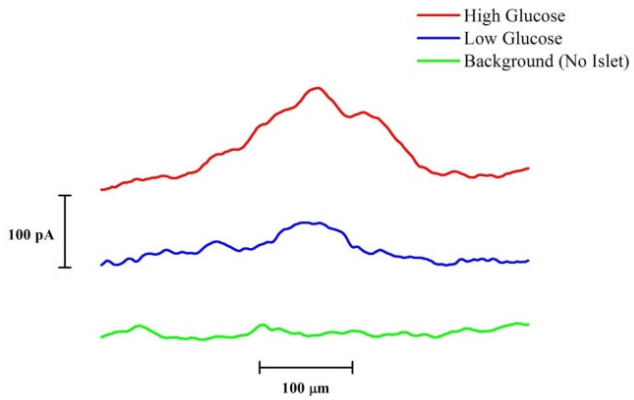

Figure 4.16; Three SPCs from an MWCNT/DHP coated UME sensor. The bottom SPC (green) is a scan across a bare substrate away from an islet, the middle trace (blue) is above an islet at low physiological glucose (2.8 mM), and the top trace (red) is the same cross section of the islet at high physiological glucose (16.7 mM).

In order to demonstrate the capability for detecting the insulin secretion from a live islet, the MWCNT/DHP sensor was utilized in a Bio-SECM within a cell culture dish containing a single pancreatic islet (HBSS, with low glucose), and a series of PSCs were performed (fig. 4.16). The sensor was first approached to the substrate surface, using the assistance of an inverted microscope. In order to acquire a background image, the microscope stage was adjusted in the x-y plane so that the sensor was away from the islet but remained close to the surface, and then the sensor was scanned across the bare dish surface. The resulting background scan (4.16, green trace) shows only noise in the signal, as would be expected. Next the microscope stage was used again to position the islet directly in the path of the sensor, and a second PSC was recorded (4.16, blue trace). A slight insulin signal can be seen through the noise present at the center of the PSC, corresponding to the center of the islet. Finally, the dish was spiked with a stock glucose solution from a micropipette to raise the concentration to the high glucose level, and the final PSC was recorded (4.16, red trace). The triggered insulin release can be seen from the increase in signal between the blue and red traces. These UME sensors were then successfully able to not only detect insulin release by the islet, but more importantly were able to differentiate between the levels of insulin release at high and low physiological glucose levels.

It should be noted that unlike human pancreatic islets, where the insulin producing β-cells are scattered throughout, murine islets contain all their β-cells at the center of the islet's mass.[77,78] This explains the difference in the areas over which insulin could be detected at low and high glucose levels. Since insulin is only secreted from the center of the islet, at low insulin production a smaller cross section of the PSC picks up the signal, while at high insulin production the increased insulin present diffuses outward.

Conclusions

The utility of the MWCNT/DHP sensor toward islet metabolism and studies of diabetes has been shown. The robustness of the insulin sensor toward shear forces present in a

microfluidic environment was also demonstrated, with minimal interference from changes in glucose levels. The sensor was shown to work in both traditional continuous flow microfluidic experiments and in flow/stop-flow MAMP experiments with equivalent sensitivity. The MWCNT/DHP insulin sensor demonstrated adequate sensitivity with a limit of detection of 1 μM for the MAMP sensor and 200 nM for the UME sensor. The MAMP sensor limit of detection was sufficient to detect changes in insulin exocytosis due to both glucose triggered and K^+ stimulated insulin release, and resulting in a qualitative assessment of the effectiveness of those stimuli toward insulin production. The effect of K^+ stimulation on islet insulin secretion was found to be significantly less than that of glucose. Also, the relative intensity of the insulin:K^+ stimulation was found to vary from group to group of the islets observed. Also the simultaneous collection of lactate production shows that metabolic rates of multiple cell types within an islet can be monitored simultaneously.

The applicability of SECM toward the noninvasive exploration of single pancreatic islet metabolism has also been demonstrated. The SECM was used to obtain topographical profiles, insulin release profiles, and cellular respiration profiles of single pancreatic islets. Since pancreatic islets are true micro organs, composed of different cell types performing different biological tasks, the evaluation of their overall functionality is more complex than for single cells. The inclusion of analyte profiles for oxygen, which is indicative of overall cell viability, and insulin release, which is specifically indicative of β-cell activity, into assays for islet viability could result in a more complete evaluation of the overall functionality of the micro organ, especially in those islets destined for human transplantation. While the SECM can not probe multiple analytes simultaneously, it is able to spatially as well as temporally differentiate data obtained from a live cell or organism. While UMEs are currently limited to one electrode, and thus one analyte, this is not a concrete limitation, and as manufacturing techniques as well as the state of the art in imaging is improved, this limitation could be overcome as well.

Acknowledgements

Islets utilized for these studies were obtained with the assistance of Dr. Zhongyi Chen of the Vanderbilt Diabetes Center. Carbon fibers for the cf-UMEs were supplied by Dr. Aurelio Galli of Vanderbilt University, and the Multi-walled carbon nanotubes were a gift from Dr. William Hofmeister of the University of Tennessee Space Institute. The insulin sensor was initially designed by Rachel Snider, and early work with it performed by Amy Rue, both of which are with the Cliffel labs at Vanderbilt University. Finally, all experimental work for this chapter was performed with the assistance of Dr. Madalina Ciobanu, formerly with the Cliffel labs at Vanderbilt University.

References

(1) Gan, D., Ed. *Diabetes Atlas, 3rd. Edition*; International Diabetes Federation, 2007.
(2) Robertson, R. P.; Harmon, J. S. *Free Radical Biology & Medicine* **2006**, *41*, 177.
(3) Montague, W. *Diabetes and the Endocrine Pancreas: A Biochemical Approach*; Oxford University Press: New York, 1983.
(4) Quesada, I.; Todorova, M. G.; Soria, B. *Biophys. J.* **2006**, *90*, 2641-2650.
(5) Rocheleau, J. V.; Walker, G. M.; Head, W. S.; McGuiness, O. P.; Piston, D. W. *Proc. Natl. Acad. Sci. U.S.A.* **2004**, *101*, 12899-12903.
(6) Brissova, M.; Fowler, M.; Nicholson, W.; Chu, A.; Hirshberg, B.; Harlan, D. M.; Powers, A. C. *J. Histochem. Cytochem.* **2005**, *53*, 1087-1097.
(7) Pfeifer, M. A.; Broadstone, V. L. In *The Endocrine Pancreas*; Samols, E., Ed.; Raven Press: New York, 1991.
(8) Schmid, G. M.; Meda, P.; Caille, D.; Wargent, E.; O'Dowd, J.; Hochstrasser, D. G.; Cawthorne, M. A.; Sanchez, J.-C. *J. Biol. Chem.* **2007**, *282*, 12717-12724.
(9) Hiatt, N.; Davidson, M. B.; Chapman, L. W.; Seinkopf, J. A. *Diabetes* **1978**, *27*, 550-553.
(10) Gomez, M.; Curry, D. L. *Endocrinology* **1973**, *92*, 1126-1134.
(11) Straub, S. G.; Sharp, G. W. G. *Diabetes Metab. Res. Rev.* **2002**, *18*, 451-453.
(12) Ravier, M. A.; Eto, K.; Jonkers, F. C.; Nenquin, M.; Kadowaki, T.; Henquin, J. C. *J Biol Chem* **2000**, *275*, 1587-1593.
(13) Tengholm, A.; Gylfe, E. *Mol Cell Endocrinol* **2009**, *297*, 58-72.
(14) Schmitz, O.; Rungby, J.; Edge, L.; Juhl, C. B. *Ageing Res Rev* **2008**, *7*, 301-305.
(15) Bank, H. L. *Diabetologia* **1987**, *30*, 812.
(16) Worcester Human Islet Transplantation Group *N Engl J Med* **2006**, *355*, 1397-1399.
(17) Cunha, D. A.; Carneiro, E. M.; Alves, M. d. C.; Horfe, A. G.; Sousa, S. M.; Boschero, A. C.; Saad, M. J. A.; Velleoso, L. A.; Rocha, E. M. *American journal of Physiology - Endocrinology and Metabolism* **2005**, *289*.
(18) Strong, V. E.; Shifrin, A.; Inabnet, W. B. *Annals of Surgical Innovation and Research* **2007**, *1*, http://www.asir-journal.com/content/1/1/6.
(19) Qian, W.-J.; Peters, J. L.; Dahlgren, G. M.; Gee, K. R.; Kennedy, R. T. *BioTechniques* **2004**, *37*, 922-924,926,928-930,932-933.

(20) Efanov, A. M.; Barrett, D. G.; Brenner, M. B.; Briggs, S. L.; Delaunois, A.; Durbin, J. D.; Giese, U.; Guo, H.; Radloff, M.; Gil, G. S.; Sewing, S.; Wang, Y.; Weichert, A.; Zaliani, A.; Gromada, J. *Endocrinology* **2005**, *146*, 3696-3701.
(21) Barbosa, R. M.; Silva, A. M.; Tome, A. R.; Stamford, J. A.; Santos, R. M.; Rosario, L. M. *Biochemical and Biophysical Research Communications* **1996**, *228*, 100-104.
(22) Shackman, J. G.; Dahlgren, G. M.; Peters, J. L.; Kennedy, R. T. *Lab on a Chip* **2005**, *5*, 56-63.
(23) Maghasi, A. T.; Halsall, H. B.; Heineman, W. R.; Rodriguez Rilo, H. L. *Analytical Biochemistry* **2004**, *326*, 183-189.
(24) Gillis, K. D.; Misler, S. *Pflugers Archiv; European Journal of Physiology* **1991**, *420*, 121-123.
(25) Bennett, G. W.; Brazell, M. P.; Marsden, C. A. *Life Sci.* **1981**, *29*, 1001.
(26) Cox, J. A.; Gray, T. J. *Analytical Chemistry* **1989**, *61*, 2462-2464.
(27) Huang, L.; Shen, H.; Atkinson, M. A.; Kennedy, R. T. *Proceedings of the National Academy of Sciences of the United States of America* **1995**, *92*, 9608-9612.
(28) Gorski, W.; Aspinwall, C. A.; Lakey, J. R. T.; Kennedy, R. T. *Journal of Electroanalytical Chemistry* **1997**, *425*, 191-199.
(29) Cheng, L.; Pacey, G. E.; Cox, J. A. *Analytical Chemistry* **2001**, *73*, 5607-5610.
(30) Pikulski, M.; Gorski, W. *Analytical Chemistry* **2000**, *72*, 2696-2702.
(31) Nagy, Z.; You, H. *Electrochimica Acta* **2002**, *47*, 3037-3055.
(32) Elsen, H. A.; Slowinska, K.; Hull, E.; Majda, M. *Analytical Chemistry* **2006**, *78*, 6356-6363.
(33) Swamy, B. E. K.; Venton, B. J. *Analyst (Cambridge, United Kingdom)* **2007**, *132*, 876-884.
(34) Lawrence, N. S.; Deo, R. P.; Wang, J. *Electroanalysis* **2005**, *17*, 65-72.
(35) Musameh, M.; Wang, J.; Merkoci, A.; Lin, Y. *Electrochemistry Communications* **2002**, *4*, 743-746.
(36) Zhao, Q.; Gan, Z.; Zhuang, Q. *Electroanalysis* **2002**, *14*, 1609-1613.
(37) Gooding, J. J.; Wibowo, R.; Liu, J.; Yang, W.; Losic, D.; Orbons, S.; Mearns, F. J.; Shapter, J. G.; Hibbert, D. B. *Journal of the American Chemical Society* **2003**, *125*, 9006-9007.
(38) Yu, X.; Chattopadhyay, D.; Galeska, I.; Papadimitrakopoulos, F.; Rusling, J. F. *Electrochemistry Communications* **2003**, *5*, 408-411.
(39) Wang, J.; Musameh, M. *Analytica Chimica Acta* **2004**, *511*, 33-36.
(40) Wang, J.; Tangkuaram, T.; Loyprasert, S.; Vazquez-Alvarez, T.; Veerasai, W.; Kanatharana, P.; Thavarungkul, P. *Analytica Chimica Acta* **2007**, *581*, 1-6.
(41) Zhang, M.; Mullens, C.; Gorski, W. *Analytical Chemistry* **2005**, *77*, 6396-6401.
(42) Snider, R. M.; Ciobanu, M.; Rue, A. E.; Cliffel, D. E. *Analytica Chemica Acta* **2008**, *609*, 44-52.
(43) Eklund, S. E.; Cliffel, D. E.; Kozlov, E.; Prokop, A.; Wikswo, J.; Baudenbacher, F. *Analytica Chimica Acta* **2003**, *496*, 93-101.
(44) Eklund, S. E.; Kozlov, E.; Taylor, D. E.; Baudenbacher, F.; Cliffel, D. E. *Methods in Molecular Biology (Totowa, NJ, United States)* **2005**, *303*, 209-223.
(45) Eklund, S. E.; Snider, R. M.; Wikswo, J.; Baudenbacher, F.; Prokop, A.; Cliffel, D. E. *Journal of Electroanalytical Chemistry* **2006**, *587*, 333-339.
(46) Eklund, S. E.; Taylor, D.; Kozlov, E.; Prokop, A.; Cliffel, D. E. *Analytical Chemistry* **2004**, *76*, 519-527.
(47) Snider, R. M.; Ciobanu, M.; Rue, A. E.; Cliffel, D. E. *Anal. Chim. Acta.* **2008**, *609*, 44-52.

(48) Sekine, N.; Cirulli, V.; Regazzi, R.; Brown, L. J.; Gine, E.; Tamarit-Rodriguez, J.; Girotti, M.; Marie, S.; MacDonald, M. J.; Wollheim, C. B.; Rutter, G. A. *J. Biol. Chem.* **1198**, *289*, 4895-4902.
(49) Bard, A. J.; Fan, F. R. F.; Kwak, J.; Lev, O. *Anal. Chem.* **1989**, *61(2)*, 132-138.
(50) Bard, A. J.; Fan, F. R. F.; Mirkin, M. V. In *Electroanalytical Chemistry*; Marcel Dekker, Inc.: New York, 1994; Vol. 18, pp 243-373.
(51) Bard, A. J.; Fan, F. R. F.; Pierce, D. T.; Unwin, P. R.; Wipf, D. O.; Zhou, F. *Science* **1991**, *254(5028)*, 68-74.
(52) Bard, A. J.; Mirkin, M. V. *Scanning Electrochemical Microscopy*; Marcel Dekker, Inc.: New York, 2001.
(53) Pitta Bauermann, L.; Schuhmann, W.; Schulte, A. *Physical Chemistry Chemical Physics* **2004**, *6*, 4003-4008.
(54) Sanchez-Sanchez, C. M.; Rodriguez-Lopez, J.; Bard, A. J. *Analytical Chemistry (Washington, DC, United States)* **2008**, *80*, 3254-3260.
(55) Roberts, W. S.; Lonsdale, D. J.; Griffiths, J.; Higson, S. P. J. *Biosensors & Bioelectronics* **2007**, *23*, 301-318.
(56) Liu, B.; Cheng, W.; Rotenberg, S. A.; Mirkin, M. V. *J. Electroanal. Chem.* **2001**, *500*, 590-597.
(57) Cai, C.; Liu, B.; Mirkin, M. V.; Frank, H. A.; Rusling, J. F. *Anal. Chem.* **2002**, *74*, 114-119.
(58) Liu, B.; Rotenberg, S. A.; Mirkin, M. V. *Anal. Chem.* **2002**, *74*, 6340-6348.
(59) Feng, W.; Rotenberg, S. A.; Mirkin, M. V. *Anal. Chem.* **2003**, *75*, 4148-4154.
(60) Liu, B.; Rotenberg, S. A.; Mirkin, M. V. *Proc. Natl. Acad. Sci. U.S.A.* **2000**, *97(18)*, 9855-9860.
(61) Nishizawa, M.; Takoh, K.; Matsue, T. *Langmuir* **2002**, *18(9)*, 3645-3649.
(62) Takii, Y.; Takoh, K.; Nishizawa, M.; Matsue, T. *Electrochim. Acta* **2003**, *48*, 3381-3385.
(63) Yasukawa, T.; Kaya, T.; Matsue, T. *Electroanalysis* **2000**, *12(9)*, 653-659.
(64) Liebetrau, J. M.; Miller, H. M.; Baur, J. E.; Takacs, S. A.; Anupunpisit, V.; Garris, P. A.; Wipf, D. O. *Anal. Chem.* **2003**, *75*, 563-571.
(65) Hengstenberg, A.; Blochl, A.; Dietzel, I. D.; Schuhmann, W. *Angew. Chem., Int. Ed. Engl.* **2001**, *40(5)*, 905-908.
(66) Isik, S.; Schuhmann, W. *Angew. Chem., Int. Ed. Engl.* **2006**, *45(44)*, 7451-7454.
(67) Bard, A. J.; Li, X.; Zhan, W. *Biosens. Bioelectron.* **2006**, *22(4)*, 461-472.
(68) Mauzeroll, J.; Bard, A. J.; Owhadian, O.; Monks, T. J. *Proc. Natl. Acad. Sci. U.S.A.* **2004**, *101(51)*, 17582-17587.
(69) Dujardin, E.; Ebbesen, T. W.; Krishnan, A.; Tracy, M. M. J. *Adv. Mater.* **1998**, *10*, 611.
(70) Forouzan, F.; Bard, A. J.; Mirkin, M. V. *Isr. J. Chem.* **1997**, *37*, 155-163.
(71) Brissova, M.; Fowler, M.; Wiebe, P.; Shostak, A.; Shiota, M.; Radhika, A.; Lin, P. C.; Gannon, M.; Powers, A. C. *Diabetes* **2004**, *53*, 1318-1325.
(72) Chen, N.; Liu, L.; Zhang, Y.; Ginsberg, H. N.; Yu, Y.-H. *Diabetes* **2005**, *54*, 3379.
(73) Dong, F.; Fang, C. X.; Yang, X.; Zhang, F. L.; Lopez, J. R. *Diabetologia* **2006**, *49*, 1421.
(74) Fang, C. X.; Dong, F.; Ren, B. H.; Epstein, P. N.; Ren, J. *Diabetologia* **2005**, *48*, 2412-2421.
(75) Remedi, M. S.; Rocheleau, J. V.; Tong, A.; Patton, B. L.; McDaniel, M. L.; Piston, D. W.; Koster, J. C.; Nichols, C. G. *Diabetologia* **2006**, *49*, 2368-2378.
(76) Wilburn, J. P.; Wright, D. W.; Cliffel, D. E. *Analyst* **2006**, *131*, 311-316.
(77) Cabrera, O.; Berman, D. M.; Kenyon, N. S.; Ricordi, C.; Berggren, P.-O.; Caicedo, A. *Proceedings of the National Academy of Sciences of the United States of America* **2006**, *103*, 2334-2339.
(78) Wong, H. Y.; Ahren, B.; Lips, C. J. M.; Hoppener, J. W. M.; Sundler, F. *Regulatory Peptides* **2003**, *113*, 89-94.

CHAPTER V

SINGLE CELL METABOLIC ANALYSES BY SCANNING ELECTROCHEMICAL MICROSCOPY*

Introduction

The past decade has witnessed a growth in the application of biosensors to micron and submicron level investigations in a wide variety of disciplines. Rapid development, both in miniaturization techniques and in understanding of biological processes, has accelerated the expansion of biosensors in clinical applications and in areas such as biology, neurobiology, pharmacology, and tissue engineering.[1,2] In this respect, researchers have been able to acquire real-time quantitative measurements through the application of micro-sensors on living cells, both in vitro and in vivo.[2-4]

Of particular interest are the enzyme-based sensors because they offer the selectivity toward a single analyte optimized by natural evolution. Enzymes achieve molecular recognition of substrates (i.e., analytes of interest) based on structural complementarity, leaving little room for error.[5] Enzymes catalyze with high specificity chemical reactions in biological systems according to Equation 5.1:

$$\text{substrate} + \text{cofactor} \xrightarrow{enzyme} \text{products} \qquad (5.1)$$

Enzymes have been successfully employed in the miniaturization of sensor designs, including one of the most important sensors for the health industry that emerged decades ago: the glucose sensor which is based on glucose oxidase (GOx), whether it is intended for in vivo monitoring of

---

*This chapter was previously published as : "*Glucose and lactate biosensors for scanning electrochemical microscopy imaging of single live cells*," Ciobanu, M.; Taylor, D. E.; Wilburn, J. P. and Cliffel, D. E. *Anal. Chem.* **2008**, *80*, 2717-2727.

glucose levels,[6] or for a diabetic's regular glucose meter for use at home. BesidesGOx, there have been numerous other enzymes used for the development of miniaturized amperometric sensors, such as sarcosine oxidase,[7] galactose oxidase,[7] hexokinase,[8] choline oxidase,[7] lactate oxidase (LOx),[9] alcohol oxidase,[7] horseradish peroxidase,[10] cholesterol oxidase,[11,12] etc. In addition to their importance for diabetes patients and in vivo studies, enzyme-based amperometric sensors are irreplaceable tools for the non-invasive study of the metabolism at the cellular level. A simplified view of the metabolic processes at the single cell level is presented in Fig. 5.1, indicating that information about the way a cell performs glycolysis could be acquired by using enzyme-based sensors for glucose and lactate. We have already employed GOx and LOx based sensors for probing cellular metabolism in a multianalyte microphysiometer

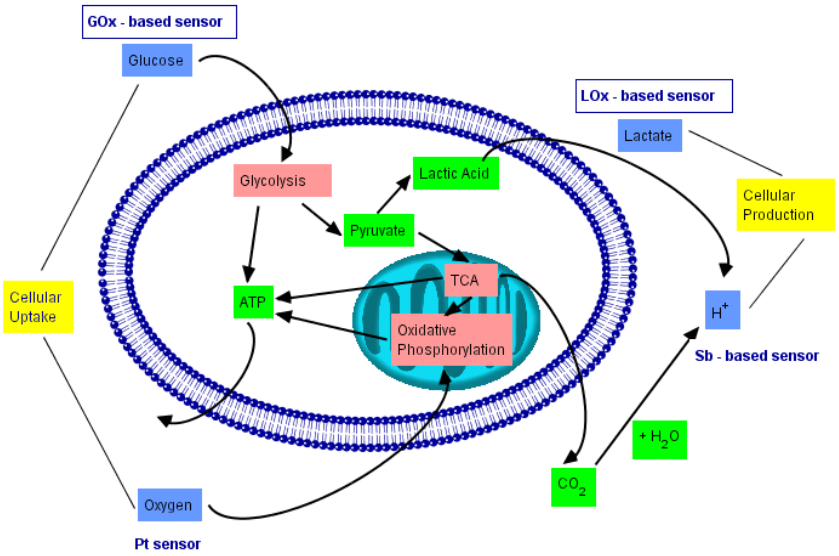

Figure 5.1; Cancer cell metabolic pathways suitable for electrochemical probing by SECM. Cancer cells have an altered metabolism compared to normal cells, with glycolysis being one of the affected pathways. TCA = tricarboxylic acid cycle.

(MAMP).[13-16] Our laboratory has modified the Cytosensor™ microphysiometer (originally developed by Molecular Devices for the measurement of acidification rates) into the MAMP to allow for simultaneously recording four analytes: glucose and oxygen uptake, lactate production and extracellular acidification rates for large numbers (> 10^5) of cells. The MAMP proves a

useful tool in studies such as the response of various cell types to chemical agents and toxins with ramifications in biodefense studies;[15] cancer cellular metabolism relating genetic mutations to different metabolic phenotypes, with implications in mathematical modeling of cancer.[17,18] The MAMP yields metabolic rates (e.g., lactate production rate) for large number of cells, but has no ability to assess cell to cell variability. This paper is not a study of the variability of metabolic rates from one single cell to another, but rather it presents the technical means that could be employed for addressing this problem by opening up the range of analytes for single cell electrochemistry.

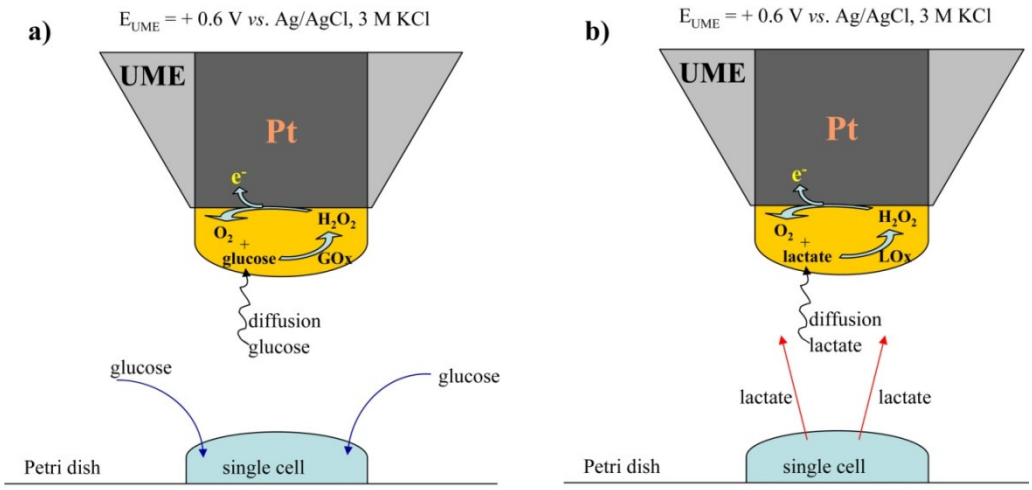

Figure 5.2; Enzyme-based UME biosensor. Enzyme layer (GOx (a) or LOx (b)) is deposited onto 25 µm Pt UME by either electropolymerization or casting. The tip is rastered across the cell adhered to a Petri dish: a) in the case of GOx it senses extracellular glucose depletion due to cellular uptake; b) in the case of LOx it senses lactate production by the cell. The enzyme film breaks down the analyte, and the resulting H_2O_2 is oxidized at the underlying Pt UME. The arrows entering the cell symbolize glucose uptake (a), while the arrows exiting the single cell denote lactate production (b).

The glucose and lactate amperometric sensors are based on a Pt electrode that is in contact with a polymer containing the specific enzyme (Fig. 5.2); glucose and lactate are measured indirectly at the electrode surface by amperometric oxidation of hydrogen peroxide. The hydrogen peroxide is formed in aqueous environments during the reaction catalyzed by the enzyme entrapped in the matrix (e.g., GOx in Fig. 5.2a or LOx in Fig. 5.2b) with the analyte of

interest (i.e., glucose for Fig. 5.2a or lactate for Fig. 5.2b) in aerobic conditions, as described by Equations 5.2 and 5.3:

$$\text{D-glucose} + \text{oxygen} \xrightarrow{GOx} \text{D-gluconolactone} + \text{hydrogen peroxide} \quad (5.2)$$

$$\text{L-lactate} + \text{oxygen} \xrightarrow{LOx} \text{pyruvate} + \text{hydrogen peroxide} \quad (5.3)$$

Horrocks et al.[10] have used an enzyme (horseradish peroxidase) UME in conjunction with the scanning electrochemical microscopy (SECM) for the measurement of H_2O_2 at surfaces. They do not present any amperometric approach curves (ACs), but rather conductance-distance curves. The conductance measurements have the advantage of being insensitive to the enzyme-polymer layer present on the tip, however, they have to be performed in solutions of very low conductivity (1 mM KCl) which makes them unsuitable for physiological applications, such as approaching and imaging in biological buffers (e.g., RPMI). Kueng et al.[8] have also reported the use of an enzyme UME for SECM; they have assembled a Pt dual microdisk electrode with one 5 μm Pt for electrode positioning via ACs and with the other 5 μm Pt modified through electropolymerization with both GOx and hexokinase for indirect imaging of ATP transport through a porous polycarbonate membrane. However, they have not used the enzyme sensor of this dual UME for either approaching the surface nor for imaging of live organisms. Acquiring ACs using the electrochemical process that takes place at an enzyme modified tip would remove the need in this case for manufacturing the more complicated dual UME. Kueng et al.[19] have also used an enzyme (GOx) coated tip integrated in an AFM-SECM setup for imaging glucose transport through a porous membrane; in this case they bypassed the need for ACs by using the AFM tip.

SECM[20-23] can be developed as a useful technique for the study of cell metabolic fluxes (as an important component of metabolomics), since it can map electrochemical activity across the entire surface of a single cell, and can record dynamic changes. Although SECM has been used over the years for investigating biological systems,[23,24] only recently has attention been

given to SECM for single cell studies.[25-38] Mirkin et al.[26,27,32-34] have investigated single cells by SECM in order to determine various redox activities across different types of cells, examining the differences between nonmetastatic and metastatic human breast cells. They have identified series of redox mediators that can cross the cell membrane, investigated their distribution between cytosol and nucleus, and found them unable to penetrate the nuclear envelope. Matsue et al.[36-38] studied single cell topography and paid particular attention to respiration studies by means of SECM for cells such as protoplasts and PC12. Wipf et al.[31] have used SECM to monitor the real-time morphological changes in PC12 cells that are used as model neurons. Baur et al.[30] have used a constant distance SECM for a study of PC12 cells where they showed that constant impedance imaging yields superior topographic images of single cells compared to more common constant height SECM. Schuhmann et al.[28] recorded topographic images of PC12 cells by SECM, and studied catecholamine release from PC12 cells, using SECM as a positioning tool for an amperometric sensor in the vicinity of the cells. Isik and Schuhmann[29] have detected the release of nitric oxide from single T-HUVEC cells by also using a constant distance SECM. Bard et al. have used SECM to study the metabolism of menadione to thiodione in single hepatoblastomas,[35] and have probed the activity of HeLa cells using the oxidation of a ferrocene derivative.[25]

Our choice of using the constant height SECM versus the constant distance SECM for the study of single cell metabolism was predicated on using a chemically modified tip (i.e., Pt UME coated with an enzyme-containing polymer); the modified tips can be integrated easier with the typical constant height SECM mode of operation. The major ways of achieving the constant distance mode in SECM are all relatively limited for the distance signal possibilities, due to their intrinsic design. One possibility for the constant distance mode is the use of the impedance SECM,[39] which is based on acquiring data based on high frequency capacitance measurements. The capacitance of the chemically modified tips would be dramatically affected by the presence of the polymer layer entrapping the enzymes on the Pt UME, compared to bare metal tips. Another way of achieving the constant distance mode for SECM measurements is by using shear

force.[40] Hengstenberg et al. have shown that enzyme-filled capillaries can be used as tips for scanning using a shear force based constant distance SECM mode;[41] however, these tips are not amperometric and are suited to generation-collection modes, not imaging. The application of a polymer film to the tip for shear force based SECM applications appears technically challenging because the mass loading of the enzyme film will reduce the resonant Q of the oscillating tip in addition to the hydrodynamic loss in Q from a large volume of solution above the cells. Another mode of operation for the SECM would be the AFM-SECM.[42] While Kueng et al. reported a GOx-coated AFM tip,[19] the use of AFM-SECM for scanning live cells has yet to be developed into a practicable method, and the difficulty of making each tip by FIB micromachining is considerable. The integration of polymer film-modified tips for use in conjunction with a constant distance SECM for the study of live cell metabolism will be the subject of future studies. With the typical UME sizes of 5-25 μm used in our work, the higher resolution possible by constant distance control would not be significant, justifying our use of constant height imaging.

A single cell is the basic structural and functional unit of all organisms. While the MAMP provides information about the metabolism of cells, it averages signals over large populations (> 10^5 cells) and cannot distinguish differences between individual cells. One cannot develop a deep understanding of metabolomics unless the processes are explored in the context of the individual cell level, wherein multiple biochemical processes, distributed throughout the cell and various cell compartments, are integrated into a functional system. Differences in the average rate of glycolysis between large numbers of cancerous and healthy cells have been demonstrated,[43,44] making spatio-temporal mapping of glycolytic analytes (e.g., pH, lactate, oxygen, glucose) an area of great interest. The intracellular pH for both cancerous and normal cells is approximately 7.4,[45] and the extracellular pH for cancerous growths is acidic, with values as low as 6.7.[46] This increased acidity in tumors is a result of the Warburg effect,[44] i.e., enhanced glycolysis, which under hypoxic conditions leads to an increased lactate production that in turn lowers the extracellular pH (see Fig. 5.1). Walenta et al.[47] reported mean lactate concentrations in

head and neck tumours of ~ 12 μmol/g, as compared to similar normal tissue lactate concentrations of ~ 5 μmol/g. Acidity profiles[32] were previously studied by SECM for single living cells; however, the recording of these pH profiles presents certain technical difficulties, such as the use of an additional potentiostat in conjunction with the SECM, as the pH sensor (Sb-based in Liu et al.'s paper)[32] is by definition potentiometric. Using the lactate production to characterize cancer cells presents its own advantages, such as the use of an amperometric sensor for lactate sensing, the ability to record lactate profiles in highly buffered solutions (as most cell culture media are) as opposed to a pH potentiometric sensor that can be used solely in a modified low buffered medium. Lactate production profiles could also provide information that could lead to a deconvolution of the pH profiles of cancerous cells.

Cell respiration[37] was also previously studied by SECM for single living cells; however, to our knowledge, there have been no reported glucose or lactate spatio-temporal profiles for single live cells. We present in this paper the manufacturing and characterization of glucose and lactate ultramicroelectrode biosensors for SECM of single live cells, and demonstrate that the GOx-based sensors can be used for the positioning of the UME in the vicinity of the cell, as well as for the imaging of the cell, and also show that the LOx-based sensors can be used for recording of lactate release profiles from single cells.

Experimental

Materials

The materials were purchased as follows: $MgCl_2 \cdot 6H_2O$, $NaH_2PO_4 \cdot H_2O$, HCl, $CaCl_2$, $MgSO_4$, NaCl, KCl, KH_2PO_4, $NaHCO_3$, L-lactic acid, sodium acetate trihydrate, 35 mm Petri dishes and 50 mM phosphate buffer pH 7.0 from Fisher Scientific; KPF_6 from Aldrich Chemical; glutaric dialdehyde as 25% solution in water (GDA) and 2-aminophenol (OAP) from Acros; $Na_2HPO_4 \cdot 7H_2O$, bovine serum albumin (BSA), RPMI 1640, D-glucose, GOx, type II-S from

Aspergillus niger and LOx from *Pediococcus* species from Sigma; H_2SO_4 and NaOH from EM Science; ethanol (absolute proof) from Aaper; ferrocenylmethyltrimethylammonium iodide from Strem Chemicals; N_2 from Gibbs Welding Supply; conductive silver epoxy from Epoxy Technology; white sealant Hysol Epoxi-Patch from Dexter Corporation; 35 mm glass bottom Petri dishes from Bioscience Tools. All materials were used as received unless otherwise specified.

ASTM Type I (18 MΩ) analytical grade deionized water (DI) was obtained with a Solution 2000 Water Purification System from Solution Consultants. All solutions were filtered prior to use with 0.2 μm syringe filters from Fisher. Ferrocenylmethyltrimethylammonium hexafluorophosphate (FcTMA) was prepared according to the method of Mirkin and co-workers.[48] All reported potentials were measured against a commercial Ag/AgCl, 3 M KCl reference electrode (RE, model CHI111, CH Instruments).

SECM of unmodified UMEs

All SECM measurements were conducted with a CHI900 instrument from CH Instruments equipped with an adjustable stage for tilt correction. The electrochemical cell was in a typical four-electrode configuration for testing the UMEs: UME tip electrode (working electrode, WE), Pt wire counter electrode (CTR), Ag/AgCl, 3 M KCl (RE), and substrate electrode (SE), which was a 2 mm Pt disk (CHI303). All UMEs were manufactured with 5 or 25 μm Pt wire from Goodfellow according to Bard et al.,[21] polished with 0.05 μm alumina from Buehler, and sonicated in ethanol and water. UMEs were electrochemically cleaned for 5 min in 0.5 M H_2SO_4 using a CHI660a potentiostat, and were tested with 1 mM FcTMA in 100 mM KCl for performance. The Pt SE was polished and cleaned in an identical manner to the UMEs. Only UMEs capable of achieving $I_T = 8$ (e.g., 800% increase in current over steady-state conditions far from the SE)[23] during approach to the Pt SE were used in biosensor construction. The UMEs

were also characterized by cyclic voltammetry (CV), and consistently yielded the expected sigmoidal CV. The UMEs used had RG ratios[21] of ~ 5 for the 5 μm Pt tips (7 μm actual measured diameter) and ~ 2 for the 25 μm Pt tips.

Enzyme-modified UMEs

a. Manufacturing.

The enzyme-containing polymer layer was deposited onto 25 μm Pt UMEs via two distinct methods: (i) Electropolymerization – the enzyme was deposited on the electrode in a similar manner as described by Zhang et al.[49] The enzyme (10 mg/mL for GOx and 2 mg/mL for LOx) and the OAP (0.8 mg/mL) were dissolved in 50 mM acetate buffer, pH 5.9, the solution was degassed (N_2), and the electrodeposition occurred under stirring at E = +0.65 V vs. Ag/AgCl, 3 M KCl for 1 hour (CHI660a workstation equipped with a Faraday cage); the electrodes were allowed to dry for another hour, were then briefly rinsed with DI and stored at 4 ^{o}C in 50 mM phosphate buffer until use. (ii) Casting – the enzyme (8 mg/mL for GOx and 10 mg/mL for LOx), GDA (14 μL/mL buffer) and BSA (62.5 mg/mL) were all dissolved in 50 mM phosphate buffer, pH 7.0;[16] the enzyme solution was then hand-cast onto the surface of the UME by briefly touching the tip of the UME to a tiny droplet of enzyme solution; the UMEs were air dried and stored at room temperature until further use.

b. Calibration

The performance of the biosensor UMEs was tested using a CHI660a potentiostat with a three electrode configuration: WE – enzyme UME; RE - Ag/AgCl, 3 M KCl; CE – Pt mesh. Current vs. time curves were recorded under moderate stirring at E = + 0.6 V vs. Ag/AgCl, 3 M KCl (for both GOx and LOx). Standard additions were made from stock solutions of 500 mM glucose and 100 mM lactate. To ensure the validity of the results, the calibrations were performed before and after the use of the biosensor UMEs in conjunction with the SECM.

SECM approach curves of biosensor UMEs

ACs were acquired for GOx and LOx UMEs in a three-electrode system: WE – biosensor 25 μm UME; RE - Ag/AgCl, 3 M KCl; CE – Pt mesh. The tip was approached to the substrate (35 mm Petri dish) and allowed to touch it. Glucose solutions of 1.0-5.0 mM and lactate solutions of 0.5 mM were used in the approach experiments.

Cell culture

Fibroblasts (mouse fibroblast CRL-10225) were cultured in high glucose (4.5 g/L) DMEM (Dulbeco's modified Eagle's medium) with 4 mM L-glutamine, supplemented with 10 % fetal bovine serum and 1.0 mM sodium pyruvate. MCF10CA1a cells[50] were cultured in DMEM/F12 medium, supplemented with cholera toxin (0.1 μg/mL), insulin (10 μg/mL), hydrocortisone (0.5 μg/mL), epidermal growth factor (20 ng/mL) and horse serum (5 %). PC12 cells (CRL-1721) were cultured in Ham's F12K medium with 2 mM L-glutamine adjusted to contain 1.5 g/L sodium bicarbonate (82.5 %), horse serum (15 %), and fetal bovine serum (2.5 %); PC12 cells were plated on dishes treated with human collagen (type IV).

SECM imaging

The SECM was used in conjunction with an inverted microscope (VistaVision, VWR) equipped with a stage and objective warmer (TCII, 2Ch micro temperature controller, Bioscience Tools). The inverted microscope allowed for visually monitoring the morphology of the cells to be scanned. The SECM tip holder was extended above the microscope objective with the aid of a light but sturdy aluminum piece. For positioning, the UMEs were approached to the dish and then withdrawn a known distance. The data were recorded in a three-electrode system: WE – UME; RE - Ag/AgCl, 3 M KCl; CE – Pt mesh, in the constant height mode.

a. Glucose profiles.

The 25 μm UME GOx biosensors were positioned near the cell to be imaged, and then the biosensor tip was rastered across the surface above the cell while the tip was maintained at E = + 0.6 V vs. Ag/AgCl, 3 M KCl. The buffer used was Hank's balanced salt solution (HBSS), pH 7.4, 5 mM glucose and no phenol red.

b. Lactate profiles

The 25 μm UME LOx biosensors were positioned near the cell to be imaged, and then the biosensor tip was rastered across the surface above the cell while the tip was maintained at E = + 0.6 V vs. Ag/AgCl, 3 M KCl. The buffer used was RPMI, pH 7.4; there was no lactate added/present in the solution. There are possible interfering analytes secreted by the cells (e.g., peroxide, dopamine, etc.) that would be active at the potential set for the UME biosensor. However, the types of sensors we are using are enzyme-based, and the polymer films are highly selective, as the polymer helps to block interferents. We have extensively tested the use of the sensors in the presence of live cells in the MAMP and found no analyte detection problems due to cross-interferents at this potential.[14-16]

c. Oxygen profiles

The buffer used was HBSS, pH 7.4, with 5 mM glucose and 1 mM FcTMA. The Pt 7 μm UME was used for recording topographical images first, with the tip potential E = + 0.6 V vs. Ag/AgCl, 3 M KCl, ensuring the oxidation of the FcTMA. We chose FcTMA as mediator for topography imaging of single cells based on previous work in our lab showing that this particular redox mediator does not cross bilayer lipid membranes (BLMs),[51] i.e., it yields a negative feedback when the UME approaches the BLM. Once the SECM topography information was acquired, the tip potential was switched to E = - 0.5 V vs. Ag/AgCl, 3 M KCl, ensuring the reduction of the oxygen present in the solution, thus yielding oxygen uptake profiles.

Results and Discussion

We have manufactured GOx enzyme UME biosensors by employing two methods: electropolymerization and hand casting. We have tested the properties of the enzyme films deposited onto the Pt UMEs by doing amperometric calibrations prior to any SECM applications. Figure 5.3a displays a typical example of a calibration toward the analyte of interest (i.e., glucose) of an electropolymerized GOx UME biosensor. The sensor displays linear sensitivity to glucose for concentrations of up to 18 mM, and there is no response to blank additions (buffer, no glucose). In order to find the "zero distance point" on the AC, the sensors were allowed to approach until they physically touched the substrate surface. In order to determine whether the procedure adversely affected performance, after the SECM experiments the sensors were tested again for sensitivity with respect to their analyte. Figure 5.3b shows an example of amperometric calibration for a GOx UME sensor after use in conjunction with SECM for recording ACs. The sensor UME continues to display linear sensitivity to glucose for concentrations of up to 18 mM, and there is no response to the blank additions. Comparatively, the cast GOx UME biosensors display a narrower linear sensitivity range, for glucose concentration of up to 14 mM. Figure 5.3c presents the stability of an electropolymerized GOx UME sensor in time. The data points in Figure 5.3c have been obtained from amperometric calibration curves similar to the ones presented in Figures 5.3a and 5.3b. Figure 5.3c displays one measurement (data point) for each day for each concentration represented on the graph. The electrode was stored in the refrigerator in 50 mM phosphate buffer pH 7 between runs. There is little difference between the calibrations done over the course of 12 days, and this minute variation is not important in the context of the fact that the electrodes should always be calibrated the day of the measurements. The electropolymerized GOx sensors (if stored at 4 °C in buffer) preserve their sensitivity toward glucose for periods of time for up to 1 month. In contrast, the cast 25 μm GOx sensors (stored at

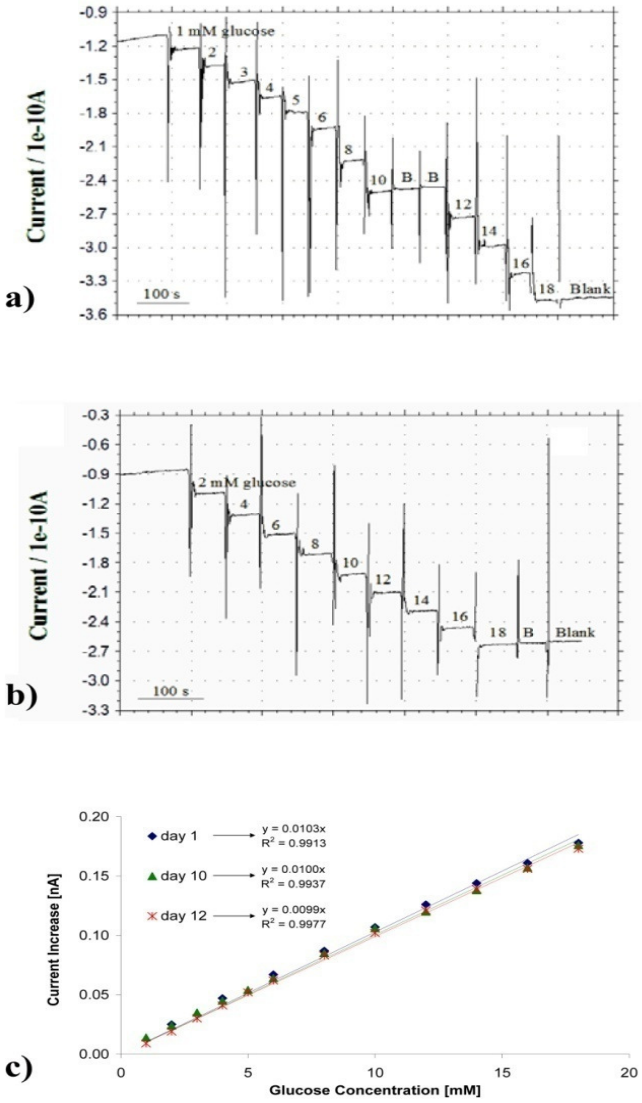

Figure 5.3; Amperometric calibrations of electro-polymerized GOx 25 µm UME biosensors, E = + 0.6 *vs*. Ag/AgCl, 3 M KCl; additions up to 18 mM glucose in 50 mM phosphate buffer, pH 7: a) GOx UME sensors exhibit sensitivity to glucose prior to SECM experiments; b) the sensors preserve the sensitivity to their analyte after being employed in extensive SECM experiments; c) the electropolymerized GOx biosensors are stable in time when stored in 50 mM phosphate buffer, pH 7 at 4 ^{o}C for periods of at least two weeks; same sensor shows almost identical sensitivity after 1, 10 and 12 days from electropolymerization date. The data presented in this figure is for three distinct electropolymerized GOx sensors (one sensor for the data in (a), one sensor for the data in (b), and another sensor for the data in (c)).

room temperature, no buffer) start to lose sensitivity to glucose after 2-3 days. Different storage conditions have been explored for all types of sensors presented in this paper, and the optimum ones for each sensor type are the only ones discussed here (dry storage at room temperature for hand-cast biosensors, and 4 °C in buffer for electropolymerized biosensors). One advantage that

the cast GOx sensors have over the similar electropolymerized ones is the more facile manufacturing procedure, which renders the films applied on the 25 µm Pt UME as 'disposable.' The overall success rate for production of sensors (determined by whether sensors exhibited sensitivity toward their analyte the same day as manufacturing) was ~ 70 % for the electropolymerization process and ~ 90 % for the casting method (we have tested at least 20 electrodes for each method).

The lactate sensor production is complicated by the relatively lower stability of LOx as compared to GOx. Fig. 5.4 compares the behavior of electropolymerized and cast LOx UME

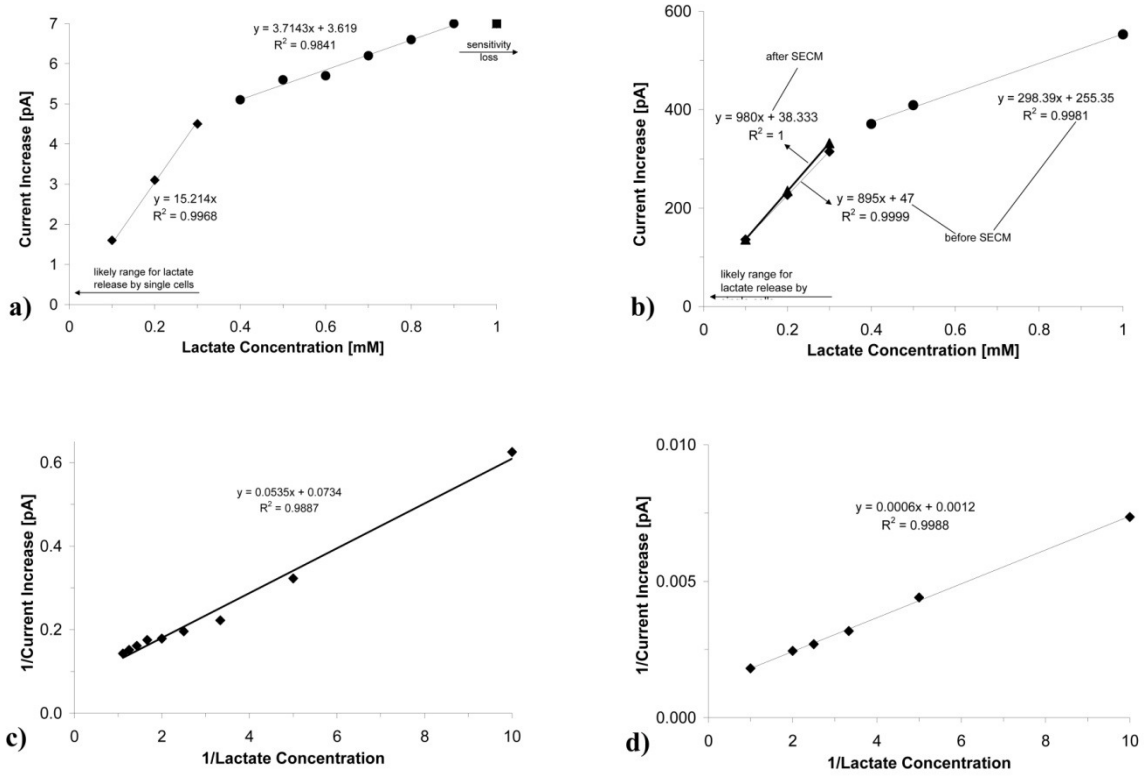

Figure 5.4; Amperometric calibrations of a) electropolymerized and b) cast LOx 25 µm UME biosensors, E = + 0.6 *vs*. Ag/AgCl, 3 M KCl; additions up to 1 mM lactate in 50 mM phosphate buffer, pH 7. The sensors were calibrated for concentrations of up to 1 mM lactate, and display two distinct linear regions: below 0.3 mM and above 0.4 mM, with the expected cellular lactate release range below 0.3 mM. The sensors retain lactate sensitivity upon being used in SECM experiments. Double reciprocal plot representations of these amperometric calibrations: c) the electropolymerized LOx sensor for which the corresponding data is shown in a); and d) cast LOx sensor for which the corresponding data is shown in b) – before use in SECM.

sensors. For both types of LOx-based sensors, the calibration plots seem to exhibit two distinct linear ranges: 0.1 – 0.3 mM that covers the likely physiological range for single cell release, and 0.4 – 0.9/1.0 mM lactate, which may be useful for future studies (e.g., scanning across surfaces with patterned LOx, in the presence of lactate in solution). Horrocks and co-workers[10] have observed the same type of dual range when they calibrated a horseradish peroxidase-modified UME with respect to H_2O_2 sensitivity; they have proposed that this decay in sensitivity was due to the redox process in parts of the polymer in poor contact with the UME element (carbon fiber in their case). The electropolymerized LOx sensors generally lose sensitivity to lactate above 0.9 mM lactate (Figure 5.4a). However, these UME sensors are assembled with the help of oxidases, and as such they should obey the enzyme kinetics laws. For enzymes following the Michaelis-Menten behavior, one should look at the Lineweaver-Burk double reciprocal plot, where the inverse of the reaction rate is directly proportional to the inverse of the substrate concentration[5] (e.g., lactate in our case). Since the reaction rate is directly proportional to the current,[52] we can plot the inverse of the current versus the inverse of the lactate concentration, for example, and if the plot is linear, then the enzyme follows the Michaelis-Menten kinetics. Figure 5.4c displays the data from Figure 5.4a in the form of the Lineweaver-Burk double reciprocal plot, and Figure 5.4d does the same thing for the data from Figure 5.4b (before SECM). Both plots appear linear, indicating that the presence of two distinct regions in Figures 5.4a and 5.4b are due to a saturation of the LOx enzyme with the lactate substrate, meaning that the enzymes follow the Michaelis-Menten kinetics. The R^2 values for the Lineweaver-Burk double reciprocal plots in both cases (Figures 5.4c and 5.4d) are higher than the R^2 values for the linear ranges corresponding to the higher concentrations (> 0.4 mM, Figures 5.4a and 5.4b), indicating that these films should be regarded as obeying the Michaelis-Menten behavior, rather than having two distinct linear regions as it was previously suggested.[10] Since the concentration of lactate production by cells is very low, the concentrations of produced lactate are contained in the lower regions (below

0.3 mM lactate), which are linear under the Michaelis-Menten behavior, and thus the enzyme saturation with the substrate does not hinder the detection for our purposes.

Just as for the GOx UME biosensors, we have tested the properties of the LOx sensors before and after the use in conjunction with the SECM, to validate the SECM results. Figure 4B displays examples of calibration plots for a cast LOx UME biosensor in the lower linear concentration range before and after recording ACs (where the tip was allowed to touch the Petri dish substrate in order to find the "zero distance point"), showing that sensitivity toward lactate is retained. While the electropolymerized LOx sensors are more reproducible, they have a lower life time (~ 24 h, stored at 4 ^{o}C in buffer) compared with the cast LOx sensors (2 days, room temperature). The manufacturing success rate is overall lower for the LOx sensors than for the GOx sensors: ~ 20 % for electropolymerized LOx and ~ 60 % for cast LOx sensors (we have tested at least 20 electrodes for each method). Just as in the case of the GOx sensors, the cast LOx sensors are easier to manufacture than the electropolymerized ones, and the cast LOx films can be regarded as 'disposable.'

As expected, for both types of sensors discussed in this paper, the electropolymerized ones were more reproducible than the cast ones. During the casting procedure it is difficult to control the exact amount of enzyme solution that gets deposited onto the Pt tip and/or the casting solution homogeneity (for electrodeposition the solution is stirred). However, individual sensor calibrations must be performed prior to use, making this less important. Figure 5.5 presents ACs for two distinct electropolymerized GOx UME sensors manufactured a few months apart (both tested the second day after manufacturing, approaching to plastic Petri dishes) and illustrates overall reproducibility of the electropolymerization manufacturing process. We can compare the ACs since we have the 'zero separation distance' for each curve, and currents have been normalized with respect to their steady-state current values. For the sensor #2 in Fig. 5.5a the

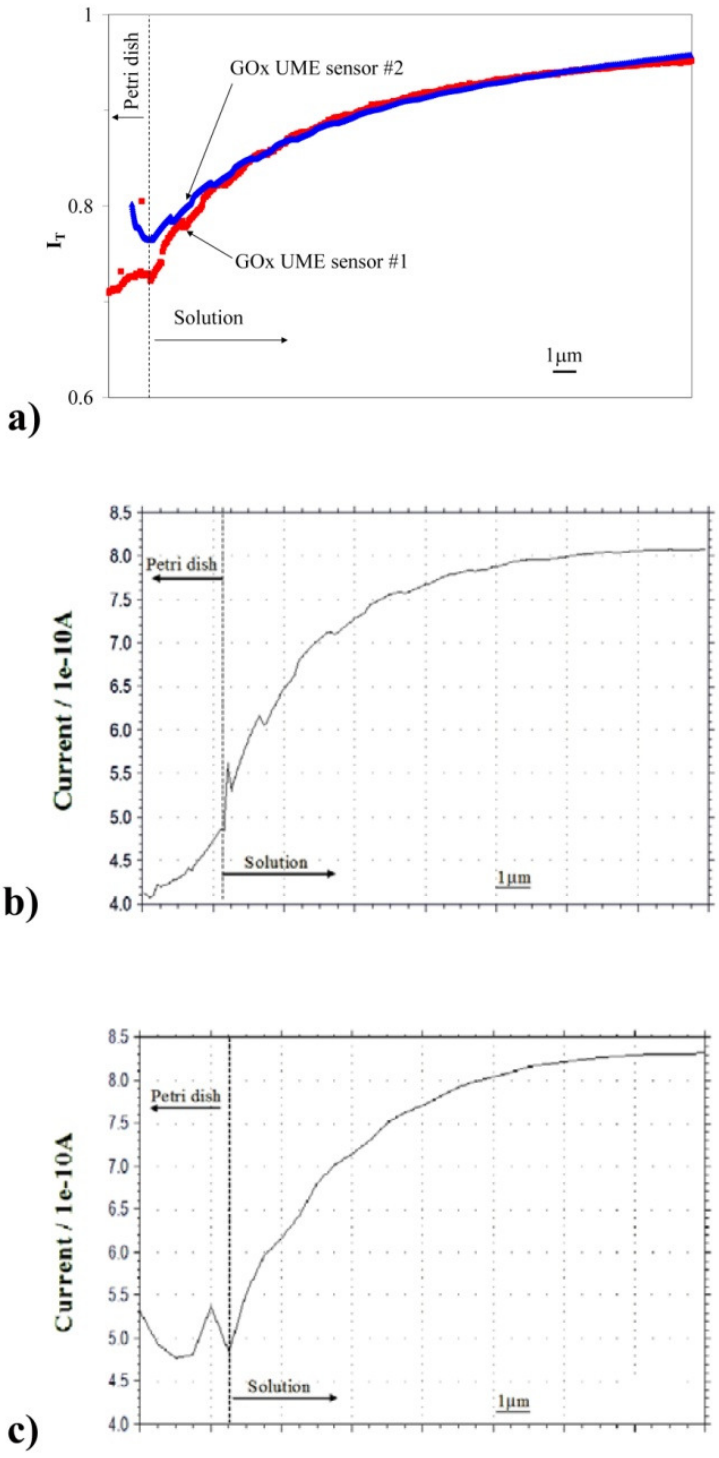

Figure 5.5; Approach curves for 25 µm UME enzyme-based biosensors; E = + 0.6 *vs*. Ag/AgCl, 3 M KCl; in 50 mM phosphate buffer, pH 7: a) GOx electropolymerized sensors #1 (approach speed 1.5 µm/s) and #2 (approach speed 3 µm/s) yielded similar curves in 5 mM glucose, indicating reproducibility; b) GOx cast sensor (5 mM glucose, approach speed 3 µm/s); c) LOx cast (0.5 mM lactate, approach speed 15 µm/s). In all plots the vertical dashed line represents the point where the UME tip touches the Petri dish, coming from the right side (solution side).

current increases upon the tip touching the substrate; this is probably due to a slight compression of the polymer layer which in turn could cause a sudden increase in the concentration of electroactive species at the Pt sensing element. Figures 5.5b and 5.5c display ACs for cast electrodes: GOx and LOx cast UME biosensors, respectively. For the case of GOx-based sensors the ACs can be used as means of positioning the tip at a known distance from the substrate when imaging live cells for example (since the solution contains glucose needed for cell viability). In the case of metabolic lactate imaging, there is insufficient lactate in the extracellular solution (e.g., produced by a single cell, since the solution has no added lactate) to allow an AC to be performed, although there might be other applications where the lactate approach curves might find use (e.g., study of LOx kinetics). Upon conducting an extensive review of the literature we were unable to find any published studies featuring ACs generated by enzyme electrodes, therefore Figure 5.5 presents the first amperometric ACs recorded with enzyme coated UMEs. The ACs for the enzyme-coated UMEs do not obey the classic SECM feedback theory, due to the presence of the polymer layer deposited on the Pt surface. The attempts of fitting the ACs to the simple kinetically limited (and/or mass transfer limited) feedback modes for SECM did not succeed either, pointing to the fact that the processes occurring at the tip are complex, and this opens the door to future studies for unfolding the intricacies of enzyme coupled electrode kinetics for these UME sensors.

We have used the ACs for the GOx UME sensors to position the tip at a certain distance (10 μm) from the glass bottom Petri dish on which fibroblasts were cultured at low density (2000 cells in the entire dish) to permit the imaging of a single fibroblast without interference from neighboring cells. We have used both the visual monitoring of the enzyme UME approaching the surface of the Petri dish with the help of the inverted microscope, and the ACs to find the point where the tip touches the substrate. The problem with only physically lowering the tip onto the surface of the substrate[37] is that the tip can be damaged in the process. By using the ACs in conjunction with the optical monitoring of the moving tip, we minimize the opportunities for

damaging the sensor. Upon establishing physical contact between the tip and the substrate, the tip is retracted the desired distance using the z-axis inchworm of the SECM setup, and consequently the tip-substrate separation distance that we report for the cell imaging is as accurate as the movement of the z-axis inchworm. While it is possible that the polymer layer would slightly adhere to the surface of the dish and the geometry of the enzyme film would be slightly disturbed in the retraction movement, our calibration experiments (see Figs. 5.3 and 5.4) clearly indicate that the analyte sensitivity of the UME biosensor is not altered upon recording ACs and gently touching the surface of the substrate. Upon positioning the UME biosensor at the desired distance above the Petri dish, the tip is rastered across the live cell while monitoring its movement through the optical microscope. Figure 5.6 shows the results of such an experiment, revealing a glucose uptake profile above a single fibroblast from a background solution containing 5 mM glucose. The current is the lowest on the top of the cell (as expected) and the uptake profile is uniform. The glucose uptake profile above a single fibroblast looks similar to the topography profiles of single fibroblasts. It is possible that the glucose uptake observed here is a combination of both diffusion/distribution profile of glucose around the fibroblast and

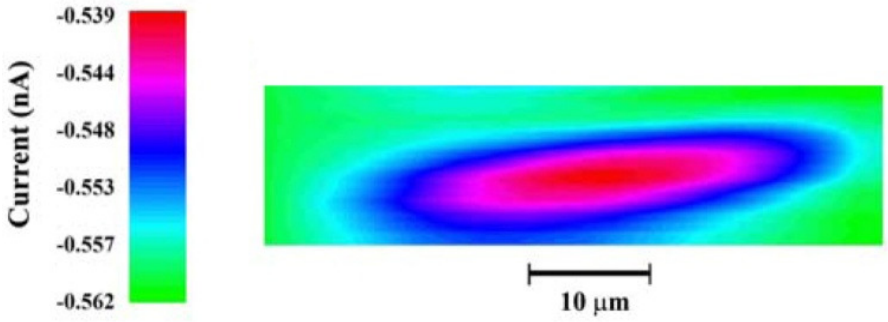

Figure 5.6; Glucose uptake profile for a single fibroblast. E = + 0.6 *vs*. Ag/AgCl, 3 M KCl; 5 mM glucose in HBSS, pH 7.4; scanning speed 15 µm/s; tip: GOx cast film on 25 µm UME biosensor; d = 10 µm from Petri dish; data have been corrected for background tilt in Origin Pro 7.5. The GOx cast 25 µm UME tip was positioned at 10 µm from the Petri dish by using approach curves.

nutrient uptake by the cell. Consequently, for the study of cell metabolism one should acquire glucose uptake images in conjunction with measuring the cellular production of an analyte, such as lactate.

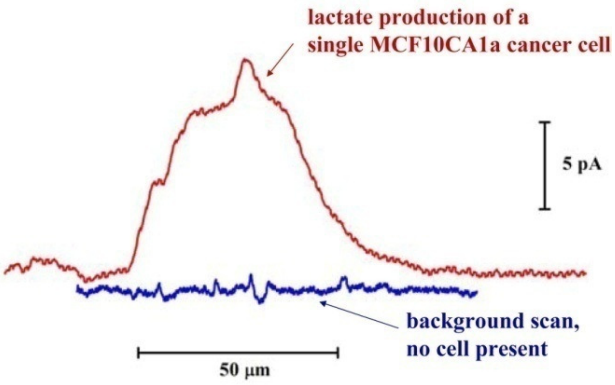

Figure 5.7; Lactate production from a single cancer cell MCF10CA1a. E = + 0.6 *vs*. Ag/AgCl, 3 M KCl; no lactate added in RPMI media, pH 7.4; scan speed 3 µm/s; tip: LOx cast film on 25 µm UME biosensor; red line: lactate production current associated with a single MCF10CA1a cancer cell; blue line: in the same Petri dish, same electrode, scan across surface when no cancer cells are present in the path of the electrode; data have been corrected for background tilt in Origin Pro 7.5.

One of the hallmarks of cancer cells is a lowered extracellular pH which is in part due to increased anaerobic respiration and lactate production by the cell (see Fig. 5.1). We have picked for this study an invasive cell line (MCF10CA1a) that forms tumors and metastasis in mice.[50] Figure 5.7 represents lactate production by a single MCF10CA1a cell, as sensed by a cast LOx 25 µm UME tip. The onset and falloff of current during the scan was observed (via the inverted microscope) to coincide with the period when the UME sensor was physically above the cell. The topography of the MCF10CA1a cells is hemispherical; however, because the lactate is produced by the cell (as opposed to being consumed, as in the case of glucose uptake), an increase in the lactate concentration above the cell is a consequence of cellular activity, and it cannot be mistaken for changes in cellular topography. The overlaid background curve was generated by repeating the scan, at the same tip-substrate separation, in a region of the dish where

no cells were present. We chose the control experiment of scanning above the bare surface of the Petri dish in order to prove that unless there is a source for the lactate (i.e., MCF10CA1a cell in our case), no current increase will be observed.

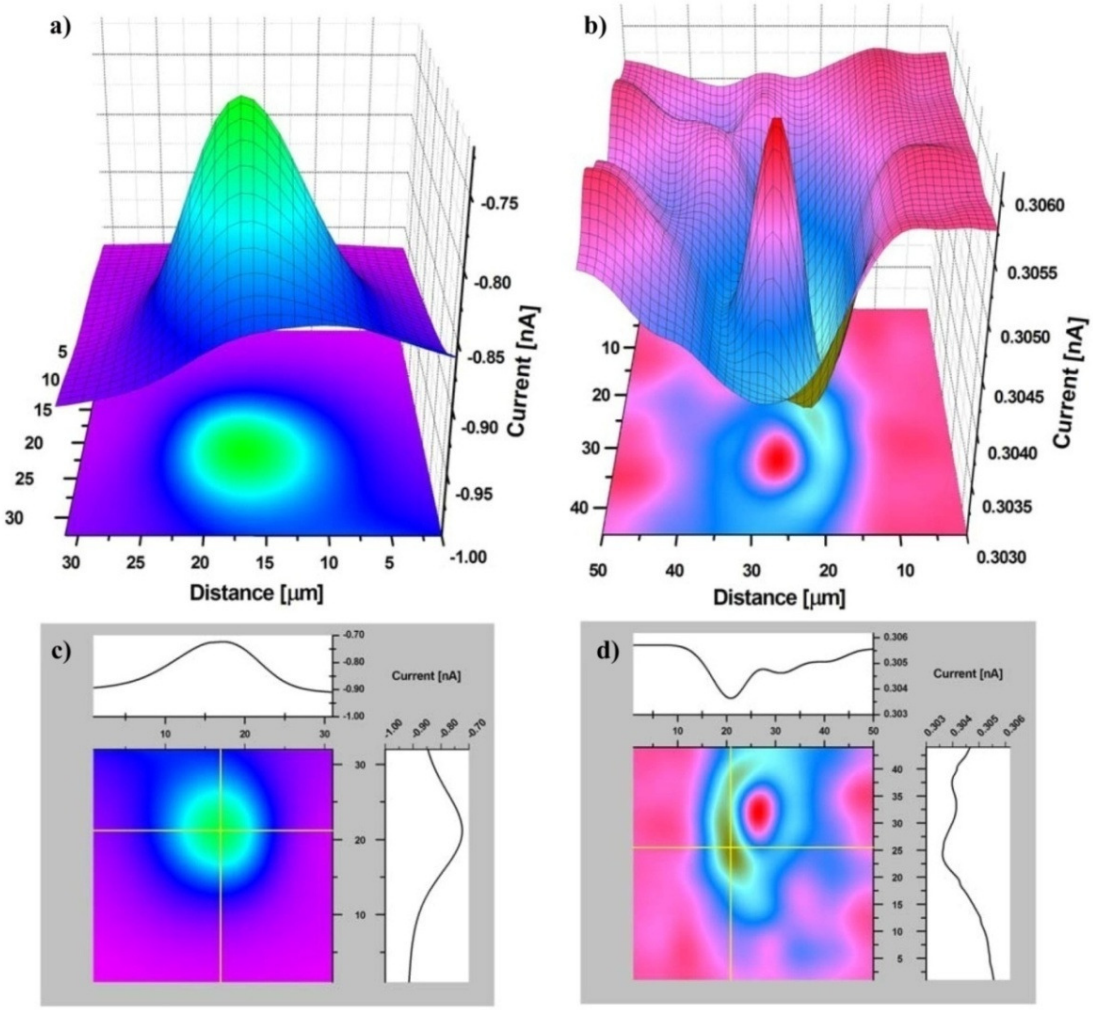

Figure 5.8; Topography (a and c) and oxygen uptake profile (b and d) of a single PC12 cell. E = + 0.6 vs. Ag/AgCl, 3 M KCl for topography and E = - 0.5 *vs*. Ag/AgCl, 3 M KCl for respiration; 1 mM FcTMA in Ringer's solution pH 7.4; tip: Pt 7 µm UME and scanning speed 30 µm/s for both images; data have been corrected for background tilt in Origin Pro 7.5. The tip was positioned by ACs to the insulating Petri dish surface: d ~ 10 µm from Petri dish for topography and d ~ 8 µm from Petri dish for respiration. (a) and (b) display the 3D contour plots for topography and respiration respectively. (c) and (d) are the same images from (a) and (b) with 'crosshairs' for easier comparison of the topography and respiration profiles: horizontal crosshair corresponds to the scan presented above the image; vertical crosshair corresponds to the scan presented on the right side of the image. All distances are in µm.

Cancer cells present enhanced aerobic glycolysis[44] and thus oxygen is an important analyte (see Fig. 5.1) that has to be accounted for when the metabolic profiling of cancerous cells is sought. We have recorded topographical images of PC12 cells in a medium containing FcTMA, with the potential of the 7 μm Pt UME tip set at E = + 0.6 vs. Ag/AgCl, 3 M KCl; at this potential the FcTMA present in solution gets oxidized at the Pt tip and a topography-type profile is observed, corresponding to the amount of FcTMA available for immediate diffusion to the tip, i.e., corresponding to the distance between the tip and the imaged object (PC12 cell in this case). An example of PC12 topography can be observed in Figure 5.8a, where the 3D contour plot for the FcTMA oxidation profile around the cell is presented. The shape of the cell appears uniform, as a hemispherical object. Upon obtaining information about the cell surface, we have switched the potential of the same Pt tip to E = - 0.5 vs. Ag/AgCl, 3 M KCl, to ensure the reduction of the oxygen present in solution at the Pt UME, and we have scanned the same area and obtained a respiration profile of the same single PC12 cell as it can be seen in Figure 5.8b. It is very interesting to observe that the oxygen profile we recorded across the cell does not mirror the topography. Takii et al.[37] reported that the acquired respiration image identically matched the expected topography (profile of the oxygen diffusion hindrance atop the cell, i.e., the oxygen distribution around the cell) and they were not able to show distinctive oxygen uptake profiles.

While we have acquired images (taken at d ≈ 10 μm from the dish surface, not shown) that resemble the previously published cell respiration images as cell topography, when the tip is scanned closer than 10 μm to the surface, it is possible to obtain images that allow differentiation in respiratory activity as a function of spatial location. Since the diffusion of the oxygen is extremely rapid in aqueous solutions, it is important to approach closer to the cell, so that the image obtained (E = - 0.5 vs. Ag/AgCl, 3 M KCl) is not solely the result of the cell topography, but includes oxygen uptake concentration profiles. We have recorded a respiration profile at d $\lesssim$ 8 μm from the dish surface, and the respiration image (3D contour plot, Figure 5.8b) raster

shows the lowest respiration activity in the middle of the cell surface, and the highest respiration activity at the edge of the cell, where the cell makes contact with the Petri dish. While this image does certainly have a component that comes from the distribution of the oxygen around the cell, it is obvious that we were able to record the oxygen depletion by the cell. Figures 5.8c and 5.8d are the corresponding plots for topography (Fig. 5.8a) and respiration (Fig. 5.8b) respectively, and we have inserted crosshairs to better illustrate portions of the 2D profiles. Figure 5.8c, which uses an external redox mediator and so is independent of physiological activity, shows a clear dependence between the current profile and topography for a roughly spheroid cell. Figure 5.8d, however, displays a more convoluted oxygen profile that cannot be explained solely by topography, and therefore is indicative of physiological activity (i.e., respiration) and/or transport properties of the cell or membrane itself.

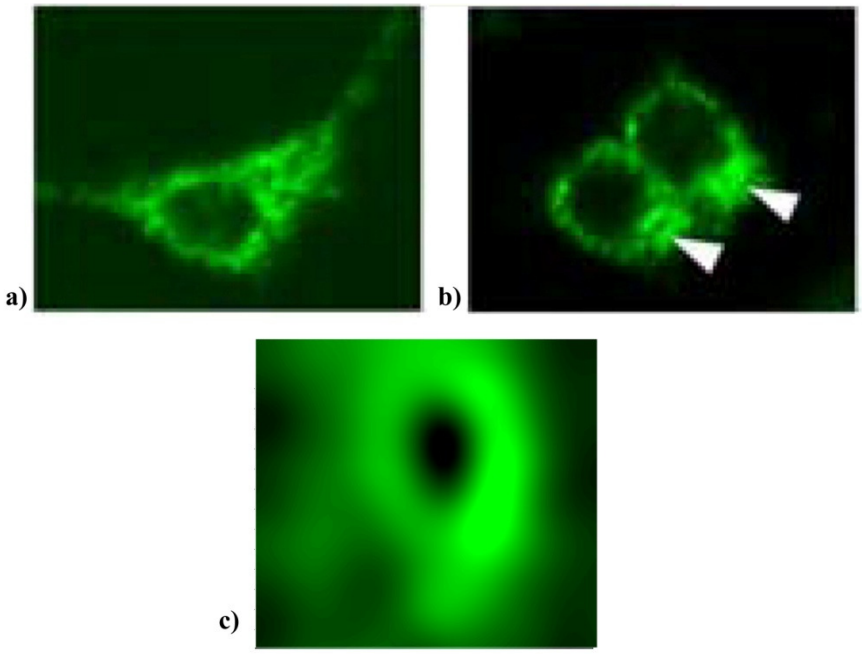

Figure 5.9; Images of stained mitochondria in (a) differentiated and (b) undifferentiated PC12 cells showing their location surrounding the nucleus, which appears as a darkened spot (arrows in (b) point to a clustering of mitochondria with the endoplasmic reticulum), while (c) is the respiratory profile of a single PC12 cell presented previously in Fig. 5.8b/d, with the false color spectrum adjusted to show high oxygen (absence of respiration) as black and low oxygen (respiratory activity) as bright green. The locations ascribed to respiratory activity thus coincide with the locations where mitochondria are present in (a) and (b). [Mitochondrial images from Darios[53]].

One could argue that the reason we are not observing uniform oxygen diffusion across the cell membrane is due to the higher distribution of mitochondria (where cellular respiratory activity occurs) at the points where the cell makes contact with the Petri dish substrate. Previous work using fluorescence microscopy[53] has shown that in cultured PC12 cells the mitochondria are predominantly located in these locations, rather than atop the cell nucleus, as shown in Figs. 5.9 (a) and (b). In order to illustrate the point effectively, the respiratory profile for the single PC12 cell presented previously in Figs. 5.8b/d is shown again in Fig. 5.9c. This time, however, the false color profile has been adjusted in order to mimic the mitochondrial stain used in Figs. 5.9a/b. Now the areas of the image corresponding to background oxygen levels (*i.e.*, no respiration) are shown in black, while areas where reduced oxygen (*i.e.,* respiratory activity) was detected are shown in bright green. Comparison of Figs. 5.9a/b and c show that the areas within the cell where respiratory activity was detected (Fig. 5.9c) coincide with those where mitochondria are present (in Figs. 5.9a/b). There is a slight 'bleeding' of green outside the area of the cell due to the depletion of oxygen in the surrounding media, which is also driven by cellular respiration.

Conclusions

We have manufactured enzyme UMEs for SECM use in the detection of lactate and glucose. We have calibrated these sensors with respect to their analyte and we have shown for the first time that enzyme-based UMEs can be used for positioning the SECM tip via amperometric ACs with respect to the substrate to be scanned. By employing the GOx- and LOx-based UME biosensors, we have obtained glucose uptake and lactate release profiles for single cancer cells as a proof of concept for the application of SECM toward the study of basic metabolic processes that are affected by disease in cancerous cells. We have also shown that respiration studies performed at closer tip-substrate separations (< 10 μm) reveal a non-uniform

distribution of oxygen that cannot be explained by the cell topography alone; these oxygen uptake profiles could give a more complete metabolic picture of the single cancer cells. Comparison of this data with that from previously published mitochondrial staining of PC12 cells shows that the areas where respiratory activity was detected within the cell coincide with those populated by mitochondria. Further experimentation, however, should be performed to definitively assign this convoluted oxygen uptake distribution to mitochondrial location alone. The ability to look at single cell lactate production, glucose and oxygen consumption, in addition to previously published acidification rates profiles, will provide for a direct comparison of single cell data to our multi-cell data from MAMP experiments.

Acknowledgements

We thank Evgheni Kozlov/Ales Prokop (fibroblasts and PC12), Julie Maier/Alissa Weaver (MCF10CA1a) and Kristopher Kahlig/Aurelio Galli (PC12) for cell culture and plating. We acknowledge the following funding sources: NIAID U01 AI061223; NCI U54 CA113007; DARPA/ONR contract N66001-01-8064; the Vanderbilt Integrative Cancer Biology Center; and the Vanderbilt Institute for Integrative Biosystems Research and Education.

References

(1) Suzuki, H. *Electroanalysis* **2000**, *12(9)*, 703-715.
(2) Lindner, E.; Buck, R. P. *Anal. Chem.* **2000**, *72(9)*, 336A-345A.
(3) Yao, T.; Yano, T.; Nanjyo, Y.; Nishino, H. *Anal. Sci.* **2003**, *19(1)*, 61-65.
(4) Marzouk, S. A. M.; Buck, R. P.; Dunlap, L. A.; Johnson, T. A.; Cascio, W. E. *Anal. Biochem.* **2002**, *308(1)*, 52-60.
(5) Garrett, R. H.; Grisham, C. M. *Biochemistry*, Second ed.; Saunders College Publishing: Fort Worth, 1999.
(6) Chen, T.; Schmidtke, D. W.; Heller, A. *Clin. Chem. Lab. Med.* **2002**, *40(8)*, 786-789.
(7) Strike, D. J.; de Rooij, N. F.; Koudelka-Hep, M. *Biosens. Bioelectron.* **1995**, *10(1/2)*, 61-66.
(8) Kueng, A.; Kranz, C.; Mizaikoff, B. *Biosens. Bioelectron.* **2005**, *21(2)*, 346-353.
(9) Ito, N.; Matsumoto, T.; Fujiwara, H.; Matsumoto, Y.; Kayashima, S.; Arai, T.; Kikuchi, M.; Karube, I. *Anal. Chim. Acta* **1995**, *312(3)*, 323-328.
(10) Horrocks, B. R.; Schmidtke, D.; Heller, A.; Bard, A. J. *Anal. Chem.* **1993**, *65(24)*, 3605-3614.

(11) Devadoss, A.; Burgess, J. D. *J. Am. Chem . Soc.* **2004**, *126(33)*, 10214-10215.
(12) Jiang, D.; Devadoss, A.; Palencsar, M. S.; Fang, D.; White, N. M.; Kelley, T. J.; Smith, J. D.; Burgess, J. D. *J. Am. Chem . Soc.* **2007**, *129(37)*, 11352-11353.
(13) Eklund, S. E.; Cliffel, D. E.; Kozlov, E.; Prokop, A.; Wikswo, J.; Baudenbacher, F. *Anal. Chim. Acta* **2003**, *496(1-2)*, 93-101.
(14) Eklund, S. E.; Kozlov, E.; Taylor, D. E.; Baudenbacher, F.; Cliffel, D. E. In *Methods in Molecular Biology*; Rosenthal, S. J., Wright, D. W., Eds.; Humana Press, Inc.: Totowa, 2005; Vol. 303(NanoBiotechnology Protocols), pp 209-223.
(15) Eklund, S. E.; Snider, R. M.; Wikswo, J.; Baudenbacher, F.; Prokop, A.; Cliffel, D. E. *J. Electroanal. Chem.* **2006**, *587(2)*, 333-339.
(16) Eklund, S. E.; Taylor, D.; Kozlov, E.; Prokop, A.; Cliffel, D. E. *Anal. Chem.* **2004**, *76(3)*, 519-527.
(17) Anderson, A. R. A. *Math. Med. Biol.* **2005**, *22(2)*, 163-186.
(18) Anderson, A. R. A.; Weaver, A. M.; Cummings, P. T.; Quaranta, V. *Cell* **2006**, *127(5)*, 905-915.
(19) Kueng, A.; Kranz, C.; Lugstein, A.; Bertagnolli, E.; Mizaikoff, B. *Angew. Chem., Int. Ed. Engl.* **2005**, *44(22)*, 3419-3422.
(20) Bard, A. J.; Fan, F. R. F.; Kwak, J.; Lev, O. *Anal. Chem.* **1989**, *61(2)*, 132-138.
(21) Bard, A. J.; Fan, F. R. F.; Mirkin, M. V. In *Electroanalytical Chemistry*; Marcel Dekker, Inc.: New York, 1994; Vol. 18, pp 243-373.
(22) Bard, A. J.; Fan, F. R. F.; Pierce, D. T.; Unwin, P. R.; Wipf, D. O.; Zhou, F. *Science* **1991**, *254(5028)*, 68-74.
(23) Bard, A. J.; Mirkin, M. V. *Scanning Electrochemical Microscopy*; Marcel Dekker, Inc.: New York, 2001.
(24) Shiku, H.; Ohya, H.; Matsue, T. In *Encyclopedia of Electrochemistry, Vol 9 - Bioelectrochemistry*; WILEY-VCH: Weinheim, Germany, 2002, pp 257-275.
(25) Bard, A. J.; Li, X.; Zhan, W. *Biosens. Bioelectron.* **2006**, *22(4)*, 461-472.
(26) Cai, C.; Liu, B.; Mirkin, M. V.; Frank, H. A.; Rusling, J. F. *Anal. Chem.* **2002**, *74*, 114-119.
(27) Feng, W.; Rotenberg, S. A.; Mirkin, M. V. *Anal. Chem.* **2003**, *75*, 4148-4154.
(28) Hengstenberg, A.; Blochl, A.; Dietzel, I. D.; Schuhmann, W. *Angew. Chem., Int. Ed. Engl.* **2001**, *40(5)*, 905-908.
(29) Isik, S.; Schuhmann, W. *Angew. Chem., Int. Ed. Engl.* **2006**, *45(44)*, 7451-7454.
(30) Kurulugama, R. T.; Wipf, D. O.; Takacs, S. A.; Pongmayteegul, S.; Garris, P. A.; Baur, J. E. *Anal. Chem.* **2005**, *77(4)*, 1111-1117.
(31) Liebetrau, J. M.; Miller, H. M.; Baur, J. E.; Takacs, S. A.; Anupunpisit, V.; Garris, P. A.; Wipf, D. O. *Anal. Chem.* **2003**, *75*, 563-571.
(32) Liu, B.; Cheng, W.; Rotenberg, S. A.; Mirkin, M. V. *J. Electroanal. Chem.* **2001**, *500*, 590-597.
(33) Liu, B.; Rotenberg, S. A.; Mirkin, M. V. *Proc. Natl. Acad. Sci. U.S.A.* **2000**, *97(18)*, 9855-9860.
(34) Liu, B.; Rotenberg, S. A.; Mirkin, M. V. *Anal. Chem.* **2002**, *74*, 6340-6348.
(35) Mauzeroll, J.; Bard, A. J.; Owhadian, O.; Monks, T. J. *Proc. Natl. Acad. Sci. U.S.A.* **2004**, *101(51)*, 17582-17587.
(36) Nishizawa, M.; Takoh, K.; Matsue, T. *Langmuir* **2002**, *18(9)*, 3645-3649.
(37) Takii, Y.; Takoh, K.; Nishizawa, M.; Matsue, T. *Electrochim. Acta* **2003**, *48*, 3381-3385.
(38) Yasukawa, T.; Kaya, T.; Matsue, T. *Electroanalysis* **2000**, *12(9)*, 653-659.
(39) Wipf, D. O.; Bard, A. J. *Anal. Chem.* **1992**, *64(13)*, 1362-1367.
(40) Ludwig, M.; Kranz, C.; Schuhmann, W.; Gaub, H. E. *Rev. Sci. Instrum.* **1995**, *66(4)*, 2857-2860.

(41) Hengstenberg, A.; Kranz, C.; Schuhmann, W. *Chemistry--A European Journal* **2000**, *6(9)*, 1547-1554.
(42) Macpherson, J. V.; Unwin, P. R. *Anal. Chem.* **2001**, *73(3)*, 550-557.
(43) Semenza, G. L.; Artemov, D.; Bedi, A.; Bhujwalla, Z.; Chiles, K.; Feldser, D.; Laughner, E.; Ravi, R.; Simons, J.; Taghavi, P.; Zhong, H. In *The Tumour Microenvironment: Causes and Consequences of Hypoxia and Acidity, Novartis Foundation Symposium, Volume 240*, 2001, pp 251-260; discussion 260-264.
(44) Warburg, O. *The metabolism of tumors*; Constable: London, 1930.
(45) Griffiths, J. R.; McIntyre, D. J. O.; Howe, F. A.; Stubbs, M. In *The Tumour Microenvironment: Causes and Consequences of Hypoxia and Acidity, Novartis Foundation Symposium, Volume 240*, 2001, pp 46-62; discussion 62-67.
(46) Bhujwalla, Z. M.; Artemov, D.; Aboagye, E.; Ackerstaff, E.; Gillies, R. J.; Natarajan, K.; Solaiyappan, M. In *The Tumour Microenvironment: Causes and Consequences of Hypoxia and Acidity, Novartis Foundation Symposium, Volume 240*, 2001, pp 23-38; discussion 38-45.
(47) Walenta, S.; Salameh, A.; Lyng, H.; Evensen, J. F.; Mitze, M.; Rofstad, E. K.; Mueller-Klieser, W. *Am. J. Pathology* **1997**, *150(2)*, 409-415.
(48) Forouzan, F.; Bard, A. J.; Mirkin, M. V. *Isr. J. Chem.* **1997**, *37*, 155-163.
(49) Zhang, Z.; Liu, H.; Deng, J. *Anal. Chem.* **1996**, *68(9)*, 1632-1638.
(50) Santner, S. J.; Dawson, P. J.; Tait, L.; Soule, H. D.; Eliason, J.; Mohamed, A. N.; Wolman, S. R.; Heppner, G. H.; Miller, F. R. *Breast Cancer Res. Treatment* **2001**, *65(2)*, 101-110.
(51) Wilburn, J. P.; Wright, D. W.; Cliffel, D. E. *Analyst* **2006**, *131(2)*, 311-316.
(52) Bard, A. J.; Faulkner, L. R. *Electrochemical Methods: Fundamentals and Applications*, 2nd ed.; John Wiley & Sons, Inc.: New York, 2001.
(53) Darios, F.; Muriel, M.-P.; Khondiker, M. E.; Brice, A.; Ruberg, M. *J. Neurosci.* **2005**, *25*, 4159-4168.

CHAPTER VI

SECM IMAGING OF ANALOG ION CHANNELS*

Introduction

The non-invasive investigation of biological systems, especially at the single-cell level, continues to present a challenge to analytical chemistry. The ability of electrochemical methods of analysis to meet this need has advanced in tandem with the state of the art in electrode construction. The early adaptation of carbon electrodes[1,2] provided the initial investigators with a rudimentary tool to conduct measurements on biological systems, but it was not until the implementation of the modern carbon fiber ultramicroelectrode[3] (Cf-UME) that such measurements could be performed without considerable disturbance to the subject. The subsequent development of scanning electrochemical microscopy[4,5] (SECM) allowed for spatial as well as temporal differentiation of data, providing a new and powerful platform for the use of UMEs in the exploration of biological systems.

The ability of SECM to perform evaluations of biological systems was demonstrated shortly after its inception.[6] Its ability to obtain spatio-temporal maps of both chemical activity and electrical conductivity in an non-invasive manner prevents the addition of uncertainty accompanied by the breeching of the cell membrane (as in patch-clamping) or the addition of extraneous functional groups (such as fluorescent tags) that can potentially alter physiological activity. Through the use of a naturally occurring redox couple (*e.g.*, catecholamine release by vesicles),[7] SECM has the potential to generate completely non-invasive maps of biological

---

*This chapter was previously published as: "*Imaging of voltage-gated alamethicin pores in a reconstituted bilayer lipid membrane via scanning electrochemical microscopy,"* Wilburn, J.P.; Wright, D.W.; Cliffel, D.E., Analyst (Cambridge, United Kingdom), 2006. **131**(2): p. 311-316.

activity in live cultured cells. Other prior biological applications of SECM include the determination of the ionic flux through synthetic pores (such as mica) or macro-scale biological membranes (such as dentine or skin),[8-10] the biological activity of single cells,[11-13] including the redox and acid-base reactivity of human cells[14] and bacteria,[15] the differences of reactivity between non-metastatic and metastatic human breast cells,[16] and mapping of the morphology of neuronal analog cell lines.[17,18] The ability of SECM to create spatial analyte concentration profiles has led to its adaptation in the measurement of metabolic rates, such as respiration in bovine embryos,[11] peroxidase activity of algal protoplasts,[19] and to study the permeability of the nuclear envelope of *Xenopus laevis* oocytes.[20] SECM has also been utilized in the study of charge transfer through bilayer lipid membranes (BLMs),[21] catecholamine emission during exocytosis,[22] and NO emissions by human umbilical cells,[23] but only to position a probe for stationary amperometric measurements; therefore no spatially resolved data was obtained.

Due to the complexity of biological systems, initial analyses often take place on more simple analog systems in order to avoid the myriad of interferents present in a living organism. When dealing with cellular signaling systems, more specifically with ion channels, α-helical peptides that form homo-oligomeric pores through BLMs are often employed as analog systems. Alamethicin, a member of the peptaibol family of antibiotics first isolated from *Trichoderma Viride*, has seen wide use as such a model. Mueller and Rudin[24] first reported that alamethicin could trigger ion transport in reconstituted lipid membranes, effectively mimicking the neurological action potential. Alamethicin has since become one of the most studied ion channel mimics[25] due to its ability to form homo-oligomeric channels, voltage-dependent conductance,[26] and its structural similarity to native transmembrane proteins.

We have incorporated alamethicin into phosphatidylcholine BLMs in order to explore the capability of SECM to map ion channel flux in real-time. The BLM is suspended horizontally in a two compartment electrochemical cell. The probe tip, set to the redox potential of the analyte, is rastered across the surface and current measurements are recorded as a function of

position in the x and y directions, yielding a concentration profile map of the species traveling through the alamethicin pore. Unlike previous applications of SECM to BLM studies, where the instrument was only used to position an electrode for stationary measurements, in this work we expand the focus to utilize the spatial capabilities of SECM as well. Spatio-temporal imaging was applied toward the analysis of both passive transport (leakage) and active transport (through open pores) across BLMs. These images successfully demonstrate the ability of SECM to monitor voltage controlled transport through alamethicin pores embedded in reconstituted BLMs.

Experimental

Materials

All materials listed in this section were used as supplied unless otherwise specified. KCl (ACS grade), MeOH (bioreagent grade), and chloroform (ACS grade) were purchased from Fisher Scientific. NaOH was ordered from EM Science, ethanol (absolute proof) from Aaper, ruthenium (III) hexammine ($Ru(NH_3)_6Cl_3$, hereafter called Ru-hex) and 4-(2-hydroxyethyl)-1-piperazine ethane-sulfonic acid (HEPES) were obtained from Acros Organics, n-decane (99%) was obtained from Alfa Aesar. Alamethicin (from *Trichoderma Viride*) was obtained from Sigma-Aldrich as a solid, subsequently dissolved in EtOH and stored at 4 °C until further use. Ferrocenylmethyltrimethylammonium hexafluorophosphate ($FcTMA^+ \cdot PF_6^-$, or FcTMA) was prepared according to the literature method.[27] All electrolyte solutions used during imaging and formation of the BLM were filtered through a syringe-type filter (0.2 μm, Fisher Science) immediately prior to use.

L-α-phosphatidylcholine (p-choline, from chicken eggs) was received from Avanti Lipids dispersed in chloroform. As per Avanti's recommendations,[28] the chloroform was evaporated by blowing a slow stream of nitrogen over the open vial, while holding it in the hands to keep it warm, until all visible liquid had evaporated and then placed under vacuum for an hour.

Once all chloroform was removed, the lipids were then re-dispersed in n-decane and kept at – 20 °C until used. All aqueous solutions were prepared using ASTM type I water (18 MΩ·cm^{-1}, hereafter referred to as DI water) from a Solution 2000 (Aqua Solutions, Inc.) reverse osmosis system.

Electrode Preparation

The UMEs utilized in this study are of the disc-sealed-in-glass type, and were fabricated from 7 μm carbon-fibers (supplied by Dr. Aurelio Galli, Vanderbilt University Department of Molecular Physiology and Biophysics) with RG values of 1.4 (±0.1). The UMEs were fabricated by the procedure published by Fan and Demaille for disk-in-glass UMEs,[29] using 2 mm borosilicate glass capillaries, conductive silver epoxy from Epoxy Technology, 22-gauge generic copper hook-up wire, and white epoxy sealant (Hysol Epoxi-Patch) from Dexter Corporation. Ag/AgCl reference electrodes were obtained from CH Instruments, and counter electrodes were made of Pt wire (Goodfellow).

The electrode geometry for some UMEs utilized in this study was observed to deviate from that of a circular disc due to variations in the angle between the carbon-fiber and the wall of the capillary. If the fiber was not parallel to the capillary, the resulting exposed disc was oval rather than round, and therefore had a higher surface area. It is for this reason that steady state currents reported in some Fig. captions (Figs 4 & supplemental Fig. S2) exceed that expected for a 7 μm electrode in 1 mM Fc-TMA solution.

Bilayer Membrane Imaging Cell

A horizontal BLM cell (Fig. 6.1a) was designed based on previous work by Amemiya and Bard.[30] The cell consists of two independently accessible chambers separated by a reinforced Teflon foil substrate incorporating the aperture for forming the BLM. The Teflon foil septa

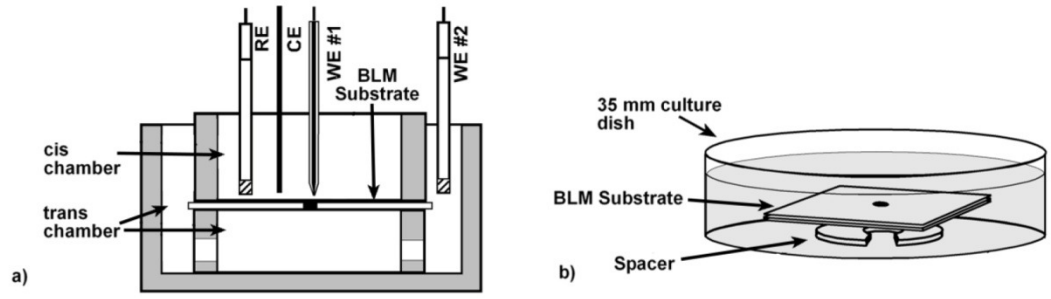

Figure 6.1; (a) a schematic of the cell used for SECM imaging of BLMs in the horizontal configuration, based on work by Amemiya & Bard.[30] (b) a schematic of the simple cell constructed from a 35 mm cell culture dish to form horizontal BLMs.

(model TP-01) were obtained from Eastern Scientific, LLC. Each septum was 25 mm square and 25 μm thick with a preformed, symmetrical aperture of 100 (± 25)μm. These septa were glued with vacuum grease (Dow Corning) to a reinforcing plate for support, cut from the bottom of a plastic cell culture dish, with a hole drilled to allow access to both sides of the aperture (Fig 6.1b). During imaging, the species to be transported initially exists exclusively in the trans compartment, and detection occurs at the probe tip in the cis compartment.

Bilayer Membrane Preparation

Bilayer lipid membranes were made according to a technique previously published by Tripathy *et. al*,[31] which was adapted for use with horizontal BLMs. This method was found to yield BLMs with a higher success rate, longer lifetimes, and less residual solvent content (*i.e.*, a smaller annulus region) than the traditional paintbrush technique. Prior to BLM formation, the Teflon foil septum and plastic plate were rinsed thoroughly in ethanol and DI water. If any stains were visible on either the foil or the Teflon cell, they were soaked overnight in a base bath (EtOH saturated with KOH). The foil septum and plate (hereafter referred jointly to as the BLM substrate) were glued together with high vacuum grease, and then rinsed again briefly with

ethanol and DI water. The inside of the aperture was then 'primed' with a lipid/decane solution (25 - 40 mg/ml) using a trimmed sable or camel hair brush. A slow stream of nitrogen was used to dry the lipid in the aperture.

Horizontal formation of the BLM was accomplished in a simple one-chamber cell (see Fig. 6.1b) constructed from a 35 mm cell culture dish. A one-chamber design, in addition to its simplicity, prevents BLM rupture due to the unequal hydrostatic pressures on either side of the aperture that is possible in a two chamber system. A thin spacer (made from a cut plastic washer), glued to the bottom of the dish with vacuum grease, allowed the solution access to both sides of the aperture, and permitted BLM formation. A small amount of grease was applied to the top of the washer as well to hold the substrate in place during formation. The assembled cell was filled with either a KCl solution (0.1 – 1 M) or a buffer solution (0.1 M KCl and 0.01 M HEPES, pH 7.0). Once the substrate was assembled, rinsed, primed, and dried, it was immediately submerged and affixed to the spacer in the dish. The dish was then placed under a microscope to visually follow the remainder of the procedure. A Drummond micropipette was filled via capillary force with the decane lipid solution, and then the bulk of the solution was expelled from the pipette (some residual lipid and solution remained adsorbed to its inner walls). The pipette tip was then immersed in the solution immediately above the aperture of the substrate, and by squeezing the bulb of the pipette gently an air bubble was blown, forcing the remaining lipids from the pipette to the wall of the air/solution barrier of the bubble. The bubble was then dragged (or 'smeared') across the aperture, leaving behind sufficient lipid to bridge the hole. The lipid then spontaneously thinned to form a bilayer within 1-5 minutes. After waiting ~5 minutes for the bilayer to stabilize, the BLM substrate was transferred to the BLM cell (see Fig. 6.1a) for imaging.

Pore Insertion

Alamethicin pore insertion was performed by addition of ethanolic alamethicin (sufficient to render a final concentration of 100 ng · ml^{-1} in the cis chamber) via micropipette to the solution directly above the BLM. After equilibration (~ 5 minutes), a potential of + 50 mV was applied across the membrane between the second working electrode (Ag/AgCl), which was placed into the trans chamber, and the reference electrode in the cis chamber (see Fig. 6.1a).

SECM Imaging

SECM experiments were conducted on a commercial instrument (CH instruments model 900), controlled with proprietary software. To perform SECM imaging, the BLM cell (see section 2.3) was assembled with the lower chamber filled with Ru-hex solution (1-5 mM in 0.1 M KCl and 0.01 M HEPES, pH 7.0) and the upper chamber with Fc-TMA (1 mM in 0.1 M KCl and 0.01 M HEPES, pH 7.0). All imaging was performed in the constant height mode, at a probe speed of 12.5 μm s^{-1}. Probe approach was performed via negative feedback utilizing the redox mediator in the cis compartment (FcTMA).

Since the BLM cell precluded the use of an inverted microscope during imaging, the aperture and BLM were initially located via topographical imaging prior to imaging of transport across the membrane (see Supplemental Information – Fig. S1). In all cases, Fc-TMA was used as a topographical redox mediator while Ru-hex was used as the transported mediator. Once the aperture and BLM were located, preliminary Ru-hex transport images of the BLMs (prior to addition of alamethicin) were obtained in order to verify the overall integrity of the membrane and allow evaluation of the levels of passive transport. Membranes with pinpoint defects were easily detected via preliminary SECM imaging, due to the presence of 'hot spots' of flux in the region of the defect.

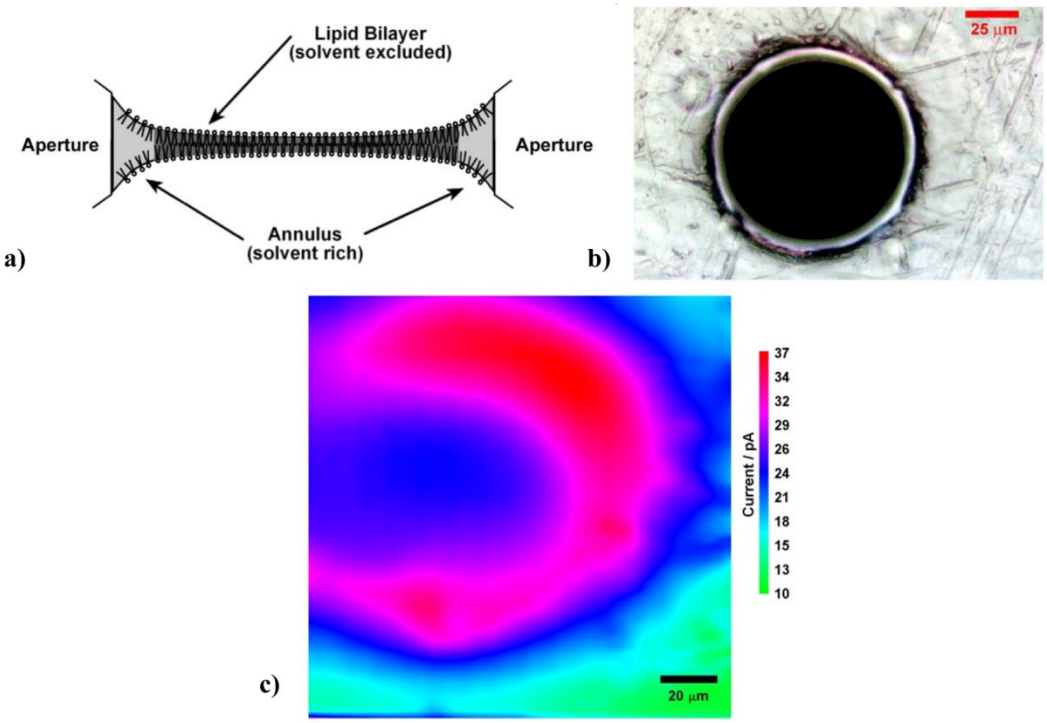

Figure 6.2; (a) topographical schematic cross-section of a BLM/aperture (not to scale) illustrating the difference in thickness between the BLM and the teflon aperture, (b) an optical microscopy image of a BLM formed in a teflon septum with aperture of 100 μm diameter, (c) SECM image showing increased passive transport through a BLM in the annulus region [7 μm CF-UME, 1 mM Ru-hex, 0.1 M KCl, 0.01 M HEPES, pH 7.0, E = -0.35 V, i_{ss}(Fc-TMA,1mM) = 1.2 nA].

Results and Discussion

In order to discuss the results of the experiments, it is first helpful to understand the mechanism of formation and the resulting topography of the BLMs formed in these experiments. The formation of the BLM itself, via a decane film suspended in aqueous solution, is thought to occur via a mechanism similar to the closing of a zipper,[32] as the tails of the two opposing monolayers intercalate to form the bilayer. When followed via optical microscopy, the process can be seen to begin with the appearance of a single dark spot where the two monolayers initially meet. The spot rapidly grows outward toward the edges of the aperture, with the BLM becoming opaque as it stabilizes. The bilayer is prevented, however, from extending completely to the edges of the aperture due to the difference in thickness (Fig. 6.2a) between the BLM (~10 nm) and septum (~25 μm). The Plateau-Gibbs border, present at the edges of the bilayer, is then

visible in transmission optical microscopy images (Fig. 6.2b) as a translucent ring between the aperture egde (seen in the image as a darkened ring) and the completely opaque central bilayer. Due to this ring-like appearance it is often referred to as the annulus. In the annulus region, as opposed to the center, the bilayer is thought to undergo a transition, becoming essentially two monolayers separated by pocket of trapped decane (see Fig. 6.2a). Due to this trapped solvent, the annulus would be expected to pose less resistance than the central region of the BLM to the mass transport of a cation such as Ru-hex.

SECM, due to its ability to map both topography and mass transport across the BLM, was employed to determine if such differences could be detected. SECM images of Ru-hex transport taken in the absence of alamethicin (Fig. 6.2c) show a slight leakage current around the outer edges of the BLM. The difference in current detected between the teflon septum (green) and the BLM (blue) can be explained by noting that the BLM is recessed in the aperture (Fig. 6.2a), rather than at the same level as the teflon surface. Since larger tip-substrate separations when the probe is positioned over the BLM result in higher negative-feedback currents, the current over the BLM is greater than that over the subtrate. The difference in width of the annulus in the SECM image (region of higher current in Fig. 6.2c) as opposed to the optical image (Fig. 6.2b) is thought to be due to lateral diffusion of the Ru-hex prior to reaching the probe tip. The lack of leakage on the left side of the annulus in Fig. 6.2c is an artifact resulting from the direction and speed of the probe scan during the experiment. Since the instrument utilizes the fastest possible rate for the return of the probe to the x-axis origin (the left side of the image) after each line-scan, a localized convection in the solution persists for a short time which disturbs the mass transport between the annulus and the probe tip. When the direction of probe travel was reversed (not shown), the resulting image showed the same absence of leakage on the right side of the BLM instead of the left. Additionally, no difference in transport current is detectable between the annulus region and the remainder of the BLM at higher scan rates, again suggesting that high probe speed leads to convection within the solution.

Since the irregular geometry of the aperture opening caused problems during SECM approach, probe approaches were performed at the higher septum surface, far from the aperture. Due to the taper of the aperture, the BLM surface is much lower (farther from the probe tip) than the septum surface, allowing the Ru-hex to diffuse laterally and creating the anomaly of a wider surface area. The tip-septum distance for this image was extremely small, as can be seen by the level of background current (in the pA range). Images taken at greater probe-septum separation were less likely to show differences between the annulus blockage and that of the BLM itself, also perhaps due to lateral diffusion prior to reaching the probe tip.

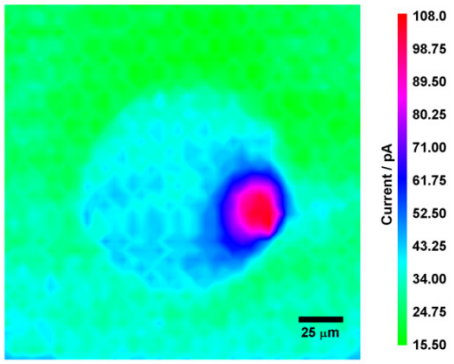

Figure 6.3; SECM image of the Ru-hex leakage (passive transport) through a pinpoint defect in a BLM. [7 µm CF-UME, 1 mM Ru-hex, 0.1 M KCl, 0.01 M HEPES, pH 7.0, E = – 0.35 V, i_{ss}(Fc-TMA, 1 mM) = 1.0 nA].

SECM analyses also proved useful in the preliminary evaluation of the integrity of the BLMs formed during the course of this experiment. While optical microscopy is useful in determining whether a BLM is present, or if formation is not yet complete, it has only limited use in its ability to evaluate the overall integrity of the membrane formed. Some pinpoint defects (Fig. 6.3), for example, were not readily visible during examination of optical images, but were easily detected by preliminary SECM imaging of membrane transport.

Upon addition to the solution surrounding a BLM, alamethicin is thought to form a pore via a voltage-dependent barrel-stave mechanism,[26] where the α-helices initially adsorb parallel to

the lipid membrane. Only upon application of a sufficient membrane potential (50 mV) do the helices incorporate themselves into the membrane and assemble to form an active pore.[26] To ensure that the current measured after alamethicin insertion was the product of mass transport through an active pore, and not electroporation (degradation due to an applied potential), control experiments were performed by applying the bias across a fresh BLM (not shown). There was no change in the BLMs resistivity as a result of the applied bias.

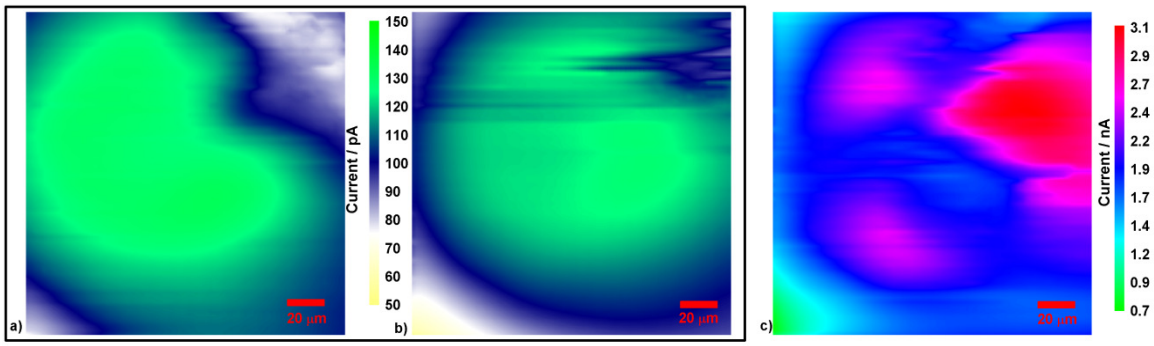

Figure 6.4; SECM images taken sequentially showing the transport of Ru-hex through the same BLM prior to addition of alamethicin (a), after addition of alamethicin but without application of a membrane bias (b), and with a + 50 mV membrane bias (see section 2.5) (c). (a) and (b) share the same color scale (in pA), while (c) has its own color scale (in nA). The current increase from prior to insertion (b) to after insertion (c) is over one order of magnitude (from 150 pA to 3.1 nA). [7 µm CF-UME, 1 mM Ru-hex, 0.1 M KCl, 0.01 M HEPES, pH 7.0, E = – 0.35 V, i_{ss}(Fc-TMA, 1 mM) = 1.9 nA].

Once the integrity of the reconstituted BLM was verified by preliminary imaging, alamethicin pores were incorporated into the membranes. SECM images of mass transport through a BLM in the course of a pore insertion experiment can be seen in Figs. 6.4a-c. The first SECM image (Fig. 6.4a) displays the blocking BLM (in green) and the surrounding teflon septum (in white) prior to the additon of alamethicin to the cell. When the pore forming antibiotic was added via micropipette to the cis compartment, a second image of the same BLM (Fig. 6.4b) was recorded, with no membrane bias. Fig. 6.4b demonstrates the inability of the alamethicin helices to insert themselves into a BLM in the absence of an applied membrane bias. The currents detected prior to the addition of alamethicin (Fig. 6.4a) are similar to those in the SECM image

where alamethicin is present but a membrane bias is not (Fig. 6.4b). Assembly of the reconstituted pore can be seen in the last image (Fig. 6.4c), where three separate 'hot spots' of Ru-hex transport were detected. Due to lateral diffusion, it is not possible to tell whether each of the three individual areas of high current is due to one or several embedded pore bundles. The result of the mass transport through the inserted pores is seen as an increase in detected current of well over one order of magnitude (from 150 pA to 3 nA).

Although the image (Fig. 6.4c) does not show the clear location of a single channel, this is hardly possible given the acquisition time (~ 25 minutes) of the experiment performed. Lipid bilayers are fluid environments, and alamethicin pores are dynamic structures, therefore within the timescale of one imaging experiment a single given pore could change both location and size (e.g. vary the number of constituent monomers) many times. While this image does not pinpoint the location of a single channel, it does provide a probability distribution over where one may be located at any given time.

The use of alamethicin pores as biological ion channel analogs has generally focused on their ability to reproduce voltage-gated channel activity. There has also been a recent move toward the design of microfluidic switches and valves based on biological models. Since the biological ion channel could be viewed as an ideally refined microfluidic bio-switch, it was decided to evaluate the ability of its analog system (the alamethicin pore) to behave in that capacity. Of main concern was whether the difference between the currents measurable in the open and closed conformations would be sufficient to be able to detect a change in states from open to closed (or vice versa).

The results of modulating the membrane potential are shown in Figs. 6.5a-c. The first image (Fig. 6.5a) is the BLM prior to insertion of the alamethicin, and due to the lower current it has a color scale (with current in nA) distinct from the other two images. The result of pore insertion, due to the initial application of a membrane bias (50 mV), can be seen by the increase

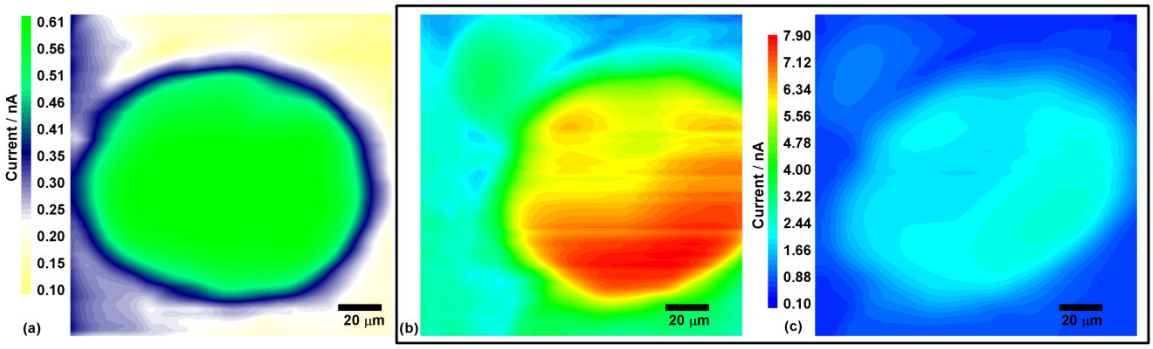

Figure 6.5; Sequential SECM images showing the same BLM prior to insertion of an alamethicin pore (a), after insertion of the pore with a 50 mV membrane bias (see section 2.5) (b), and then after removing the bias (c). Images (b) and (c) share the same color scale (both scales in nA). Once again insertion of the pore (b) results in an increase of transport current by over an order of magnitude. The same color scale was utilized for (b) and (c) to compare the current resulting from the removal of the membrane bias (current decreases by ~ 50% from (b) to (c)). [7 µm CF-UME, 1 mM Ru-hex, 0.1 M KCl, 0.01 M HEPES, pH 7.0, E = – 0.35 V, i_{ss}(Fc-TMA, 1 mM) = 0.98 nA].

in current between the first image (Fig. 6.5a) and second (Fig. 6.5b). The third image (Fig. 6.5c) was then taken after removal of the membrane potential. The shared color scale (current also in nA) between the last two images enables the comparison between the current in the on (Fig. 6.5b) and off (Fig. 6.5c) states of the pore. The current detected for the pore in closed conformation (Fig. 6.5c) shows a drop in current of ~ 50% from the open state (Fig. 6.4b). The image of mass transport in the closed conformation (Fig. 6.5c) retains, however, the spatial distribution found in the open conformation (Fig. 6.5b) suggesting that the alamethicin pores are retained in the membrane even in the absence of a membrane potential. This successfully demonstrated voltage-gated control of the flux across the BLM through the alamethicin pores.

Conclusions

An analog of a biological ion channel system was assembled utilizing a decane dispersion of p-choline to form a planar BLM in a 100 µm diameter aperture, into which was inserted the antibiotic porin alamethicin. SECM, in the constant-height mode was utilized to measure mass transport of Ru-hex under various conditions. Utilization of SECM enabled the evaluation of overall BLM integrity, verification of pore insertion, and control of the mass transport of ions

through the membrane. SECM images showed that the annulus region (Plateau-Gibbs border) of the BLM posed a lower resistance to passive transport of the Ru-hex cation through the membrane. The insertion of alamethicin, and subsequent pore formation, was confirmed by an increase in the measured current levels by more than one order of magnitude over the background (leakage) values due to the mass transport of Ru-hex from the trans compartment. Additionally, the removal of the membrane bias resulted in a detectable change in the current resulting from mass transport, suggesting the possibility that the system could be used as a reversible switch or microfluidic valve.

Acknowledgments

I would like to acknowledge the personal contributions of John P. Wikswo and J. M. Ramsey to this project, as well as the financial assistance provided by the U.S. Department of Energy (LDRD), the U.S. National Institutes of Health (U01 A1 0016223-01), and Vanderbilt University.

References

(1) Kissinger, P. T.; Hart, J. B.; Adams, R. N. *Brain Research* **1973**, *55*, 209-213.
(2) Adams, R. N. *Analytical Chemistry* **1976**, *48*, 1126A-1138A.
(3) Ponchon, J. L.; Cespuglio, R.; Gonon, F.; Jouvet, M.; Pujol, J. F. *Analytical Chemistry* **1979**, *51*, 1483-1486.
(4) Liu, H. Y.; Fan, F. R. F.; Lin, C. W.; Bard, A. J. *Journal of the American Chemical Society* **1986**, *108*, 3838-3839.
(5) Bard, A. J.; Fan, F. R. F.; Kwak, J.; Lev, O. *Analytical Chemistry* **1989**, *61*, 132-138.
(6) Lee, C.; Kwak, J.; Bard, A. J. *Proceedings of the National Academy of Sciences of the United States of America* **1990**, *87*, 1740-1743.
(7) Pitta Bauermann, L.; Schuhmann, W.; Schulte, A. *Physical Chemistry Chemical Physics* **2004**, *6*, 4003-4008.
(8) White, H. S. *Electrochemical Society Interface* **2003**, *12*, 30-34.
(9) Nugues, S.; Denuault, G. *Journal of Electroanalytical Chemistry* **1996**, *408*, 125-140.
(10) MacPherson, J. V.; Unwin, P. R. *Electroanalysis* **2005**, *17*, 197-204.
(11) Shiku, H.; Torisawa, Y.-S.; Takagi, A.; Aoyagi, S.; Abe, H.; Hoshi, H.; Yasukawa, T.; Matsue, T. *Chemical Sensors* **2004**, *20*, 86-87.
(12) Takii, Y.; Takoh, K.; Nishizawa, M.; Matsue, T. *Electrochimica Acta* **2003**, *48*, 3381-3385.

(13) Kaya, T.; Torisawa, Y.-S.; Oyamatsu, D.; Nishizawa, M.; Matsue, T. *Biosensors & Bioelectronics* **2003**, *18*, 1379-1383.
(14) Mirkin, M. V.; Liu, B.; Rotenberg, S. A.; Cheng, W. *Journal of Electroanalytical Chemistry* **2001**, *500*, 590-597.
(15) Mirkin, M. V.; Cai, C.; Liu, B. *Analytical Chemistry* **2002**, *74*, 114-119.
(16) Mirkin, M. V.; Liu, B.; Rotenberg, S. A. *PNAS* **2000**, *97*, 9855-9860.
(17) Kurulugama, R. T.; Wipf, D. O.; Takacs, S. A.; Pongmayteegul, S.; Garris, P. A.; Baur, J. E. *Analytical Chemistry* **2005**, *77*, 1111-1117.
(18) Liebetrau, J. M.; Miller, H. M.; Baur, J. E.; Takacs, S. A.; Anupunpisit, V.; Garris, P. A.; Wipf, D. O. *Analytical Chemistry* **2003**, *75*, 563-571.
(19) Zhou, H.; Kasai, S.; Noda, H.; Ohya-Nishiguchi, H.; Shiku, H.; Matsue, T. *Bulletin of the Chemical Society of Japan* **2003**, *76*, 1757-1762.
(20) Guo, J.; Amemiya, S. *Analytical Chemistry* **2005**, *77*, 2147-2156.
(21) Amemiya, S.; Bard, A. J.; Tsionsky, M.; Zhou, J.; Fan, F.-R. F.; Dryfe, R. A. W. *Anal. Chem.* **1999**, *71*, 4300-4305.
(22) Schuhmann, W.; Hengstenberg, A.; Blochl, A.; Dietzel, I. D. *Angew. Chem. Int. Ed.* **2001**, *40*, 905-908.
(23) Pailleret, A.; Oni, J.; Reiter, S.; Isik, S.; Etienne, M.; Bedioui, F.; Schuhmann, W. *Electrochemistry Communications* **2003**, *5*, 847-852.
(24) Mueller, P.; Rudin, D. O. *Nature (London, United Kingdom)* **1968**, *217*, 713-719.
(25) Bak, M.; Bywater, R. P.; Hohwy, M.; Thomsen, J. K.; Adelhorst, K.; Jakobsen, H. J.; Sorensen, O. W.; Nielsen, N. C. *Biophysical journal* **2001**, *81*, 1684-1698.
(26) Tieleman, D. P.; Berendsen, H. J. C.; Sansom, M. S. P. *Biophysical Journal* **2001**, *80*, 331-346.
(27) Forouzan, F.; Bard, A. J.; Mirkin, M. V. *Israel Journal of Chemistry* **1997**, *37*, 155-163.
(28) Avanti Polar Lipids, 2005; Vol. 2005.
(29) Fan, F.-R. F.; Demaille, C. In *Scanning Electrochemical Microscopy*; Bard, A. J., Mirkin, M. V., Eds.; Marcel Dekker: New York, 2001, pp 75.
(30) Bard, A. J.; Amemiya, S. *Anal. Chem.* **2000**, *72*, 4940-4948.
(31) Tripathy, A.; Tien, H. T.; Ottova, A. L. *Bioelectrochemistry and Bioenergetics* **1998**, *44*, 183-199.
(32) Tien, H. T.; Dawidowicz, E. A. *Journal of Colloid and Interface Science* **1966**, *22*, 438-453.

VITAE

Publications

1. Ciobanu, M.; Taylor, D. E.; Wilburn, J. P.; Cliffel, D. E., *Glucose and lactate biosensors for scanning electrochemical microscopy imaging of single live cells.* Analytical Chemistry, 2008, **80**(8): p. 2717-2727.
2. Wilburn, J.P.; Brown, K.L.; Cliffel, D.E., *Mercury-free analysis of lead in drinking water by anodic stripping square wave voltammetry.* Journal of Chemical Education, 2007, **84**(2): p. 312-314.
3. Ciobanu, M.; Wilburn, J.P.**;** Krim, M.; Cliffel D.E. "Chapter 1: Fundamentals." in "Handbook of Electrochemistry.", edited by C.G. Zoski, Elsevier Science, 2007, pp 934.
4. Wilburn, J.P.; Wright, D.W.; Cliffel, D.E., *Imaging of voltage-gated alamethicin pores in a reconstituted bilayer lipid membrane via scanning electrochemical microscopy.* Analyst (Cambridge, United Kingdom), 2006. **131**(2): p. 311-316.

Manuscripts in preparation

1. Wilburn, J. P.; Ciobanu, M.; Cliffel, D. E. "Scanning Electrochemical Microscopy of Live Islets Using an Insulin-Sensitive Ultramicroelectrode." (to be submitted to Chemical Communications).
2. Ciobanu, M.; Wilburn, J. P.; Snider, R.; Rue, A.; Cliffel, D. E. *Metabolic profiling of pancreatic islets.* (to be submitted to Analytical Chemistry).
3. Wilburn, J. P.; Ciobanu, M.; Jenkins, J. L.; Cliffel, D. E. *Multianalyte Microphysiometry as a Probe of Organophosphate Neurotoxicity.* (to be submitted to Chemical Research in Toxicology).

Works Presented [National/International Conferences]

A. Oral Presentations

1. Cliffel, D. E.; Wilburn, J. P.; Ciobanu, M. *Elucidating Cancer Cell Metabolism using Scanning Electrochemical Microscopy and Microfluidic Physiometry*. PITTCON, Chicago, IL, March 8 – 13, 2009.
2. Cliffel, D. E.; Wilburn, J. P.; Ciobanu, M. *Cellular Energy Metabolism of Single Cells using SECM.* PITTCON, Chicago, IL, February 25 – March 1, 2007.
3. Wilburn, J. P.; Cliffel, D. E.; Wright D. W. *Imaging of Voltage-gated Pores in a Bilayer lipid Membrane via Scanning Electrochemical Microscopy.* PITTCON, Orlando, FL, March 12-17, 2006.
4. Wilburn, J. P.; Cliffel, D. E.; Wright D. W. *Imaging of Voltage-gated Pores Inserted in Bilayer Lipid Membranes.* SW/SERMACS, Memphis, TN, November 1-4, 2005.

B. Poster Presentations

1. Jenkins, J.; Hood, J.; Soni, A.; Cliffel, D. E.; Wilburn, J. P.; Sundaram, S. *Development of Neural Protectants Against Organophosphorus Compound (OPC) Neurotoxicity.* Biomedical Engineering Society Meeting, Chicago, IL, October 11-14, 2006
2. Wilburn, J. P.; Ciobanu, M.; Cliffel, D.E. *Scanning Electrochemical Microscopy of Single Pancreatic Islets.* The 4th Workshop on Scanning Electrochemical Microscopy, Falcade, Italy, September 3-6, 2006.

3. Wilburn, J. P.; Cliffel, David E.; *Non-invasive Imaging of Ion Channels via Scanning Electrochemical Microscopy.* PITTCON, Orlando, FL, Feb. 26 – March 4, 2005.

Works Presented [Local Conferences, Poster Presentations]

1. Snider, R.M.; Ciobanu, M.; Wilburn, J.P.; Rue, A.E.; Chen, Z.; Powers, A.C.; Cliffel, D.E. *Metabolic Profiling of Islets.* Diabetes at Vanderbilt: from Molecules to People, sponsored by The Vanderbilt Diabetes Research and Training Center, Vanderbilt Univ., May 17, 2006.
2. Wilburn, J. P.**;** Cliffel, David E.; *Non-invasive Imaging of Ion Channels via Scanning Electrochemical Microscopy.* 1st Vanderbilt Institute for Cancer Biology Retreat, August 9, 2005.

APPENDIX A

BIOFOULING

One of the major recurring problems occurring in electroanalytical chemistry, and one that becomes more predominant in biological analyses, is that of electrode fouling.[1-3] In unmodified electrodes all chemical reactions occur directly on the surface of the electrode itself, in a rapid sequence of adsorption/reaction/desorption steps. Any substance adhering to the electrode surface, therefore, will result in a reduction of the surface area available to drive such reactions. In real samples, especially biological ones, there are substances within the sample matrix itself that are capable of blocking the electrode. In other cases, the fouling species can be generated by oxidation of a species in the matrix, including the analyte itself.[1]

Biofouling, or electrode fouling due to biological material, is even more predominate with the use of micro and ultramicroelectrodes, due to differences in diffusion and the reduced surface areas involved. With micro electrodes the increased sensitivity toward electrode fouling is solely due to a decrease in surface area, but in ultramicroelectrodes there is an additional diffusional contribution. In macro and micro electrodes, the analytes diffuse toward the electrode surface linearly (fig. A.1a). In ultramicroelectrodes, however, the diffusional pattern is more spherical, due to the extremely smaller electrode area (fig. A.1b). In this case, there is a higher analyte flux per unit of surface area, and any reduction in surface area will have a larger corresponding reduction in current response, and will occur typically in a shorter amount of time.

There are three possible strategies frequently implemented to prevent and/or minimize electrode fouling within the sensor design itself. The first option is to use electrode materials that inherently have lower potential for biofouling, such as carbon nanotubes or more recently doped diamond electrodes.[4-6] This is the best choice when while designing a sensor system you

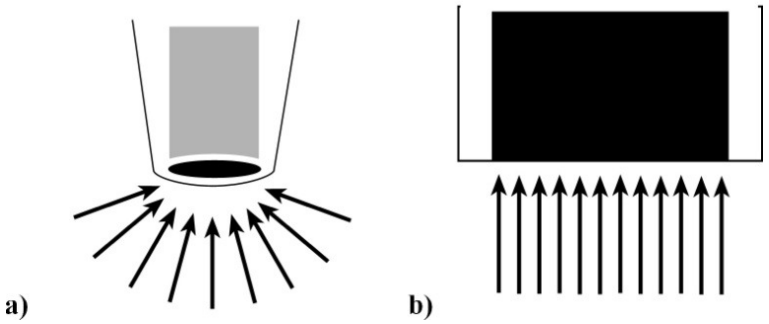

Figure A.1; The diffusional migration of redox species to (a) ultramicroelectrode and (b) micro/macro electrode surfaces.

anticipate there may be a potential for biofouling, however for other pre-existing electrode systems there are other measures that can be taken as well. A second strategy, as utilized by Davies and Brenk[7] and later by Clark[8,9] for unmodified electrode surfaces, is to limit or eliminate the ability of unwanted substances from reaching the electrode surface. This is done through incorporation of permselective membranes[10,11], self-assembled monolayers,[12] or films to the electrode.[2,13-15] The third strategy is to modify the electrode surface itself to reduce adhesion of the poisoning agents. This is done by deposition of metallic films or the inclusion of resistant materials such as carbon nanotubes or chitosan into film coatings. The choice of which strategy to follow depends on individual situations.

In addition to changes in sensor design, there are also changes in experimental design that can be implemented to minimize biofouling. If the fouling is a result of the electrode reaction itself, a switch from constant-potential amperometry to square-wave amperometry or even cyclic voltammetry can reduce the extent of biofouling by minimizing the amount of time current is passed through the electrode. This will, however, decrease temporal resolution of the data collected. This may also be supplemented by the application of a potential pulse between measurements which in some cases has been shown to reverse the effects of unwanted adsorbed substances. Most recently, this potential pulse conditioning has been utilized in condition with thermal conditioning to re-activate the surface of a fouled electrode.[1] This strategy, however,

would not be feasible in the proximity of live cells due to the potential for damage to the cells themselves.

References

(1) Duwensee, H.; Vazquez-Alvarez, T.; Flechsig, G.-U.; Wang, J. *Talanta* **2009**, *77*, 1757-1760.

(2) Wang, J.; Wu, L. H.; Martinez, S.; Sanchez, J. *Anal. Chem.* **1991**, *63*, 398-400.

(3) Kissinger, P. T.; Preddy, C. R.; Shoup, R. E.; Heineman, W. R. In *Laboratory Techniques in Electroanalytical Chemistry,* 2nd Edition ed.; Kissinger, P. T., Heineman, W. R., Eds.; Marcel Dekker: New York, 1996, pp 47-50.

(4) Granger, M. C.; Witek, M.; Xu, J.; Wang, J.; Hupert, M.; Hanks, A.; Koppang, M. D.; Butler, J. E.; Lucazeau, G.; Mermoux, M.; Strojek, J. W.; Swain, G. M. *Anal. Chem.* **2000**, *72*, 3793-3804.

(5) Higson, S.; Vadgama, P. *Anal. Chim. Acta* **1995**, *300*, 77-83.

(6) Shin, D.; Tryk, D. A.; Fujishima, A.; Merkoci, A.; Wang, J. *Electroanalysis* **2005**, *17*, 305-311.

(7) Davies, P. W.; Brink, F., Jr. *Rev. Sci. Inst.* **1942**, *13*, 524-533.

(8) Clark, L. C., Jr.; Helmsworth, J. A.; Kaplan, S.; Sherman, R. T.; Taylor, Z. *Surg. Forum* **1953**, *4*, 93-96.

(9) Clark, L. C., Jr.; Wolf, R.; Granger, D.; Taylor, Z. *J. Appl. Physiol.* **1953**, *6*, 189-193.

(10) Bridge, K.; Davis, F.; Collyer, S.; Higson, S. *Electroanalysis* **2005**, *18*, 95-102.

(11) Higson, S.; Desal, M. A.; Ghosh, S.; Christie, I.; Vadgama, P. *J. Chem. Soc. Faraday Trans.* **1993**, *89*, 2847-2851.

(12) Davis, F.; Higson, S. *Biosens. Bioelectron.* **2004**, *21*, 1-20.

(13) Collyer, S.; Davis, F.; Lucke, A.; Stirling, C. J. M.; Higson, S. *Anal. Chim. Acta* **2003**, *16*, 275-281.

(14) Hoyer, B.; Jensen, N. *Electroanalysis* **2005**, *17*, 2037-2042.

(15) Taylor, M. A.; Jones, M. N.; Vadgama, P.; Higson, S. *Biosens. Bioelec.* **1995**, *10*, 251-260.

APPENDIX B

RESULTS OF STATISTICAL ANALYSIS ON ORGANOPHOSPHATE DATA

Table 1; Statistical analysis of OP experimental results reported in Chapter 3. F-tests and t-tests for all analytes, at each exposure level, show that differences in means and variances (with respect to the RPMI control) are significant at the 95% confidence level.

		RPMI	1 μM	10 μM	100 μM	500 μM	1 mM
Dopamine	mean	11.885	29.352	35.483	47.383	33.002	30.573
	standard deviation	2.077	6.587	9.960	9.640	4.626	2.325
	n	16	16	17	14	13	13
	degrees of freedom		30	31	28	27	27
	t exp		10.607	9.769	13.777	16.456	28.984
	t crit (@ 95%)		1.7	1.7	1.7	1.7	1.7
	F		8.801	53.556	21.189	11.116	8.300
	F crit		4.210	4.225	4.242	4.260	4.242
Calcium	mean	2.614	3.676	4.638	4.063	3.598	3.769
	standard deviation	0.455	1.221	0.901	1.046	0.963	1.376
	n	13	16	15	14	13	14
	degrees of freedom		27	26	25	24	25
	t exp		3.481	8.700	5.185	3.688	3.142
	t crit (@ 95%)		1.7	1.71	1.71	1.71	1.71
	F		33.323	35.578	88.627	51.119	98.696
	F crit		4.121	4.139	4.139	4.160	4.149
Glucose	mean	93.987	54.205	46.100	30.000	37.525	23.721
	standard deviation	21.153	20.575	26.362	18.058	23.682	18.977
	n	20	17	15	15	13	14
	degrees of freedom		35	33	33	31	32
	t exp		7.972	7.035	13.723	8.596	13.854
	t crit (@ 95%)		1.69	1.7	1.7	1.7	1.7
	F		109.083	81.484	206.963	268.524	521.958
	F crit		4.160	4.171	4.196	4.210	4.210
Lactate	mean	0.475	0.996	0.869	0.836	0.404	0.323
	standard deviation	0.105	0.120	0.104	0.142	0.106	0.083
	n	17	10	14	15	14	12
	degrees of freedom		25	29	30	29	27
	t exp		13.753	14.222	9.854	2.495	6.381
	t crit (@ 95%)		1.71	1.7	1.7	1.7	1.7
	F		140.451	109.716	68.224	3.473	17.650
	F crit		4.242	4.183	4.171	4.183	4.210

Table 2; Statistical analysis of OP experimental results reported in Chapter 3. F-tests and t-tests for dopamine, glucose and lactate, at each exposure level, show that differences in means and variances (with respect to the DMSO control) are significant at the 95% confidence level. F-test and t-test results for calcium, however, indicate that only results for 10 and 100 µM are significant at the 95% level (data failing significance testing is highlighted in red).

		DMSO	1 µM	10 µM	100 µM	500 µM	1 mM
Dopamine	mean	15.236	29.352	35.483	47.383	33.002	30.573
	standard deviation	4.643	6.587	9.960	9.640	4.626	2.325
	n	24	16	17	14	13	13
	degrees of freedom		38	39	36	35	35
	t exp		8.572	8.382	12.477	13.845	23.787
	t crit (@ 95%)		1.69	1.69	1.69	1.69	1.69
	F		67.154	69.988	187.104	121.914	109.609
	F crit		4.098	4.105	4.121	4.13	4.149
Calcium	mean	3.357	3.676	4.638	4.063	3.598	3.769
	standard deviation	0.675	1.221	0.901	1.046	0.963	1.376
	n	22	16	15	14	13	14
	degrees of freedom		47	46	45	44	45
	t exp		**1.046**	5.505	2.526	**0.904**	**1.120**
	t crit (@ 95%)		1.68	1.68	1.68	1.68	1.68
	F		**1.064**	24.462	6.096	**0.759**	**1.443**
	F crit		4.113	4.12	4.13	4.139	4.13
Glucose	mean	64.961	54.205	46.100	30.000	37.525	23.721
	standard deviation	23.856	20.575	26.362	18.058	23.682	18.977
	n	24	17	15	15	13	14
	degrees of freedom		39	37	37	35	36
	t exp		12.679	9.294	13.568	9.631	12.473
	t crit (@ 95%)		1.69	1.69	1.69	1.69	1.69
	F		5.324	5.324	23.645	11.209	30.464
	F crit		4.105	4.105	4.105	4.121	4.113
Lactate	mean	0.593833	0.996	0.869	0.836	0.404	0.323
	standard deviation	0.216421	0.120	0.104	0.142	0.106	0.083
	n	24	10	14	15	14	12
	degrees of freedom		32	36	37	36	34
	t exp		10.618	9.932	6.615	6.674	11.346
	t crit (@ 95%)		1.7	1.69	1.69	1.69	1.7
	F		30.257	19.751	14.754	9.337	17.347
	F crit		4.149	4.113	4.105	4.113	4.13